



UNIVERSITÀ DEGLI STUDI DI TRENTO

Department of Physics
Master degree in Physics

**Characterization of the
gravitational wave emission from
binary neutron stars mergers**

Supervisor:

Prof. Giovanni Andrea Prodi

Co-supervisor:

Dr. Claudia Lazzaro

Graduant:

Anna Puecher

Academic year 2017/2018

Abstract

Since their prediction in 1930's, neutron stars were accompanied by the issue of the equation of state describing their matter. Because of its high density, this matter cannot be recreated and studied in laboratory, therefore different ways to investigate it must be looked for. In the last decades, some progresses have been made thanks to nuclear matter studies; on the other hand, astronomical measurements of neutron stars mass and radii allowed to put some constraints on the maximum mass and mass-radius relation for neutron stars, which, in turn, depend on the equation of state. The first detection of a gravitational wave from a binary neutron star in August 2017, GW170817, opened a completely new window on this problem and set the beginning of the multi-messenger astronomy era. Indeed, the features of the gravitational wave signal emitted by a merging neutron star binary strongly depend on the properties of progenitors neutron stars, which therefore can be estimated. Moreover, depending on the progenitor neutron star mass and equation of state, the merger can produce a stable NS, a prompt collapse to a black hole or a massive remnant that later collapses to a black hole. Analyzing the gravitational wave signal emitted during this phase, that strongly depends on the equation of state ruling neutron stars matter, would help to discriminate neutron star models.

For these reasons, the aim of this thesis is to develop new data analysis methods for the characterization of gravitational wave signals emitted by neutron stars binaries during the post-merger phase, with the goal to extract some distinctive parameters, like frequency or duration of post-merger signal. Post-merger signal emitted by neutron stars remnants is difficult to detect because of the lower sensitivity of Earth-based detectors in the high frequencies region it involves, with respect to merger and late-inspiral ones. However, the technological improvements implemented for the O3 run starting next Spring and, later, for O4, will make the detectors gain sensitivity also at higher frequencies, hence an analysis of post-merger signals should become feasible. The analysis is performed in the framework of the coherent Wave Burst pipeline of LIGO-Virgo collaboration, in order to make minimal assumptions about the source and try to estimate its parameters without any a-priori information.

The thesis is organized as follows: in *Chapter 1* I introduce gravitational waves from a theoretical point of view, in the framework of linearized gravity. *Chapter 2* deals with the detection of gravitational waves, from their interaction with test masses to the description of detectors. *Chapter 3* describes the source we are interested in, namely coalescing neutron stars binaries, with a focus on the post-merger phase. In *Chapter 4* I briefly introduce the coherent WaveBurst pipeline and

describe how waveform injections are performed in order to simulate the signals that we are going to study. In *Chapter 5* I present the main results of my work for what concerns time and frequency characterization of post-merger GW signals, describing the estimators we found and how they behave for the different neutron star models considered. Finally, *Chapter 6* introduces the method we are developing to discriminate a prompt-collapse scenario from the formation of a neutron star remnant and to enable some classification of the NS equation of state, starting from the estimators we found.

Notation

We use a spacelike signature $(-, +, +, +)$, with Greek indices running from 0 to 3 and Latin indices from 1 to 3; the standard convention for the summation over repeated indices is adopted.

The values of the principal constants are:

- $c \simeq 3 \times 10^8 m/s$, speed of light in vacuum
- $G \simeq 6.67 \times 10^{-11} \frac{m^3}{kg \cdot s^2}$, gravitational constant
- $M_\odot \simeq 2 \times 10^{30} Kg$, solar mass
- $R_\odot \simeq 7 \times 10^5 Km$, solar radius

Below is reported a list of the acronyms used in this thesis:

NS = neutron star	FDP = False Dismissal Probability
BNS = binary neutron star	TT = Transverse Traceless
BH = black hole	ISCO = Innermost Stable Circular Orbit
GW = gravitational wave	cWB = coherent waveburst
TOV = Tolman, Oppenheimer, Volkoff	DPF = dominant polarization frame
SNR = signal-to-noise ratio	PM = post merger
PSD = power spectral density	WDM = Wilson-Daubachies-Meyer
EOS = equation of state	TF = time-frequency
SMNS = supra-massive neutron star	RMS = root mean square
HMNS = hyper-massive neutron star	LIGO = Laser Interferometer Gravitational-wave Observatory
FAP = False Alarm Probability	

Contents

Introduction	v
1 Gravitational waves	1
1.1 Einstein field equations	1
1.2 The weak field limit	1
1.3 Linearization	3
1.4 Solutions in vacuum	4
1.5 Gravitational waves sources	5
1.6 Gravitational waves energy	9
1.7 Inspiral of compact binaries	11
1.7.1 ISCO	13
2 Gravitational waves detection	14
2.1 GW interaction with test masses	14
2.2 Gravitational waves detectors	16
2.3 Interferometers principle of detection	17
2.4 Basic laser interferometry techniques	18
2.5 Noise sources	20
2.5.1 Seismic noise	21
2.5.2 Gravity gradient noise	21
2.5.3 Thermal noise	22
2.5.4 Quantum noise	22
2.6 Ground-based interferometer response to a gravitational wave	24
2.7 Network of detectors	24
2.8 The detections	25
3 Neutron stars	27
3.1 History	27
3.2 Neutron Stars formation	28
3.3 Neutron stars equation of state	28
3.4 Neutron stars mass and radius	30
3.5 NS structure	31
3.6 Neutron stars population	32
3.7 Neutron star binaries	35

3.7.1	Formation channels of neutron star binaries	35
3.7.2	Binary merger stages	37
3.7.3	Post-merger	37
3.7.4	Gravitational waves from BNS mergers	39
3.8	Detection of GW signal from a BNS	40
3.8.1	GRB and EM counterparts	44
4	Coherent WaveBurst pipeline and simulated signals	47
4.1	cWB algorithm	47
4.1.1	Likelihood method	48
4.1.2	Coherent waveBurst	48
4.2	Waveform models	52
4.3	cWB injections	54
4.4	Theoretical parameters	57
5	Characterization of post-merger signal	61
5.1	Waveform examples	61
5.1.1	SNR checks	62
5.1.2	General time-frequency features of the reconstructed signals	64
5.2	Post-merger identification	66
5.3	Post-merger characterization in time	69
5.3.1	Energy ratio	70
5.3.2	Time duration of post-merger signal	74
5.4	Spectral characterization	81
6	Inferring properties of the post-merger source	89
6.1	Criteria for the detection of a post-merger emission	90
6.2	Luminosity profile	93
6.3	Simulating an observation	93
	Bibliography	103

Chapter 1

Gravitational waves

In this first Chapter we review some basic concepts of General Relativity, in order to see how gravitational waves are included in this theory. We start with a brief explanation of their derivation in the weak field limit, arriving to the solution of linearized Einstein equations both in vacuum and with a source. Finally we describe some properties of gravitational waves, in particular for what concerns the application to compact binaries. The dissertation and resulting equations are taken from [1] and [5], unless different references are specified. From Section 1.2 on, geometrical units $G = c = 1$ are adopted.

1.1 Einstein field equations

The basic idea of General Relativity is that the presence of mass (and therefore energy) produces a curvature in space-time, which cannot be considered simply flat anymore. A tensorial equation is required for gravitational field, in order to hold in every coordinate system. This equation, that relates spacetime local curvature to matter energy tensor is given by Einstein field equations [1]

$$R_{\alpha\beta} - \frac{1}{2}Rg_{\alpha\beta} = \frac{8\pi G}{c^4}T_{\alpha\beta} \quad (1.1)$$

where $R_{\alpha\beta}$ is the Ricci tensor, R the Ricci scalar, $g_{\alpha\beta}$ the spacetime metric and $T_{\alpha\beta}$ the stress-energy tensor, describing the density and flux of energy and momentum in spacetime.

The metric tensor is required to be symmetric and non-degenerate, therefore has only 10 independent components. As a consequence, Eq. 1.1 includes ten non-linear, partial differential equations. However, a quite simple solution can be found in particular circumstances, such as the weak field limit.

1.2 The weak field limit

This limit can be considered as an expansion around flat spacetime, namely we are dealing with tiny deviations in the flat metric:

$$g_{\alpha\beta} = \eta_{\alpha\beta} + h_{\alpha\beta} \quad \text{with} \quad |h_{\alpha\beta}| \ll \eta_{\alpha\beta} \quad (1.2)$$

Since the numerical values of a tensor's components depend on the reference frame, what we mean here is that, in the physical situation in which we are interested, there exists a reference frame where Eq.1.2 holds in a sufficiently large region of space.

Under a generic Lorentz transformation, we have that

$$g_{\alpha'\beta'} = \Lambda_{\alpha'}^{\mu} \Lambda_{\beta'}^{\nu} g_{\mu\nu} \quad (1.3)$$

$$= \Lambda_{\alpha'}^{\mu} \Lambda_{\beta'}^{\nu} (\eta_{\mu\nu} + h_{\mu\nu}) \quad (1.4)$$

$$= \eta_{\alpha'\beta'} + \Lambda_{\alpha'}^{\mu} \Lambda_{\beta'}^{\nu} h_{\mu\nu} \quad (1.5)$$

Since, by definition of Lorentz transformation, $\Lambda_{\rho}^{\mu} \Lambda_{\sigma}^{\nu} \eta_{\mu\nu} = \eta_{\rho\sigma}$, both $\eta_{\alpha\beta}$ and $\eta_{\alpha'\beta'}$ represent the Minkowski metric. Therefore, in a Lorentz-transformed frame, we have

$$g_{\alpha'\beta'} = \eta_{\alpha'\beta'} + h_{\alpha'\beta'} \quad (1.6)$$

provided we define

$$h_{\alpha'\beta'} = \Lambda_{\alpha'}^{\mu} \Lambda_{\beta'}^{\nu} h_{\mu\nu}. \quad (1.7)$$

This choice is consistent with the interpretation of $h_{\alpha\beta}$ as a tensor under Lorentz transformations. Consequently, while in absence of gravity we deal with a flat spacetime described by the Minkowski metric, the presence of a weak gravitational field translates into a "slightly curved" spacetime, that can be approximated as a flat background with a perturbative tensor $h_{\alpha\beta}$ defined on it. Then, all physical fields, like $R_{\mu\nu\alpha\beta}$, can be described in terms of $h_{\alpha\beta}$ and interpreted as fields on a flat background spacetime [1].

General Relativity is invariant under diffeomorphisms, namely coordinate transformations $x^{\mu} \rightarrow x'^{\mu}(x)$, where $x'^{\mu}(x)$ is invertible, differentiable and with a differentiable inverse. Under a generic infinitesimal diffeomorphic coordinate transformation $x^{\mu} \rightarrow x'^{\mu}(x) = x^{\mu} + \xi^{\mu}$, with ξ^{μ} infinitesimal, we have

$$\Lambda_{\beta}^{\alpha'} = \frac{\partial x^{\alpha'}}{\partial x^{\beta}} = \frac{\partial(x^{\alpha} + \xi^{\alpha})}{\partial x^{\beta}} = \delta_{\beta}^{\alpha} + \xi_{,\beta}^{\alpha} \quad (1.8)$$

and similarly

$$\Lambda_{\alpha'}^{\beta} = \delta_{\alpha'}^{\beta} - \xi_{,\alpha'}^{\beta} \quad (1.9)$$

Applying it to Eq.1.4

$$g_{\alpha'\beta'} = \Lambda_{\alpha'}^{\mu} \Lambda_{\beta'}^{\nu} g_{\mu\nu} \quad (1.10)$$

$$= (\delta_{\alpha'}^{\mu} - \xi_{,\alpha'}^{\mu})(\delta_{\beta'}^{\nu} - \xi_{,\beta'}^{\nu})(\eta_{\mu\nu} + h_{\mu\nu}) \quad (1.11)$$

$$= \eta_{\alpha\beta} + h_{\alpha\beta} - \xi_{,\alpha\beta} - \xi_{,\beta\alpha} + \mathcal{O}(\partial\xi^2) \quad (1.12)$$

at lowest order (we assume $\mathcal{O}(h_{\alpha\beta}) \sim \mathcal{O}(|\xi_{\alpha\beta}|)$). Reminding that $\eta_{\alpha\beta}$ and $\eta_{\alpha'\beta'}$ represent the same metric, we conclude that, under a diffeomorphism, the metric perturbation transforms as

$$h_{\mu'\nu'} = h_{\mu\nu} - L_\xi \eta_{\mu\nu}, \quad (1.13)$$

where $L_\xi \eta_{\alpha\beta} = \xi_{\alpha,\beta} + \xi_{\beta,\alpha}$ (Lie derivative on flat metric). In analogy with electromagnetism, where Maxwell equations are invariant under the gauge transformation of vector potential $A^\mu \rightarrow A^\mu + \partial\chi$, with χ an arbitrary scalar field, we can look at 1.13 as a Gauge transformation and say that there exists a gauge freedom to map the (perturbed) metric into another one via a diffeomorphism.

1.3 Linearization

The linearized Einstein equation derives from an expansion of Eq.1.1 to linear order in $h_{\alpha\beta}$, in the weak field condition 1.2.

Starting from the expression for Riemann tensor

$$R_{\alpha\beta\mu\nu} = \frac{1}{2}(g_{\alpha\nu,\beta\mu} - g_{\alpha\mu,\beta\nu} + g_{\beta\mu,\alpha\nu} - g_{\beta\nu,\alpha\mu}) \quad (1.14)$$

and taking into account that $\eta_{\mu\nu}$ elements are constant, hence their derivative is zero, the Riemann tensor to first order in $h_{\mu\nu}$ reads

$$R_{\alpha\beta\mu\nu} = \frac{1}{2}(h_{\alpha\nu,\beta\mu} - h_{\alpha\mu,\beta\nu} + h_{\beta\mu,\alpha\nu} - h_{\beta\nu,\alpha\mu}). \quad (1.15)$$

Contracting it with flat spacetime metric, we can find the Ricci tensor

$$R_{\beta\nu} = R_{\alpha\beta\mu\nu}\eta^{\alpha\mu} = \frac{1}{2}(\partial^\alpha\partial_\beta h_{\alpha\nu} + \partial^\alpha\partial_\nu h_{\beta\alpha} - \partial_\beta\partial_\nu h - \partial^\alpha\partial_\alpha h_{\beta\nu}) \quad (1.16)$$

and Ricci scalar

$$R = \eta^{\beta\nu} R_{\beta\nu} = \partial^\alpha\partial^\nu h_{\alpha\nu} - \partial^\alpha\partial_\alpha h, \quad (1.17)$$

always to first order in $h_{\mu\nu}$.

In order to simplify calculations, we define the *trace-reverse* metric

$$\bar{h}_{\mu\nu} = h_{\mu\nu} - \frac{1}{2}\eta_{\mu\nu}h \quad (1.18)$$

whose name comes from the fact that $\bar{h} = -h$. Exploiting the expansion of Ricci tensor and scalar (Eq. 1.16 and 1.17) and the definition 1.18, we can write the linearized Einstein tensor as:

$$G_{\alpha\beta} = R_{\alpha\beta} - \frac{1}{2}Rg_{\alpha\beta} = -\frac{1}{2}(\partial^\mu\partial_\mu\bar{h}_{\alpha\beta} + \eta_{\alpha\beta}\partial^\mu\partial^\nu\bar{h}_{\mu\nu} - \partial^\mu\partial_\beta\bar{h}_{\alpha\mu} - \partial^\mu\partial_\alpha\bar{h}_{\beta\mu}). \quad (1.19)$$

This expression can be simplified thanks to the gauge freedom that appears from (1.13). Indeed, applying transformation 1.13 to the trace-reverse metric, we obtain

$$\bar{h}_{\mu'\nu'} = \bar{h}_{\mu\nu} - L_\xi \eta_{\mu\nu} + \eta_{\mu\nu}\xi_\alpha^\alpha \quad (1.20)$$

from which the first-derivative terms entering in $G_{\alpha\beta}$ are

$$\partial^{\nu'} \bar{h}_{\mu'\nu'} = \partial^\nu \bar{h}_{\mu\nu} - \square \xi_\mu + \mathcal{O}(\text{sup}) \quad (1.21)$$

where we neglect ξ second derivatives and \square is the flat space D'Alambertian $\square = \eta_{\mu\nu} \partial^\mu \partial^\nu = \partial_\mu \partial^\mu$. Therefore, by imposing $\partial^\nu \bar{h}_{\mu\nu} = \square \xi_\mu$ we can always find an infinitesimal coordinate transformation $x^\mu \rightarrow x^{\mu'} = x^\mu + \xi^\mu$ for which, in the new coordinate system,

$$\partial^{\nu'} \bar{h}_{\mu'\nu'} = 0 \quad (1.22)$$

that considerably simplifies expression 1.19. With this *Lorenz Gauge*, or *Harmonic Gauge*, the linearized Einstein tensor becomes

$$G_{\alpha'\beta'} = -\frac{1}{2} \square \bar{h}_{\alpha'\beta'} \quad (1.23)$$

and the field equations

$$\square \bar{h}_{\alpha\beta} = -16\pi T_{\alpha\beta} \quad (1.24)$$

where the stress tensor is linearized in the same gauge. Notice that the four equations arising from condition 1.22 reduce to six the ten independent components of the symmetric 4×4 matrix $h_{\mu\nu}$.

1.4 Solutions in vacuum

Eq. 1.24 in the Lorenz gauge 1.22 represent the basic equations for gravity linearized theory. In order to study GWs propagation, we are interested in this equation outside the source, namely where $T_{\mu\nu} = 0$. Einstein linearized equation in vacuum reads

$$\square \bar{h}_{\alpha\beta} = 0 \quad (1.25)$$

which has the form of a wave equation, with solutions

$$\bar{h}_{\mu\nu} = C_{\mu\nu} e^{ikx}, \quad (1.26)$$

where $C_{\mu\nu}$ is the matrix of coefficients giving amplitudes for the various components of the wave and $kx \equiv \eta_{\alpha\beta} k^\alpha x^\beta$. In analogy with electromagnetism k^α is called wave vector and, plugging 1.26 into 1.25, it can be proved that it is light-like, which leads to the important consequence that gravitational waves travel with the speed of light. For what concerns coefficients, $C_{\mu\nu}$ is a 4×4 symmetric matrix, whose independent components, thanks to Lorenz gauge, are reduced to six. However, the gauge is not completely fixed yet: if we choose a vector ζ^μ , such that $\square \zeta^\mu = 0$, and perform the coordinate transformation $x^{\mu'} = x^\mu + \xi^\mu + \zeta^\mu$, both the vacuum wave equation 1.25 and the gauge 1.22 are still satisfied, where now $\bar{h}_{\mu'\nu'} = C_{\mu'\nu'} e^{ikx'}$. Hence we can choose the functions ζ^μ as to impose four conditions on $h_{\mu\nu}$: from the six degrees of freedom only two remain, which are the physical ones.

We can choose

$$\zeta^\mu = B_\mu e^{ikx} \quad (1.27)$$

such that $\square \zeta^\mu = 0$ is satisfied.

In order to fix the gauge, we must make a choice on the coefficients $C_{\mu'\nu'}$. We can take

$$C_{\mu'}^{\mu'} = 0, \quad C_{0'\nu'} = 0 \quad \forall \nu' \quad (1.28)$$

in order to have $\bar{h} = 0$ and $h_{0\mu} = 0$ (see [1] for the full derivation). Notice that if $\bar{h} = 0$ we have $\bar{h}_{\mu\nu} = h_{\mu\nu}$, therefore from now on we could drop the bar. It can be proved [5] that this coefficients choice determines unambiguously the B_μ and hence ζ^μ , therefore there are no more gauge degrees of freedom left.

This Traceless-Transverse (TT) gauge

$$h_{0\nu} = 0 \quad \eta^{\mu\nu} h_{\mu\nu} = 0 \quad (1.29)$$

owns its name to the fact that it implies a null-trace and a transverse wave, namely the perturbation is orthogonal to the wave vector. This property, which resembles electromagnetic waves, can be shown via the Lorentz gauge $\partial^j h_{ij}$, that leads to $k^j C_{ij} = 0$.

Therefore, from the original 10 independent components, we are left with only two physical degrees of freedom, the two wave polarizations. Eq.1.25 has solutions like

$$h_{ij}^{TT} = e_{ij}(\mathbf{k}) e^{ikx} \quad (1.30)$$

where e_{ij} is the polarization tensor. Defining the wave propagation direction along the z-axis, 1.30 can be written as

$$h_{\alpha\beta(x)} = \begin{pmatrix} 0 & 0 & 0 & 0 \\ 0 & h_+ & h_\times & 0 \\ 0 & h_\times & -h_+ & 0 \\ 0 & 0 & 0 & 0 \end{pmatrix} e^{ikx} \quad (1.31)$$

1.5 Gravitational waves sources

Now we consider the Einstein linearized equations with a source, namely

$$\square \bar{h}_\alpha \beta = -16\pi T_\alpha \beta, \quad (1.32)$$

where we shall interpret each component of $\bar{h}_\alpha \beta$ as a function on Minkowski space, satisfying a wave equation [3]

$$-\frac{\partial^2 f(x)}{\partial t^2} + \nabla^2 f(x) = j(x) \quad (1.33)$$

with different sources $j(x)$. To solve a generic wave equation 1.33, first we can consider the case when the source is a single δ -function in the origin. A solution of this equation is given by the function

$$g(r, t) \sim \frac{1}{r} [O(t-r) + I(t+r)] \quad (1.34)$$

where $O(t - r)$ and $I(t + r)$ represent, respectively, the outgoing and ingoing parts of the solution. Since we are interested in solutions lying in the future light-cone of the source event, we keep only the outgoing component. The solution $g(r, t)$ of a wave-equation with δ -function source and outgoing wave boundary condition is given by

$$g(t, r) = -\frac{\delta(t - r)}{4\pi r}. \quad (1.35)$$

Since the wave equation is linear, more general sources can be built up by adding waves generated from many δ -sources, namely considering the source as distributed over many space-time points (t', x') . Recalling Eq.1.35, the general solution to a wave equation is

$$f(t, \vec{x}) = -\frac{1}{4\pi} \int d^3x' \frac{j(t_{ret}, \vec{x}')}{|\vec{x} - \vec{x}'|} \quad (1.36)$$

where evaluation at retarded time $t_{ret} \equiv t - |x - x'|$ is necessary in order to account for outgoing wave boundary.

Exploiting these results, the general solution of 1.32 is [3]

$$\bar{h}^{\alpha\beta}(t, \vec{x}) = 4 \int d^3x' \frac{\left[T^{\alpha\beta}(t_{ret}, \vec{x}') \right]}{|\vec{x} - \vec{x}'|} \quad (1.37)$$

To study more in detail the expression for gravitational waves, we make two assumptions:

- we study them far from a weak source, at a distance $r \gg R_s$, where R_s is the characteristic size of the source
- we assume long GW wavelengths, namely $\lambda \gg R_s$, where $\lambda = 2\pi/\omega$ is the wavelength associated with ω , the characteristic frequency of variation of the source. Equivalently, we can ask for low velocities of matter motion inside the source, because, for simple sources, $v_s \sim \omega R_s \ll 1$ [1].

Since y^i represent the spatial coordinates of the source and we are supposing that the field point x^i is far away, $|x^i| \equiv r \gg |y^i| \equiv y$, the asymptotic expression for gravitational waves becomes

$$\bar{h}^{\alpha\beta} = \frac{4}{r} \int d^3y T^{\alpha\beta}(t - r, \vec{y}). \quad (1.38)$$

Over a limited range of angles about any direction \hat{r} , this waveform is approximately a plane wave at large r . For the purpose to analyze physical quantities related to gravitational waves, like energy, flux and so on, we are interested only in spatial components \bar{h}^{ij} , with sources $\int d^3x T^{ij}(t - r, x)$ (moreover, we will see later that spatial components are sufficient to recover $h_{\alpha\beta}$ expression in TT-gauge). We can obtain a more meaningful expression thanks to the flat-metric energy-momentum conservation $T_{,\nu}^{\mu\nu} = 0$, which, for the component $\mu = 0$, yields

$$T_{,0}^{00} + T_{,k}^{k0} = 0. \quad (1.39)$$

Differentiating Eq.1.39 with respect to time and exploiting again $T_{\mu\nu}$ conservation

$$\frac{\partial^2 T^{00}}{\partial t^2} = \frac{\partial^2 T^{kl}}{\partial x^k \partial x^l}. \quad (1.40)$$

Multiplying both sides by $x^i x^j$ and integrating over volume, we obtain

$$\int d^3x T^{ij}(x) = \frac{1}{2} \frac{d^2}{dt^2} \int d^3x x^i x^j T^{00}(x). \quad (1.41)$$

Notice that the right-hand side of 1.40 can be integrated by parts and the boundary terms vanish because integration is performed over a box of volume larger than the source, where therefore $T^{\mu\nu} = 0$.

Eq.1.41 together to (one of) the (possible) definitions of *quadrupole moment tensor*

$$q_{ij}(t) = \int d^3y y^i y^j T^{00}(t, \vec{y}) \quad (1.42)$$

leads to the very important result that gravitational waves are generated, at lowest order, by mass quadrupole moment variations

$$\bar{h}_{ij}(t, \vec{x}) = \frac{2}{r} \dot{q}_{ij} \Big|_{t=t_{ret}}. \quad (1.43)$$

The multipolar expansion can be derived in a more rigorous way by mean of the Fourier transform of energy momentum tensor, considering the expansion of the exponential, where the term of order n brings a correction of order $\mathcal{O}\left(\frac{v}{c}\right)^n$. The leading term of this expansion is indeed proportional to q_{ij} (see [1] for more details).

In general, the stress-energy tensor components are identified as

- T^{00} : energy density
- T^{0i} : energy flux along x^i
- T^{j0} : momentum density
- T^{ij} : stress tensor or momenta flux along x^j

At low velocity approximation, the energy density T^{00} is dominated by rest mass density $\rho(x)$. The resulting momenta are

$$M \simeq \int d^3x \rho(x) \quad (1.44)$$

$$M^i \simeq \int d^3x \rho(x) x^i \quad (1.45)$$

$$M^{ij} \simeq \int d^3x \rho(x) x^i x^j \quad (1.46)$$

$$(1.47)$$

This clearly shows that, taking the time-derivative used in 1.39, $\dot{M} = 0$, because $T^{\mu\nu}$ vanishes at the boundary. Obviously, a system radiating gravitational waves is loosing mass. The conservation of mass expressed by previous equation originates from the linearity approximation made, where the back reaction of the source dynamics due to the energy carried away by GW emission is neglected. For what concerns the first mass moment, we have

$$\dot{M}^i \propto \int_V d^3x x^i \partial_0 T^{00} = - \int_V d^3x x^i \partial_j T^{0j} = \int_V d^3x \delta_j^i T^{0j} \propto P^i \quad (1.48)$$

where P^i is the linear momentum. Eq.1.48 encloses the main difference between gravitational and electromagnetic waves. While the last ones are associated to a change in dipole moment, which corresponds to changing the motion of the center of mass, dealing with gravitational waves the motion of the center of mass of an isolated system is the same as a free-falling particle, therefore cannot change, in order not to violate linear momentum conservation. For this reason, the first term whose time variation can produce a gravitational wave is the second mass moment $M^{ij} \equiv q^{ij}$.

Up to now we considered a generic tensor $\bar{h}_{\alpha\beta}$, but we can express h in TT-gauge. Given a plane wave solution $h_{\mu\nu}(x)$ propagating in direction $\hat{\mathbf{n}}$, we can introduce [1] the symmetric tensor

$$P_{ij}(\hat{\mathbf{n}}) = \delta_{ij} - n_i n_j \quad (1.49)$$

which is transverse ($n^i P_{ij}(\hat{\mathbf{n}}) = 0$) and is a projector ($PikP_{kj} = P_{ij}$). Starting from $P_{ij}(\hat{\mathbf{n}})$, we define the Lambda tensor

$$\Lambda_{ij,kl}(\hat{\mathbf{n}}) = P_{ik}P_{jl} - \frac{1}{2}P_{ij}P_{kl} \quad (1.50)$$

that is a transverse projector too. It can be proved (see [1] for demonstration) that, given a plane wave $h_{\mu\nu}$ in Lorenz gauge, the GW in TT-gauge can be derived from its spatial components by

$$h_{ij}^{TT} = \Lambda_{ij,kl}h_{kl}. \quad (1.51)$$

Recovering the result 1.43 and re-introducing physical units (G and c), we can say that the leading term of multipolar expansion is

$$h_{ij}^{TT}(t, \mathbf{x}) = \frac{2G}{rc^4}\Lambda_{ij,kl}(\hat{\mathbf{n}})\ddot{M}^{kl}(t - r/c). \quad (1.52)$$

The quadrupole tensor M^{ij} can be rewritten as

$$M^{kl} = \left(M^{kl} - \frac{1}{3}\delta^{kl}M_{ii} \right) + \frac{1}{3}\delta^{kl}M_{ii} \quad (1.53)$$

where M_{ii} is the trace. The first term is traceless by construction, while the last term is a scalar. Since the contraction of $\Lambda_{ij,kl}(\hat{\mathbf{n}})$ with δ^{kl} gives zero, the only term that matters when going to the TT-gauge is the traceless one. Defining the *traceless quadrupole moment* as

$$Q^{ij} \equiv M^{ij} - \frac{1}{3}\delta^{ij}M_{kk} = \int d^3x\rho(t, \mathbf{x})(x^i x^j - \frac{1}{3}r^2\delta^{ij}), \quad (1.54)$$

Eq.1.52 can be rewritten as

$$h_{ij}^{TT}(t, \mathbf{x}) = \frac{2G}{rc^4}\Lambda_{ij,kl}(\hat{\mathbf{n}})\ddot{Q}_{kl}(t - r/c) \quad (1.55)$$

$$= \frac{2G}{rc^4}\dot{Q}_{kl}^{TT}(t - r/c). \quad (1.56)$$

1.6 Gravitational waves energy

The concept of energy in General Relativity does not result trivial, since, due to the non-linearity of the theory, the energy enclosed in some region of spacetime depends not only on the mass content, but also on gravitational interaction between different parts of the source. In weak field limit we could think to define an energy-stress tensor associated to the perturbation $h_{\mu\nu}$, but some problems arise. First of all, according to General Relativity, any form of energy contributes to spacetime curvature, therefore, when studying the energy carried by GWs, we should take into account that gravitational waves themselves could produce spacetime curvature. Then, stress-energy tensor is intrinsically a quadratic function of the field, hence a linear expansion in $h_{\mu\nu}$ is not sufficient anymore.

To solve the first issue, we consider now a curved, dynamical background spacetime (no more a flat one), described by a metric $\bar{g}_{\mu\nu}$, such that

$$g_{\mu\nu}(x) = \bar{g}_{\mu\nu}(x) + h_{\mu\nu}(x) \quad |h_{\mu\nu}| \ll 1. \quad (1.57)$$

The major problem arising from this definition is how can we distinguish GW perturbations from metric components, since the metric $g_{\mu\nu}$, in principle, can get contributions changing in space and time [1]. A clear distinction is feasible when background spacetime and GW involve well-separated scales. This happens, for example, when in a coordinate system the background metric changes on a typical space variation L_B , while the small amplitude perturbations superimposed to it have a reduced wavelength

$$\lambda = \frac{\lambda}{2\pi} \ll L_B. \quad (1.58)$$

A similar distinction can be done in frequency space, if background metric varies with frequencies up to f_B and $h_{\mu\nu}$ is peaked around a frequency

$$f \gg f_B. \quad (1.59)$$

While the perturbation frequency and wavelength are related by $\lambda = c/f$, the background quantities are in principle independent, therefore only one of the previous conditions is sufficient to distinguish $\bar{g}_{\mu\nu}(x)$ and $h_{\mu\nu}$. This separation reflects also on GW detectors (which will be discussed in following chapter): for example, ground-based detectors are affected by the noise due to inhomogeneities of Earth gravitational potential, which changes on scales much shorter than the typical $\lambda = 50 - 500 \text{ km}$ of an incoming gravitational wave with frequency $f \sim 1 - 2 \text{ kHz}$. On the other hand, these Newtonian gravitational fields are essentially static, therefore can be distinguished from GWs in frequency space. For that reason, detectors data are usually analyzed in Fourier space, in order to extract eventual GW signals from the background noise. While the condition on frequency is fulfilled for what concerns detectors, usually the theoretical treatment is carried out assuming that the condition on wavelength is satisfied (*short wave expansion*).

Therefore, if one of the previous conditions is fulfilled, the spacetime metric can be approximated as a smooth background plus perturbations. In order to find an expression for the energy, now we must expand Einstein field equations up to second order in $h_{\mu\nu}$. For this purpose it is

useful to write the Einstein equations as

$$R_{\mu\nu} = \frac{8\pi G}{c^4} \left(T_{\mu\nu} - \frac{1}{2} g_{\mu\nu} T \right) \quad (1.60)$$

where T is the trace of matter energy-momentum tensor $T_{\mu\nu}$. The Ricci tensor can be expanded as

$$R_{\mu\nu} = \bar{R}_{\mu\nu} + R_{\mu\nu}^{(1)} + R_{\mu\nu}^{(2)} \quad (1.61)$$

where $R_{\mu\nu}^{(1)}$ contains terms linear in $h_{\mu\nu}$ and $R_{\mu\nu}^{(2)}$ terms quadratic in $h_{\mu\nu}$. $\bar{R}_{\mu\nu}$ is constructed from $\bar{g}_{\mu\nu}$ therefore contains only low frequency terms, $R_{\mu\nu}^{(1)}$ is linear in $h_{\mu\nu}$ hence includes only high frequency terms, while $R_{\mu\nu}^{(2)}$ could have both. Taking into account the separation of scales discussed above, Eq.1.60 can be separated into a low and a high frequency part [1]. This distinction is useful because we can average these quantities over a volume with side \bar{l} , such that $\lambda \ll \bar{l} \ll L_B$. In this way, modes with wavelength $\bar{\lambda} \ll \bar{l}$ are averaged away, while those with $\lambda \sim L_B \gg \bar{l}$ remain almost unaffected. Similarly, if condition 1.59 is satisfied, we can introduce a timescale \bar{t} such that $\frac{1}{f} \ll \bar{t} \ll \frac{1}{f_B}$ and average over \bar{t} or, correspondingly, over many periods of the GW.

Exploiting this averaging procedure, we can define an effective energy-momentum tensor for matter $\bar{T}_{\mu\nu}$ such that

$$\bar{T}_{\mu\nu} - \frac{1}{2} \bar{g}_{\mu\nu} \bar{T} = \left\langle T_{\mu\nu} - \frac{1}{2} g_{\mu\nu} T \right\rangle \quad (1.62)$$

that, by definition, is a purely low-frequency (or low-momentum) quantity, with trace $\bar{T} = \bar{g}_{\mu\nu} \bar{T}^{\mu\nu}$.

Moreover, we can define a tensor

$$t_{\mu\nu} = -\frac{c^4}{8\pi G} \left\langle R_{\mu\nu}^{(2)} - \frac{1}{2} \bar{g}_{\mu\nu} R^{(2)} \right\rangle \quad (1.63)$$

with $R^{(2)} = \bar{g}^{\mu\nu} R_{\mu\nu}^{(2)}$. With definitions 1.62 and 1.63, the low-frequency part of Einstein equation can be rewritten as [1]

$$\bar{R}_{\mu\nu} - \frac{1}{2} \bar{g}_{\mu\nu} \bar{R} = \frac{8\pi G}{c^4} (\bar{T}_{\mu\nu} + t_{\mu\nu}) . \quad (1.64)$$

Performing calculations with the correct gauge choice, in order to consider only real fluctuations due to gravitational field perturbations, leading to physical effects, one can find the expression for GW energy-momentum tensor (details can be found in [1])

$$t_{\mu\nu} = \frac{c^4}{32\pi G} \left\langle \partial_\mu h^{\alpha\beta} \partial_\nu h^{\alpha\beta} \right\rangle . \quad (1.65)$$

In particular, in TT-gauge, the energy density is given by

$$t^{00} = \frac{c^2}{32\pi G} \langle \dot{h}_{ij}^{TT} \dot{h}_{ij}^{TT} \rangle = \frac{c^2}{16\pi G} \langle \dot{h}_+^2 + \dot{h}_\times^2 \rangle . \quad (1.66)$$

Starting from these expressions, one can derive the energy flux

$$\frac{dE}{dt} = \frac{c^3 r^2}{32\pi G} \int d\Omega \langle \dot{h}_{ij}^{TT} \dot{h}_{ij}^{TT} \rangle . \quad (1.67)$$

In the quadrupole approximation worked out in previous section, the radiated power per solid angle becomes [1]

$$\left(\frac{dP}{d\Omega}\right)_{quad} = \frac{c^3 r^2}{32\pi G} \langle \dot{h}_{ij}^{TT} \dot{h}_{ij}^{TT} \rangle = \frac{G}{8\pi c^5} \Lambda_{ij,kl}(\hat{\mathbf{n}}) \langle \ddot{Q}_{ij} \ddot{Q}_{kl} \rangle \quad (1.68)$$

Performing the angular integral, one can find the total radiated power or *Luminosity* \mathcal{L} of the source, yielding the famous **quadrupolar formula**

$$P_{quad} = \frac{G}{5c^5} \langle \ddot{Q}_{ij} \ddot{Q}_{kl} \rangle \quad (1.69)$$

where \ddot{Q}_{ij} is computed at retarded time.

1.7 Inspiral of compact binaries

As said in previous sections, any mass distribution with non-uniformly time-varying quadrupole mass moment can emit gravitational waves. Among all these possible sources, one of the most interesting are star binaries, in particular the systems formed by compact objects, which now we study in detail.

The formalism developed in previous sections provides us with the expressions for some important quantities describing the inspiral phase evolution of a compact binary system. Consider two compact stars of mass m_1 and m_2 , neutron stars or black holes that here we treat as point-like objects, with positions respectively \mathbf{r}_1 and \mathbf{r}_2 . In the Center of Mass (CM) frame, the dynamics of the system can be treated as a one-body problem with reduced mass $\mu = m_1 m_2 / (m_1 + m_2)$ and equation of motion $\ddot{\mathbf{r}} = -(Gm/r^3) \mathbf{r}$, with $m = m_1 + m_2$ total mass and $\mathbf{r} = \mathbf{r}_2 - \mathbf{r}_1$ relative coordinate [1]. The compensation of gravitational and centrifugal force required by Newtonian mechanics leads to the third Kepler law

$$\frac{Gm^2}{(2R)^2} = \frac{mv^2}{R} \quad (1.70)$$

from which

$$\omega_b = \sqrt{\frac{Gm}{4R^3}} \quad (1.71)$$

with v tangent velocity, ω_b angular frequency and R radius of the orbit.

Using the expression for second mass moment in CM frame $M_{CM}^{ij} = \rho x_0^i(t)x_0^j(t)$ and parametrizing the stars position in polar coordinates as

$$x_0(t) = R \cos(\omega_b t + \frac{\pi}{2}) \quad (1.72)$$

$$y_0(t) = R \sin(\omega_b t + \frac{\pi}{2}) \quad (1.73)$$

$$z_0(t) = const \quad (1.74)$$

we can find

$$q_{xx} = \mu R^2 \frac{(1 - \cos(2\omega_b t))}{2} \quad q_{yy} = \mu R^2 \frac{(1 + \cos(2\omega_b t))}{2} \quad (1.75)$$

$$q_{xy} = q_{yx} = -\frac{1}{2} \mu R^2 \sin(2\omega_b t) \quad (1.76)$$

while all other components vanish.

Hence the explicit form of the wave is [1]

$$h_{ij} = \frac{4G\mu\omega_b^2 R^2}{r} \begin{pmatrix} \cos(2\omega_b t_r) & \sin(2\omega_b t_r) & 0 \\ \sin(2\omega_b t_r) & -\cos(2\omega_b t_r) & 0 \\ 0 & 0 & 0 \end{pmatrix}. \quad (1.77)$$

The gravitational wave frequency emitted by a binary system during its inspiral phase is twice the orbital frequency: $\omega_{gw} = 2\omega_b$.

If we want to account for the fact that a wave produced in a reference frame (x, y, z) can be observed in a different frame (x', y', z') , where the z' -axis is inclined of an angle θ with respect to the z one, and the plane $x'y'$ is rotated of angle ϕ with respect to xy , the polarization amplitudes become

$$h_+(t, \theta, \phi) = \frac{1}{r} \frac{4G\rho\omega_b^2 R^2}{c^4} \left(\frac{1 + \cos^2 \theta}{2} \right) \cos(2\omega_b t_{ret} + 2\phi) \quad (1.78)$$

$$h_\times(t, \theta, \phi) = \frac{1}{r} \frac{4G\rho\omega_b^2 R^2}{c^4} \cos \theta \sin(2\omega_b t_{ret} + 2\phi) \quad (1.79)$$

This expression can be rewritten removing R in favor of ω_b and further simplified introducing the *chirp mass*

$$M_c = \mu^{3/5} m^{2/5} = \frac{(m_1 m_2)^{3/5}}{(m_1 + m_2)^{1/5}} \quad (1.80)$$

Defining the gravitational wave frequency $f_{gw} = 2\pi/\omega_{gw}$, with $\omega_{gw} = 2\omega$, Eq.1.78 becomes

$$h_+(t, \theta, \phi) = \frac{4}{r} \left(\frac{GM_c}{c^2} \right)^{5/3} \left(\frac{\pi f_{gw}}{c} \right)^{2/3} \left(\frac{1 + \cos^2 \theta}{2} \right) \cos(2\pi f_{gw} t_{ret} + 2\phi) \quad (1.81)$$

$$h_\times(t, \theta, \phi) = \frac{4}{r} \left(\frac{GM_c}{c^2} \right)^{5/3} \left(\frac{\pi f_{gw}}{c} \right)^{2/3} \cos \theta \sin(2\pi f_{gw} t_{ret} + 2\phi) \quad (1.82)$$

Starting from Eq.1.68, one can find the total radiated power

$$P = \frac{32}{5} \frac{c^5}{G} \left(\frac{GM_c \omega_{gw}}{2c^3} \right)^{10/3} \quad (1.83)$$

Polarizations amplitudes in Eq.1.81 have been derived assuming a fixed, circular Keplerian orbit. However, the emission of gravitational radiation costs energy, taken from the kinetic and potential energy of the orbit

$$E_{orbit} = E_{kin} + E_{pot} = -\frac{Gm_1 m_2}{R}. \quad (1.84)$$

Therefore, to compensate for energy loss, R must decrease in time, implying that ω increases and, consequently, the radiated power becomes greater and greater, further enhancing R reduction. This process, at the end, leads to the binary coalescence. As long as $\dot{\omega} \ll \omega^2$, $|\dot{R}|$ is much smaller than the tangential velocity ωR , therefore we can safely consider the approximation of a circular orbit with varying radius. Equating P in Eq.1.83 to $-\frac{dE_{orbit}}{dt}$, one can find [1] the evolution in time of gravitational wave frequency

$$\dot{\omega}_{gw} = \frac{12}{5} 2^{1/3} \left(\frac{GM_c}{c^3} \right)^{5/3} \omega_{gw}^{11/3} \quad (1.85)$$

or

$$\dot{f}_{gw} = \frac{96}{5} \pi^{8/3} \left(\frac{GM_c}{c^3} \right)^{5/3} f_{gw}^{11/3}. \quad (1.86)$$

Integrating the last equation, we see that f_{gw} formally diverges at a finite value of time, that we call t_{coal} . The gravitational wave frequency can be expressed as a function of $\tau = t_{coal} - t$, time to coalescence, as [1]

$$f_{gw}(\tau) = \frac{1}{\pi} \left(\frac{5}{256} \frac{1}{\tau} \right)^{3/8} \left(\frac{GM_c}{c^3} \right)^{-5/8} \simeq 134 Hz \left(\frac{1.21 M_\odot}{M_c} \right)^{5/8} \left(\frac{1 s}{\tau} \right)^{3/8}. \quad (1.87)$$

The frequency divergence appears only formally, because, from the physical point of view, for a separation smaller than a critical distance the two stars merge.

Therefore, the inspiral phase of a binary system depends on the chirp mass parameter, which is the source property that we can better estimate from a gravitational wave signal.

1.7.1 ISCO

All calculations above have been performed assuming a flat background, but curvature corrections become important when dealing with compact objects such as black holes and neutron stars. The main difference is that General Relativity predicts a minimum distance value beyond which stable circular orbits are no more allowed. This Innermost Stable Circular Orbit (ISCO) distance, in Schwarzschild coordinates, is given by [3]

$$r_{ISCO} = \frac{6Gm}{c^2}. \quad (1.88)$$

This means also that the waveform calculated above is valid up to a maximum orbital frequency

$$f_{ISCO} = \frac{1}{6\sqrt{6}(2\pi)} \frac{c^3}{Gm} \simeq 2.2 kHz \left(\frac{M_\odot}{m} \right) \quad (1.89)$$

While approaching the ISCO, strong field effects become more and more important, until the two objects are so close that start plunging together.

Chapter 2

Gravitational waves detection

So far we have seen what gravitational waves are, how they derive from Einstein field equations and how to describe their main properties. Now we turn our attention to the experimental side, investigating the principal features of gravitational waves detectors and briefly describing the detections made up to now.

2.1 GW interaction with test masses

Physical effects of gravitational waves can be observed in their interaction with test masses, just like spacetime curvature is detectable through the motion of test bodies. With "test masses" we mean bodies that move along the geodesics of the curved spacetime but have masses too small to produce (or modify) a spacetime curvature on their own. Observing just one point-like mass is not enough to detect a gravitational wave: if we study the motion of a test mass in a frame free falling with it, the mass remains at rest, independently of gravitational waves passage. Therefore its motion cannot be distinguished from that of a test mass in flat spacetime, consistent with equivalence principle.

We must look at the mutual acceleration between two test bodies, because a gravitational wave will stretch periodically the spacetime between them. Consider two point-like particles, initially very close, free-falling, respectively, along the geodesics $x^\mu(\lambda)$ and $x^\mu(\lambda) + \xi^\mu(\lambda)$, with ξ^μ separation vector that we assume small and λ affine parameter (for convenience we can choose it to be the proper time, $\lambda \equiv \tau$). If spacetime is not Euclidean, we expect that the distance between these two particles will change during the motion. This relative acceleration is intimately connected to the geometry of spacetime through the Riemann tensor $R_{\mu\nu}^\alpha$ and is described by the *geodesic deviation equation* [2] [5]

$$\frac{d^2\xi^\mu}{d\lambda^2} = R_{\nu\rho\sigma}^\mu U^\nu U^\rho \xi^\sigma \quad (2.1)$$

with U^ν and U^ρ four-velocities.

In the previous chapter we saw that gravitational waves assume a particularly simple form in a reference frame defined by the TT gauge. In order to evaluate the effect of GWs on test masses in this frame, first of all we consider the geodesic equation for a test particle [3][1]

$$\frac{d^2x^\beta}{d\tau^2} + \Gamma_{\alpha\nu}^\beta \frac{dx^\alpha}{d\tau} \frac{dx^\nu}{d\tau} = 0 \quad (2.2)$$

where the Christoffel symbols $\Gamma_{\alpha\nu}^\beta$ depend on the metric tensor, since they can be obtained from [3][5]

$$\Gamma_{\alpha\nu}^\beta = \frac{1}{2} g^{\mu\beta} (g_{\mu\alpha,\nu} + g_{\nu\mu,\alpha} - g_{\alpha\nu,\mu}) \quad (2.3)$$

Eq.2.2 describes the free-fall motion, in a gravitational field, of a massive point-like particle.

In TT gauge, we can consider only spatial components $\beta = i$. Expanding the Christoffel symbols $\Gamma_{\alpha\nu}^\beta$ to first order in $h_{\mu\nu}$ and assuming that the particle is initially at rest (namely $\frac{dx^i}{d\tau} = 0$ at $\tau = 0$), one can show that $\frac{dx^i}{d\tau}$ remains zero at all the times [1], therefore a particle at rest remains at rest also after the passage of a gravitational wave. If the coordinates of a test mass remain constant, also the coordinate distance between two particles should not change. This can be shown by writing the spatial components $\mu = i$ of Eq.2.1 and exploiting the properties of TT-gauge, until one finds the geodesic deviation equation form in TT-gauge [1]

$$\frac{d^2\xi^i}{d\tau^2} \Big|_{\tau=0} = - \left[\dot{h}_{ij} \frac{d\xi^i}{d\tau} \right]_{\tau=0} \quad (2.4)$$

Therefore, if at $\tau = 0$ the particle is at rest ($\frac{d\xi^i}{d\tau} = 0$), also $\frac{d^2\xi^i}{d\tau^2} = 0$ and the separation ξ^i remains constant. This derives from the fact that we exploited the gauge freedom to choose a frame in which coordinates do not change. Instead, physical effects of gravitational waves can be observed investigating proper distance and time. Considering a gravitational wave propagating along the z-axis, the proper distance between two events is [1]

$$s = L[1 + h_+ \cos(\omega t)]^{1/2} \simeq L[1 + \frac{1}{2}h_+ \cos(\omega t)] \quad (2.5)$$

with L coordinate distance. The separation between two masses, in terms of proper distance, will oscillate when a GW (here we considered only the h_+ component for simplicity) stretches the spacetime, resulting in a *strain*.

Although the TT frame simplifies a lot the description of gravitational waves, the experimental apparatus is usually described in the more suitable *proper detector frame*, which takes into account the fact that laboratories usually rotate and accelerate with respect to an inertial frame [9]. The proper detector frame corresponds to the coordinate system created by an observer using a rigid rule to define spatial coordinates with respect to an origin, usually taken as the laboratory center, where is placed also a clock that defines the time coordinate [1] [10].

In such a frame, the geodesic deviation equation becomes [1]

$$\ddot{\xi}^i = \frac{1}{2} \ddot{h}_{ij}^{TT} \xi^j. \quad (2.6)$$

Remember that geodesic deviation equation 2.1 is derived expanding up to first order in ξ^μ and neglecting all higher orders. This approximation remains valid only for small $|\xi^i|$, i.e. when the coordinate separation between the two masses is much smaller than the typical variation scale of gravitational waves

$$L \ll \lambda_{gw} \quad (2.7)$$

However, this requirement is widely fulfilled in ground-based interferometers and bar detectors.

Starting from Eq.2.6 we can understand the physical effect of the passage of a gravitational wave. The separation between particles is periodically stretched and compressed in the directions perpendicular to the GW-propagation one, producing the effect shown in figure 2.1 on a ring of particles. Differently from electromagnetic waves, whose polarizations are rotated by $\pi/2$, the angle between the two gravitational waves polarizations is $\pi/4$. Up to now we have always treated the two polarization components separately, but one should keep in mind that the most general linearized gravitational wave results from a superposition of them.

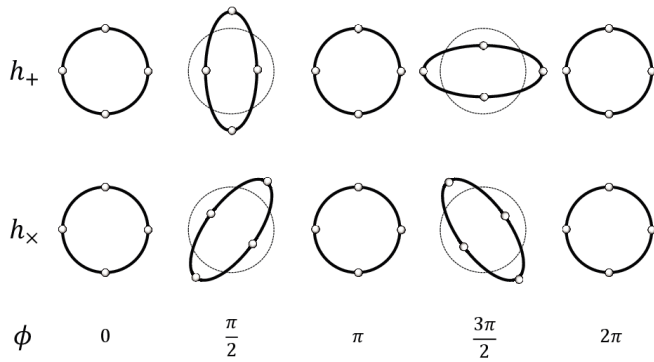


Figure 2.1: Physical effects of the two polarization components h_+ and h_\times of a gravitational wave, traveling along z direction, on a ring of test masses on xy plane.

2.2 Gravitational waves detectors

Many techniques have been developed to detect gravitational waves, but all of them exploit the fact that, if the test masses are separated by a coordinate distance L , and the passage of a gravitational wave causes a displacement ΔL , the *strain* can be approximated [3] as

$$h \simeq \frac{\Delta L}{L} \quad (2.8)$$

which highlights that the displacement ΔL , the quantity we want to measure, is proportional to the dimension of the detector L .

Gravitational waves detectors divide into two main classes:

- Resonant mass detectors
- Laser interferometers (ground and space based)

Actually, there exists also a different technique, that concerns Doppler tracking of pulsars timing or of electromagnetic signals exchanged between a spacecraft and Earth, looking mainly for stochastic background, but we will not deal with it here.

Resonant mass detectors were the first kind of detector built in laboratory to search for gravitational wave signals. However, two main issues affects mass detectors: first of all, the frequency sensitivity is restricted to a narrow band, therefore broad-band searches for GW signal are not possible. In these detectors, gravitational waves transfer energy to the massive body, whose subsequent oscillations are observed. For this reason sensitivity is peaked on a detector mechanical resonance (the first longitudinal mode for bar detectors), where the energy absorption is maximized [11][4]. Moreover, such detectors (that are usually in the form of bars, although some proposal for spherical masses were made, in order to acquire directionality sensitivity) had a limited length, which, recalling Eq.2.8, affects the measurable displacement ΔL . Among the principal sources of noise affecting resonant bars we include vibrations induced by mechanical ambient noise and thermal spontaneous motion of matter. Some expedients were implemented in order to reduce them, such as suspending the bar in vacuum and cooling it down to ultra low temperatures. The most important detectors based on this technique were AURIGA, NAUTILUS, EXPLORER and ALLEGRO. However, the limitations affecting this kind of detectors make them very unlikely to be able to detect a gravitational wave signal, and nowadays none of them is operational.

2.3 Interferometers principle of detection

Interferometers use light beams to measure the length difference between two perpendicular arms. This technique is based on Michelson interferometer [7], which adapts particularly well to GW detection due to their quadrupolar nature. Indeed, if a GW arrives perpendicular to the detector plane, one arm will result increased in length and the other one reduced, hence maximizing the detectable length difference. Figure 2.2 shows a simple scheme for this kind of interferometer: a beam of monochromatic light, a laser, goes through a beam splitter, with equal probability to be reflected or transmitted. Then, the two light beams are completely reflected by the mirror at the end of each arm and bounce back, recombining at the beam splitter. Part of the resulting beam goes into a photodiode, which measures its intensity.

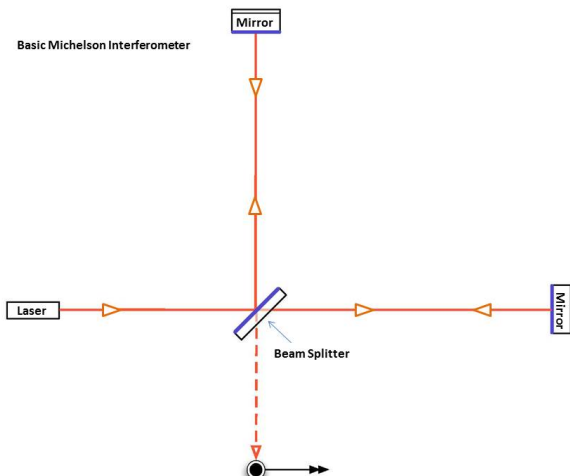


Figure 2.2: Schematic representation of a basic Michelson interferometer, [7]

We denote ω_L the laser frequency, hence its wavenumber and wavelength read $k_L = \frac{\omega_L}{c}$ and $\lambda_L = \frac{2\pi}{k_L}$. Turning to the complex expression for the electric field, its x and y components can be written as

$$E_x = E_0 e^{-i\omega_L t + ik_L x} \quad E_y = E_0 e^{-i\omega_L t + ik_L y} \quad (2.9)$$

Assuming that the interferometer arms are oriented along x and y axis, we call their lengths L_x and L_y . When a photon emitted by the laser arrives at the beam splitter, it has 50% probability to be reflected into the y -arm and 50% to be transmitted into the x one. We assume that there are no phase discontinuities while the field is free-propagating, but it gains an additional π phase from the total reflection on the mirror at the end of the arm, which, ideally, allow no transmission. Adopting the convention that for a 50/50 beam splitter the transmission yields a factor $\frac{1}{\sqrt{2}}$ to the electric field amplitude, while reflection modulates it with factor $\frac{1}{\sqrt{2}}$ on one side of the mirror and $-\frac{1}{\sqrt{2}}$ on the other, the two electric fields that at the end recombine at the beam splitter are [1]

$$E_1 = -\frac{1}{2}E_0 e^{-i\omega_L t + 2ik_L L_x} \quad (2.10)$$

$$E_2 = +\frac{1}{2}E_0 e^{-i\omega_L t + 2ik_L L_y} \quad (2.11)$$

Using the identities $2L_x = L_x + L_y - (l_y - L_x)$ and $2L_y = L_x + L_y - (L_x - L_y)$, we can rewrite the total electric field $E_{out} = E_1 + E_2$ as

$$E_{out} = -iE_0 e^{-i\omega_L t + 2ik_L (L_x + L_y)} \sin[k_L(L_y - L_x)] \quad (2.12)$$

and the power measured by the photodiode will be [1]

$$P_{out} \propto |E_{out}|^2 = E_0^2 \sin^2[k_L(L_y - L_x)]. \quad (2.13)$$

Therefore, any variation in arms length results in a modification of measured output power.

2.4 Basic laser interferometry techniques

Real interferometers detectors are far more complicated than this. Here we briefly describe some laser interferometric techniques generally adopted to enhance the detectors performance. More details can be found in [8], [7], [18] and [17].

Fabry-Perot cavities

Effect 2.13 can be seen as a difference in phase that leads to different interference patterns. In particular, the total electric field when the two beams recombine at the beam splitter can be written as [1]

$$E_{tot}(t) = -iE_0 e^{-i\omega_L(t-2L/c)} \sin[\phi_0 + \Delta\phi_{gw}(t)] \quad (2.14)$$

where ϕ_0 depends on how the detector is built and can be adjusted, while $\Delta\phi_{gw}$ contains the effect of gravitational wave and, in the limit of $\omega_{gw}L/c \ll 1$, reduces to

$$\Delta\phi_{gw}(t) \simeq h(t - L/c)k_L L \quad (2.15)$$

It follows that the total output power detected by the photodiode $P_{out} \sim |E_{out}|^2$ is modulated by the gravitational wave

$$P = P_0 \sin^2[\phi_0 + \Delta\phi_{gw}(t)] = \frac{P_0}{2}[1 - \cos(2\phi_0 + 2\Delta\phi_{gw}(t))]. \quad (2.16)$$

To detect the effects of a gravitational wave, we want to maximize $\Delta\phi_{gw}(t)$. It can be proved [1] that, for a GW of frequency ω_{gw} , $\Delta\phi_{gw}$ depends on L as

$$\Delta\phi_{gw} \propto \sin(\omega_{gw}L/c) \quad (2.17)$$

therefore the optimal length in order to maximize $\Delta\phi_{gw}(t)$ is

$$L = \frac{\lambda_{gw}}{4} \simeq 750 \text{ km} \left(\frac{100 \text{ Hz}}{f_{gw}} \right) \quad (2.18)$$

For this value of L, the phase shift induced by the gravitational wave has the same sign along all its round trip in the arm, therefore the effect sums up and is enhanced.

From the practical point of view, interferometer arms of hundreds of kilometers are impossible to obtain. For this reason, both arms are provided with a resonant Fabri-Perot cavity, that allows an effective optical length

$$L_{eff} = 2L \frac{\mathcal{F}}{2\pi} \quad (2.19)$$

with \mathcal{F} finesse of the cavity, with design value $\mathcal{F} \approx 450$ [17]. From a naive point of view, we can say that the Fabri-Perot cavity is composed by two mirrors that make the photons bounce back and forth many times. In this way the time a photon spends in the arm is increased to $\tau_s = \frac{L}{c} \frac{\mathcal{F}}{\pi}$ and hence the effect of gravitational waves enhanced. The main issue of this technique is that Fabri-Perot cavities act like a low-pass filter, therefore they kill detectors sensitivity at higher frequencies.

Power recycling

It can be shown (see [1] and references therein) that in a Michelson interferometer an optimum signal-to-noise ratio SNR can be obtained adjusting the arms length in a such a way that the output light is very close to a minimum, namely near a dark fringe of the interference pattern. Intuitively, it can be understood as a configuration with very low background, in which null measurements can be performed and a gravitational wave signal has more chances to be detected. In order to stabilize the interferometer in this sense, a photodiode measures the intensity of interferometer output and feeds results back to a transducer that can change the position of one of the interferometer's mirrors.

This operation mode is obtained through a modulation technique (discussed in [8]), via an electro-optic phase modulator placed in front of the interferometer. In this situation, however, if

the mirrors have very low optical loss, almost all light is reflected back to the input laser. For this reason, a *power recycling mirror* is placed between the laser and the beam splitter, in order to form a perfect resonant cavity between this mirror and the rest of the interferometer. Moreover, it creates a power build-up inside the interferometer, that can be enough to reach a laser power of 750 kW, required to operate at full sensitivity, even if the laser enters the interferometer at most at 200 W [7].

Signal recycling

In order to make feasible for interferometers to detect gravitational waves, the match between the time spent by light travelling up and down the arms of the detector and the period of gravitational waves is fundamental [18]. This matching is achieved mainly by adjusting arm length and cavity finesse, both fixed by design. A mirror placed before the photo-detector recycles the signal back into the interferometer, where it resonates, thus being enhanced over a frequency bandwidth determined by the mirror reflectivity. In addition, the control of this mirror's position allows a precise tuning of the frequency at which the performance is peaked. The *signal-recycling mirror*, therefore, allows to adjust the matching condition to "tune" the detector's response to the frequency band of the waves. In Advanced LIGO, the signal-recycling mirror reflectivity has been chosen to increase signals from coalescing black hole and neutron star systems.

2.5 Noise sources

In general, the output signal of a detector is given by

$$s(t) = \xi(t) + n(t) \quad (2.20)$$

where $\xi(t)$ is the signal produced by the GW and $n(t)$ the noise. In order to describe and quantify noise, we consider the noise autocorrelation function

$$R(\tau) \equiv \langle n(t + \tau)n(t) \rangle \quad (2.21)$$

and define the *noise spectral density* (or noise spectral sensitivity, or noise power spectrum) $S_n(f)$ via the Wiener-Khintchin theorem [1]

$$\frac{1}{2}S_n(f) \equiv \int_{-\infty}^{+\infty} d\tau R(\tau)e^{i2\pi f\tau} \quad (2.22)$$

The noise of a detector is usually characterized by the *spectral strain sensitivity* (or *spectral amplitude*) $\sqrt{S_n(f)}$, which has dimensions $\text{Hz}^{-1/2}$.

Strains produced by gravitational waves near the Earth are of the order of 10^{-21} or lower, with a consequent displacement of interferometer mirrors below $\Delta L \sim 10^{-18}$. Therefore, in order to be able to detect them, noise levels of the detectors must have an amplitude spectral density at least lower than $\simeq 10^{-20}\sqrt{\text{Hz}}$ over the frequency range of the signal. Ground-based interferometers have a detection band of interest (10 Hz-10kHz) and a target strain sensitivity $h = 10^{-23}/\sqrt{\text{Hz}}$, [12]. Although in principle it should be possible to build laser interferometers limited only by the

Heisenberg uncertainty principle, from the practical point of view many sources of noise makes the achievement of such sensitivity very difficult. Typically, the sensitivity of a standard interferometer is limited by seismic noise and gravitational disturbance form environment at low frequencies, thermal noise at intermediate frequencies and shot noise at higher ones (see Fig.2.3).

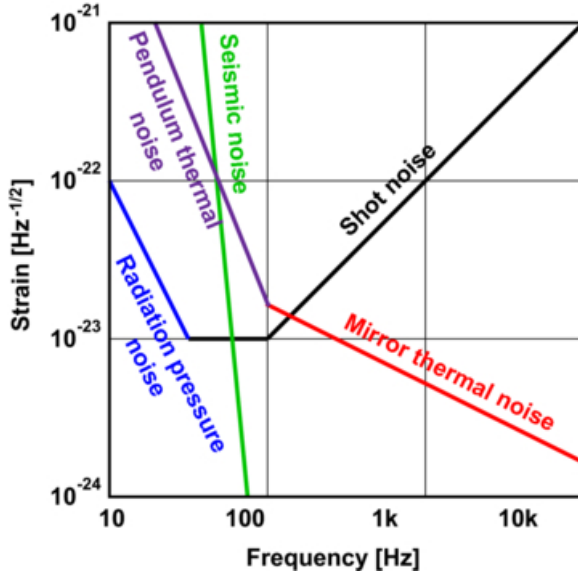


Figure 2.3: Strain sensitivity of a standard interferometer with contributions of major noise sources and corresponding frequencies at which they arise, [6]

2.5.1 Seismic noise

At low frequencies, one of the main sources of noise comes from external mechanical vibrations, both of anthropogenic and natural origin. In a reasonably quite site of Earth, it follows a spectrum (in all three dimension) of the order $\sim 10^{-7} f^{-2} m/\sqrt{Hz}$, therefore a huge attenuation is required [8]. A combination of active and passive damping systems is usually employed. Active damping consists in a series of devices that sense ground vibrations and perform counter-movements in order to keep the instrument still (for example the hydraulic external isolation system implemented in LIGO, [7]). On the other hand, for what concerns passive damping, on the arms plane isolation is provided by a multistage pendulum system. Indeed, for a simple pendulum the transfer function above resonance frequency falls as $1/f^2$, while for a N-stage system as $(1/f^2)^N$. Similarly, attenuation along vertical direction (since vertical noise is likely to couple to horizontal axis) is obtained with a spring. The LIGO interferometers employ a four-stage pendulum [7], while Virgo has an extremely effective isolation system, the Super Attenuator, which is expected to allow, at 10 Hz, a horizontal and vertical attenuation factor of 10^{-11} and 10^{-9} respectively [13][14].

2.5.2 Gravity gradient noise

Also known as Newtonian noise, it originates from fluctuations in the gravitational field that can couple with the suspended mirrors and cause an unwanted displacement. It can be caused by the motion of massive bodies but also by changes in densities of environmental media, like atmospheric

pressure. Since gravitational force cannot be screened out, two approaches have been proposed in order to reduce it [8]:

- Monitor and subtraction method, where an array of seismometers monitor the relevant ground motion with the goal to develop a noise model that can be subtracted from the signal
- Build the detector underground, away from the surface (hence from density fluctuations)

Although at few Hz Newtonian noise is overcame by the seismic one, and at slightly higher frequencies by thermal noise, also if their levels are pushed to lower and lower values, gravity gradient noise represents a substantial limit to sensitivity. Newtonian noise sets the fundamental low-frequency limit for ground-based interferometers, because it does not allow to gain sensitivity below a few Hertz.

2.5.3 Thermal noise

From fluctuation-dissipation theorem, we have that a thermal noise corresponds to mechanical dissipation. Without needing a detailed microscopic model of the dissipation mechanism, this theorem allows us to calculate the spectral density of the force responsible for thermal fluctuations. Performing calculations (details can be found in [1]), it is possible to prove that the displacement spectral density is proportional to the loss angle or loss factor $\phi(\omega)$. In the case of a mass hung on a spring, the loss factor is a measure of mechanical losses associated to the material of the spring.

We can distinguish between suspensions and test-masses thermal noise. The first group includes swinging and vertical motion in suspensions, together with violin modes that cause noise spikes between 300Hz and 1kHz.

Test-masses, instead, are affected by Brownian motion of the mirrors, approximately between 10 and 100 Hz. Moreover, one must take into account thermo-refractive fluctuations: the dielectric mirrors used in gravitational waves interferometers are composed by many layers of materials with different refractive indices. However, the refractive index is a function of temperature, hence temperature fluctuations induce variations also in mirrors refractive indices.

There exist two possible solutions to reduce thermal noise:

- Cool down the system.
- Since it depends on dissipations present in the system, which in turn are strongly related to the material used, search for materials with optimal properties.

2.5.4 Quantum noise

Quantum noise derives from the quantized nature of the electromagnetic field used to measure test mass displacements and represents the fundamental limit to sensitivity in most of the detection frequency band. It includes two different processes, laser shot noise and radiation pressure noise.

Laser shot noise

Laser output is naturally quantized in photons, therefore the measure of the output power arriving at the mirror can be interpreted as a count of the number of photons touching it. Any counting process of independent events follows a Poissonian statistics that, for large number of counts N , becomes a gaussian with standard deviation \sqrt{N} . This fluctuation in the number of photons produces an uncertainty in the measured power, leading, for a Michelson interferometer, to a strain sensitivity [1]

$$S_n^{1/2}(f)|_{shot} = \frac{1}{L} \left(\frac{\lambda_L h c}{\pi^2 P} \right)^{1/2} \quad (2.23)$$

Radiation pressure

Eq.2.23 shows clearly that shot noise can be reduced increasing laser power. However, a complementary effect should be taken into account: when a photon beam impinges a mirror and is reflected back, it transfers momentum to the mirror itself, causing a radiation pressure noise. If the pressure exerted on the mirror was constant, it could be simply compensated. The problem arises from the fact that fluctuations in the number of photons leads to changes in radiation pressure too, with a strain sensitivity [1]

$$S_n^{1/2}(f)|_{rad. pr.} = \frac{4}{ML(2\pi f)^2} \left(\frac{2\hbar\omega_L P}{c^2} \right)^{1/2} \quad (2.24)$$

where M is the mass of the mirror. Notice that, contrary to shot noise, it increases with \sqrt{P} . Therefore, if we increase the laser power with the aim to reduce shot noise, on the other hand we are increasing radiation pressure noise. For this reason quantum noise represents a fundamental limit to interferometers sensitivity.

Standard Quantum Limit

We have seen that the quantized nature of light leads to two different kinds of noise, laser shot noise and radiation pressure noise, that behave in opposite ways as functions of laser power. The resulting *Optical read-out noise*

$$S_n(f)|_{opt} = S_n(f)|_{shot} + S_n(f)|_{rad}, \quad (2.25)$$

at a given operation frequency, can be minimized by an optimal value of input power $P_{opt}(f)$, for which shot noise and radiation pressure noise are equal. The corresponding optimal strain sensitivity

$$S_n^{1/2}(f)|_{SQL} = \frac{1}{2\pi f L} \sqrt{\frac{8\hbar}{M}} \quad (2.26)$$

defines the *Standard Quantum Limit* (SQL), i.e. the quantum limit to sensitivity.

2.6 Ground-based interferometer response to a gravitational wave

As we have seen in previous section, there are many kinds of noise that affects ground-based interferometers. Hence, in general, the output signal of these detectors must take into account the noise contribution

$$s(t) = \xi(t) + n(t) \quad (2.27)$$

where $n(t)$ is the noise data time series and $\xi(t)$ the detector output signal due to a gravitational wave. $\xi(t)$ is the response of the detector to the real gravitational signal h_{ij} , to which $\xi(t)$ is related via the **antenna pattern** $F(\mathbf{n})$ [54][56]

$$\xi(t) = h_+(t)F_+(\theta, \phi) + h_\times(t)F_\times(\theta, \phi) \quad (2.28)$$

The antenna pattern contains the dependence of detector response to a GW on the wave direction, and is defined as [1]

$$F_A(\mathbf{n}) = D^{ij}e_{ij}^A(\mathbf{n}) \quad \text{for } A = +, \times \quad (2.29)$$

with $D^{ij} = \frac{1}{2}(\hat{\mathbf{x}}_i\hat{\mathbf{x}}_j - \hat{\mathbf{y}}_i\hat{\mathbf{y}}_j)$ detector tensor and $e_{ij}(\hat{\mathbf{n}})$ polarization tensor.

The explicit expression for antenna pattern depends on the source position in sky, given by the angles (θ, ϕ) and by the polarization angle ψ , which corresponds to the rotation angle in sky frame [4]:

$$F_+(\theta, \phi, \psi) = \frac{1}{2}(1 + \cos^2 \theta) \cos 2\phi \cos 2\psi - \cos \theta \sin 2\phi \sin 2\psi \quad (2.30)$$

$$F_\times(\theta, \phi, \psi) = \frac{1}{2}(1 + \cos^2 \theta) \cos 2\phi \sin 2\psi - \cos \theta \sin 2\phi \cos 2\psi \quad (2.31)$$

They can also be expressed in the detector frame, simply setting $\psi = 0$ [1]:

$$F_+(\theta, \phi,) = \frac{1}{2}(1 + \cos^2 \theta) \cos 2\phi \quad (2.32)$$

$$F_\times(\theta, \phi) = \cos \theta \sin 2\phi \quad (2.33)$$

The maximum value of either F_+ or F_\times is 1. From the previous equation it is possible to infer that a detector with perpendicular arms has some blind directions: if $\theta = \pi/2$ and $\phi = \pi/4$, both F_+ and F_\times become zero. From a qualitative point of view, one can also imagine that for a wave arriving perpendicular to the detector plane the effects on the arms is maximized, while if the propagation direction is along the arms bisector, both are stretched and compressed by same amount, therefore no effect can be detected.

2.7 Network of detectors

Gravitational waves detectors are almost omni-directional antennas, since, conversely to electromagnetic astronomical telescopes, they have a good sensitivity over a large area of the sky. The

problem arising from this feature is that gravitational waves detections will not automatically provide the source location in sky. It is possible to estimate it observing the same signal from detectors located in different places and triangulating the source position from the delay between arrival times in the various interferometers [4][55]. Furthermore, a single detector cannot observe the two polarizations of a gravitational wave at the same time, since it measures a combination of the two. A network of differently aligned detectors allows to improve sensitivity for both polarizations, as we will discuss in Section 4.1.2.

Finally, with a network of detectors, analysis can be performed in two different ways, coincidentally or coherently. In coincident detections events are first identified in single detectors, then temporal coincidence between detectors is required to select an event. Coherent analysis, instead, combines data streams from all detectors into one coherent statistics. With a coherent analysis, in a network of N_D detectors the visibility of a signal is improved by a factor $\sqrt{N_D}$ [4].

For this reason the aim is to build a network of multiple detectors worldwide (figure 2.4):

- Advanced LIGO: consists of two interferometers with arm-length 4 km, one located in Livingston (Louisiana) and the other one in Hanford (Washington State). A third LIGO interferometer has been approved to be built in India.
- Advanced VIRGO: 3km-arms interferometer, located at Cascina (Pisa), in Italy.
- KAGRA: under construction near Kamioka, Japan, it will be the first interferometer with kilometric arms located underground and will employ cryogenic technologies
- GEO600: detector in Hannover, with 600m arms, it is mainly used to test new technologies.

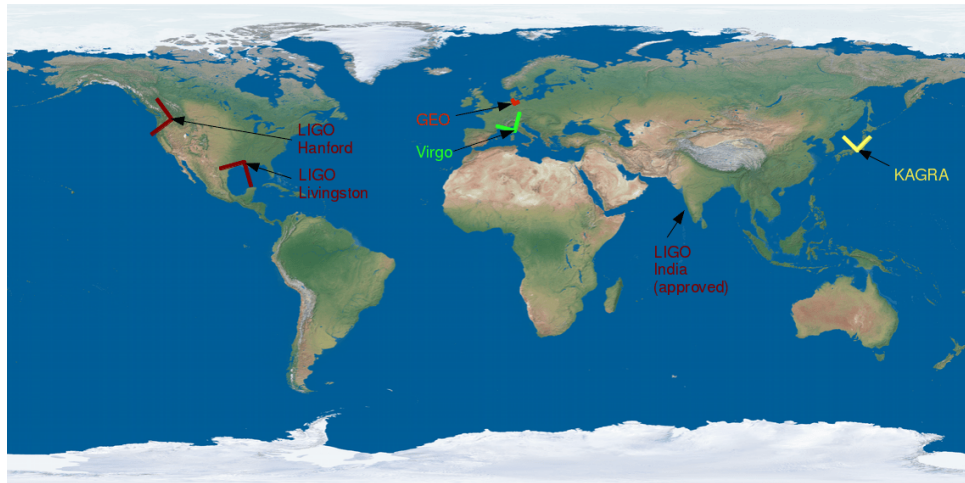


Figure 2.4: Representation of the location of various GW detectors planned to form a worldwide network. *Credits: The Virgo Collaboration/LAPP and Tom Patterson*

2.8 The detections

After a period of technological upgrade, the advanced LIGO detectors became operational in 2015. During the first observing run O1, from September 12th, 2015 to January 19th, 2016, the first direct

detection of a gravitational wave was made, Fig.2.5. The gravitational-wave event GW150914 was produced by a black hole binary, with component masses estimated to be $36^{+5}_{-4} M_{\odot}$ and $29^{+4}_{-4} M_{\odot}$ and final black hole mass $62^{+4}_{-4} M_{\odot}$, with $3.0^{+0.5}_{-0.5} M_{\odot}c^2$ radiated in gravitational waves, [15]. It denoted a major breakthrough, because it was the first direct observation of gravitational waves and furthermore demonstrated the existence of binary stellar-mass black hole systems. A second BBH signal was detected on December 26, 2016, with initial black hole masses $14.2^{+8.3}_{-3.7} M_{\odot}$ and $7.5^{+2.3}_{-2.3} M_{\odot}$, [16]. After a further upgrade and commissioning, advanced LIGO started the second observation run O2 on 30th November, 2016, and it lasted until August 25th, 2017. Advanced Virgo joined O2 on 1st August, 2017, so it was operational on August 17th, when a gravitational wave signal from the coalescence of a neutron star binary was detected [31], setting the beginning of multi-messenger astronomy era. At the moment, new modifications are being implemented on the three detectors, in order to improve further the sensitivity for the third observation run, O3, planned for Spring 2019.

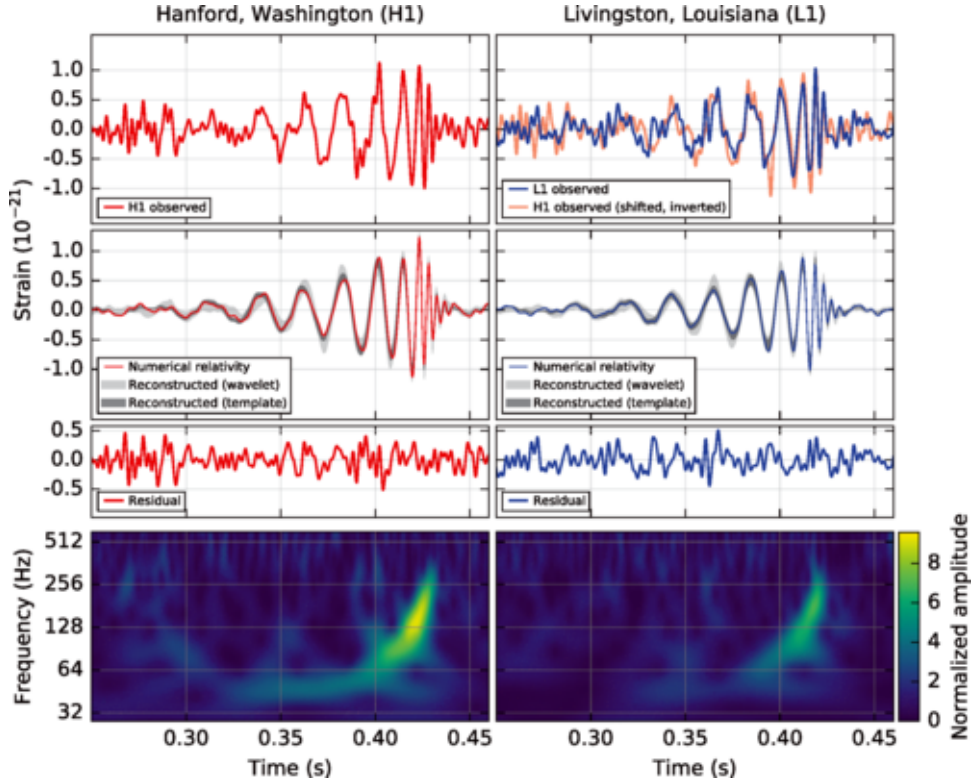


Figure 2.5: Gravitational-wave event GW150914 observed by the LIGO-Hanford (left panels) and LIGO-Livingston (right panels). *Top row:* strain. *Second row:* gravitational wave strain projected onto each detector in the $35 - 350$ Hz band. *Bottom row:* time-frequency representation (see Section 4.1.2) of the strain data, showing signal frequency increasing over time. [15].

Chapter 3

Neutron stars

In this chapter I describe the GW sources we are interested in for our analysis, namely BNS coalescence. The first part contains a general outlook on neutron stars astrophysics, their structure, population and the issue of equation of state describing their matter. The second part, instead, deals with BNS and their coalescence, with particular attention to the post-merger phase. The last section is dedicated to the BNS detection made in August, 2017.

3.1 History

Neutron stars are the most compact stars known in the Universe, with typical masses comparable to the mass of the Sun but radii of the order $R \sim 10^{-5} R_\odot$. Their existence was predicted by Baade and Zwicky a few years later neutron discovery by Chadwick, in order to account for the enormous amount of energy released in supernovae explosions [21]. Since then, many attempts were made to understand and describe better what neutron stars were and how they should behave, in particular for what concerns the equation of state describing matter at such high densities. For a few decades, studies on neutron stars remained purely theoretical, until the first observation made in 1967. Two years before Antony Hewish started to construct at Cavendish Laboratories a new radio telescope, with very high temporal resolution, with the aim to study scintillations of radio sources produced when their radiation passes through inhomogeneities of solar wind in the interplanetary space. Two years later, Jocelyn Bell, the PhD student supervised by Hewish, discovered a weak, variable radio source outside the solar system, with a very stable period [21][20]. In astronomy, rapid pulses like the ones detected can be explained only by binary, pulsating and rotating stars. Among those possible sources, the only one compatible with observations was the last one. Some indecision remained about what kind of star, between white dwarfs and neutron stars, could produce the observed pulses, until the discovery of Crab pulsar PSR0531-21. Since a white dwarf cannot sustain its very short period of 0.0333s without disintegrating, it definitely excluded white dwarfs as a possible source of these signals, leading to the conclusion that *pulsars* were actually rotating neutron stars. Moreover, the discovery of pulsars associated with Vela and Crab supernova remnants supported the original hypothesis of Baade and Zwicky regarding their connection with supernovae [21].

3.2 Neutron Stars formation

The evolution of stars can be described as a continuous struggle between gravitational collapse and the radiation pressure provided by nuclear reactions. In the star's core, starting from hydrogen, heavier and heavier elements are burned. When the burning fuel is exhausted, the reaction stops, the star contracts and heats up, and such increased temperature allows it to burn the next element. At the end, stars result in an onion-like structure, the more massive ones ending up with an iron core, others stopping at a carbon-oxygen composition. Anyway, in all cases, at a certain point the star runs out of fuel and gravitational collapse sets on. Depending on the core mass, the dead star could have different fates. If the mass is lower than the Chandrasekhar limit, $M_{Ch} \simeq 1.4M_{\odot}$ [20], the star can be supported by electrons degeneracy pressure and becomes a white dwarf. Slightly more massive cores, instead, find the new equilibrium configuration in a neutron star, supported by neutrons degeneracy pressure. Finally, even more massive stars are forced to collapse to a black hole. Neutron stars are thought to originate from core-collapse supernovae, whose progenitors are stars with masses between $8 - 24M_{\odot}$. When the supergiant progenitor runs out of fuel, the core begins to collapse due to gravitational pull. The subsequent bounce produces an expanding shock wave that blows away the outer layers, leaving behind the supernova remnant. The collapse releases an enormous amount of energy, of the order of $10^{53}erg$, and can be accompanied by a powerful neutrino outburst. The proto-neutron star formed in this way is hot, with an internal temperature $T \sim 10^{11}K$, opaque to neutrinos and larger than usual neutron stars, and lives for about one minute before becoming an ordinary neutron star transparent to neutrinos [19].

Another possible formation channel of neutron stars includes *accretion induced collapse*: a white dwarf, usually component of a binary, accretes matter until its mass exceeds Chandrasekhar limit. However, most of the times, this process leads to a thermonuclear explosion, that disrupts the compact object [19].

3.3 Neutron stars equation of state

Stellar structure is usually described by four equations

- Equation of hydrostatic equilibrium: it defines the balance between gravitational pull and pressure gradient of the hot gas inside the star, provided by energy released in the nuclear reactions in their cores.
- Mass conservation
- Equation for energy generation: it provides the energy generation rate within a star, that strongly depends on the energy production mechanism.
- Equation for energy transport: in a star, energy can be transported via two mechanisms, convection and radiation, with radiative transport resulting more effective in main sequence stars.

Anyway, when dealing with neutron stars two big differences must be taken into account: pressure is provided by fermions degeneracy and not by nuclear reactions, and matter's extreme compactness requires general relativity to describe it.

In 1939 Tolman, Oppenheimer and Volkoff found the spherically symmetric and static solution to Einstein equations in the presence of a matter fluid (some years before Schwarzschild found the solution in vacuum, generally used to describe black holes or space outside a spherical star). Consider the static metric [3]

$$ds^2 = -e^{A(r)}dt^2 + e^{B(r)}dr^2 + r^2d\Omega^2 \quad (3.1)$$

and the Einstein equations

$$G_{\mu\nu} = 8\pi T_{\mu\nu}. \quad (3.2)$$

For the stress tensor

$$T_{\mu\nu} = (\rho + p)u_\mu u^\nu + pg_{\mu\nu} \quad (3.3)$$

the condition $u_\mu u^\mu = -1$ holds, implying [5]

$$u_\mu = (e^A, 0, 0, 0) \quad T_{\mu\nu} = \text{diag}(e^{2A}\rho, e^{2B}p, r^2p, r^2psin\theta) \quad (3.4)$$

If we compute the Ricci tensor components in the above static metric (3.1), the (rr)- and (tt)-components of Einstein equation can be written as [5]:

$$(tt) - component \quad \frac{1}{r^2}e^{-2B}(2rB' - 1 + e^{2B}) = 8\pi\rho \quad (3.5)$$

$$(rr) - component \quad \frac{1}{r^2}e^{-2B}(2rA' + 1 - e^{2B}) = 8\pi p \quad (3.6)$$

where the prime indicates derivative with respect to r . With the substitution

$$m(r) = \frac{r}{2}(1 - e^{-2B}) \quad (3.7)$$

the (tt)-component yields

$$m' = 4\pi r^2\rho \quad (3.8)$$

which formally resembles the newtonian equation for mass conservation. Here the concept of mass is substantially different from the newtonian case, since in general relativity the total energy density inside a star is given not only by matter but also by the gravitational energy keeping it together. To take into account such binding energy, the correct integration of 3.8 gives a quantity [21]

$$\bar{M} = M + E_{binding}. \quad (3.9)$$

Instead, for what concerns the (rr)-component, using definition 3.7 it becomes [5]

$$A' = \frac{m(r) + 4\pi r^3 p}{r[r - 2m(r)]} \quad (3.10)$$

Together with the Einstein equation components we must consider the energy conservation $\nabla_\mu T^{\mu\nu} = 0$, that yields the relation [5]

$$(\rho + p)A' + p' = 0. \quad (3.11)$$

Combining Eq.3.10 and Eq.3.11, we obtain the *TOV equation* [21]

$$p' = -\frac{(\rho + p)(m(r) + 4\pi r^3 p)}{r[r - 2m(r)]} \quad (3.12)$$

To solve this equation, proper boundary conditions are required. In particular, the physics of the system imposes:

$$\begin{cases} m(r) = M_*, P(r) = 0 & \text{for } r > R_* \\ m(0) = 0, \rho(0) = \rho_c & \text{for } r = 0 \end{cases} \quad (3.13)$$

with M_* and R_* mass and radius of the neutron star, and ρ_c its central density.

Moreover, an equation of state must be provided, namely a relation that bounds pressure and energy density of matter inside the star. However, we do not know the equation of state of matter at such high densities yet.

The lack of knowledge about the equation of state characterizing their matter represents the main issue for neutron stars. Modern research tries to combine astrophysical observations with results of experiments on nuclear matter properties, especially regarding nuclear symmetry energy (see [22] for a review), in order to extract information about nuclear matter equation of state at high densities.

3.4 Neutron stars mass and radius

The equation of state turns out to be crucial in determining many neutron stars properties, like maximum mass and mass-radius relation. The existence of a maximum mass is a direct consequence of general relativity, in particular a theorem by Buchdal states that, for a spherical star, no equilibrium solution can be found for $R < \frac{9}{8}R_s$, with $R_s = 2MG/c^2$ the Schwarzschild radius (hence $\frac{R}{M} < \frac{9}{4}\frac{G}{c^2}$) [21].

The first attempt, by Oppenheimer and Volkoff, to determine the maximum mass possible of a neutron star gave $0.72M_\odot$, too small with respect to the available measurements of NS masses. The problem arose because their calculation considered non-interacting neutrons: this result showed clearly that the dominant contribution of strong repulsive interaction must be taken into account.

As shown in Fig. 3.1, the relation between mass and radius of neutron stars is really EoS-dependent. Therefore, a simultaneous measurement of these two quantities could give important information about NS equation of state.

Mass determination from binaries with a pulsar is one of the most accurate mass measurements concerning neutron stars. In classical gravity, the orbit can be described by five Keplerian parameters: the orbital period P , the projection of pulsar's semimajor axis $a \sin(i)$ (with i inclination angle of the orbital plane with respect to the line of sight), the orbital eccentricity e , the longitude of periastron ω and the epoch of periastron passage T_0 . Such orbital parameters determine the so-called mass function [20]

$$f(m_1, m_2, i) = \frac{(m_2 \sin i)^3}{M^2} = \left(\frac{2\pi}{P}\right)^2 (a \sin i)^3 \quad (3.14)$$

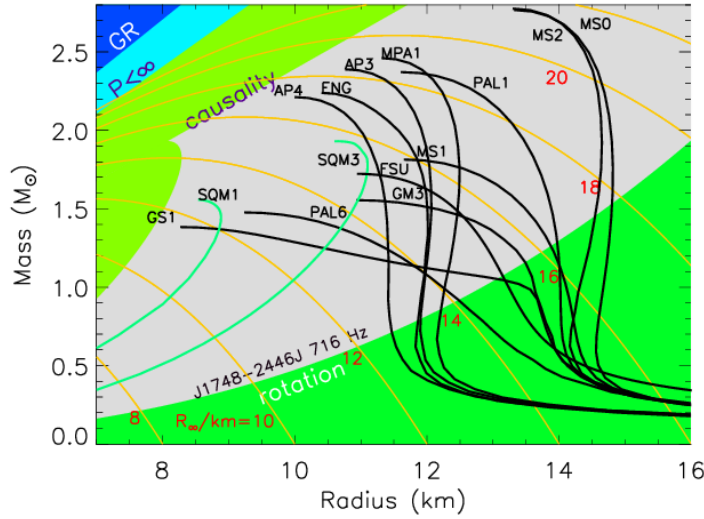


Figure 3.1: Typical mass-radius curves for different equations of state. Regions of the plane excluded by general relativity, finite pressure, and causality are indicated. [22]

where m_1 is the mass of the pulsar, m_2 of the companion and $M = m_1 + m_2$ the total mass. Anyway, this function is not sufficient to determine the single component masses. If the system's compactness requires general relativity to describe it, more parameters, called "post-Keplerian", are needed: $\dot{\omega}$, \dot{P} , gravitational redshift and Shapiro delay. If at least two of them are known, the single masses can be determined. Up to now, the largest well-measured mass is $1.9 \pm 0.04 M_{\odot}$ for PSR J1614-2230.

On the other hand, neutron stars radii are usually inferred from thermal emission and X-ray bursts, but large uncertainties affect these kinds of measurements.

3.5 NS structure

Although the details of a neutron star model depend on the equation of state, a general structure can be identified, dividing it into five regions (Fig.3.2):

- **Atmosphere:** a thin plasma layer, with thickness from tens centimeters in hot NS (effective temperature $\sim 3 \times 10^6 K$) to few millimeters in cold ones ($T \sim 3 \cdot 10^5 K$). Here the spectrum of thermal electromagnetic radiation carries information about the parameters of the surface layer, such as effective surface temperature, surface gravity, chemical composition, strength and geometry of surface magnetic field.
- **Outer crust (outer envelope):** it extends for some hundred meters from atmosphere bottom to the layer with density $\rho = \rho_{ND} \sim 4 \cdot 10^{11} g/cm^3$. Here pressure is mainly provided by electrons and it is called crust because a larger fraction is usually solidified. In the outer layers, at low densities, the minimum-energy compromise between Coulomb

repulsive force among protons and nuclear attractive force between nucleons translates in all neutrons and protons being enclosed in iron nuclei. At $\rho \sim 10^6 g/cm^3$ electrons become relativistic and soon thereafter their energy increases enough to transform protons present in the iron nuclei into neutrons via electron capture $p^+ + e^- \rightarrow n + \nu_e$. At higher densities, **neutronization** takes place, namely a process that enriches nuclei with neutrons, producing nuclei such as Fe^{56} , Ni^{62} , Ni^{64} , Ni^{68} , Kr^{86} . This is possible because the β -decay process $n \rightarrow p^+ + e^- + \bar{\nu}_e$, that in ordinary conditions would make neutrons decay into protons, is prevented by the absence of available states for emitted electrons, due to their complete degeneracy.

- **Inner crust (inner envelope):** in this layer thick a few kilometers, density ranges from ρ_{ND} to $\sim 0.5\rho_0$, with ρ_0 nuclear saturation density. When the density reaches $10^{11} g/cm^3$, the minimum-energy configuration requires that some neutrons are found outside the nuclei. The appearance of such neutrons is called **neutron drip** and causes the creation of a three-component mixture: a lattice of neutron-rich nuclei plus non-relativistic degenerate neutrons and relativistic degenerate electrons. Among degenerate neutrons Cooper pairing can occur, leading to superfluidity. As the density grows further, the number of free neutrons increases as that of electrons declines, and the neutron degeneracy pressure exceeds the electrons one when $\rho \simeq 4 \times 10^{12} g/cm^3$. In the bottom layers, with density $1/3\rho_0 \leq \rho \leq 1/2\rho_0$, some models predict that nuclei can become essentially non-spherical and form a *mantle*.
- **Outer core:** it is several kilometers thick and has density $0.5\rho_0 \leq \rho \leq 2\rho_0$. When the density approaches ρ_0 , the nuclei effectively dissolve and neutrons inside and outside nuclei cannot be distinguished anymore, resulting in a fluid mixture of free neutrons, protons, electrons and possibly muons ($npe\mu$ composition) dominated by neutron degeneracy pressure. The state of this matter is determined by electric neutrality and β -equilibrium (balance between electron capture and β -decay inhibited by the presence of degenerate electrons), according to which, increasing density further, the ratio n:p:e reaches the limiting value 8:1:1 [21]. All $npe\mu$ -plasma components are strongly degenerate, electrons and muons form almost ideal Fermi gases, while neutrons and protons can be in a superfluid state.
- **Inner core:** the central and most mysterious region of a neutron star, with density $\rho \geq \rho_0$, believed to reach values up to 15-16 ρ_0 . Several hypothesis have been made for what concerns the inner core composition and equation of state, among which we mention:
 - ★ Hyperonization, namely the appearance of hyperons, above all Λ
 - ★ Pion and kaon condensation, in particular π^- production from the decay of a neutron into a proton and negative pion occurs spontaneously at $\rho > 2\rho_0$
 - ★ Phase transition to quark matter, composed of up, down and strange quarks

3.6 Neutron stars population

Some general properties of neutrons stars were predicted even before their observation:

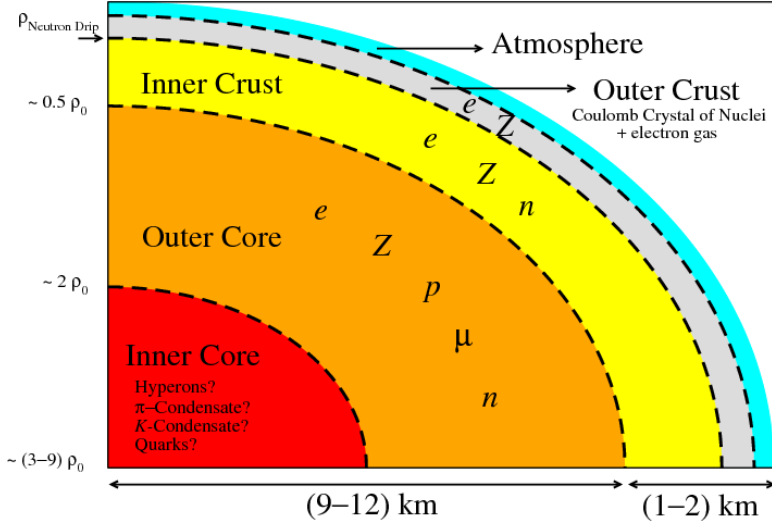


Figure 3.2: Schematic representation of neutron star structure, [24]

- NS must rotate very rapidly: even if the progenitor's core was slowly rotating, the conservation of angular momentum implies that the great decrease in radius it undergoes leads to a fast rotation for the new-born neutron star
- NS should have strong magnetic fields
- Since they are formed in supernova explosions, with $T \sim 10^{11} K$, NS are initially very hot. The cooling process occurs mainly through neutrino emission, since their very small cross section of interaction with matter allows them to escape unimpeded carrying away energy.

Neutron stars are generally divided into radio pulsars, gamma-ray pulsars and X-ray pulsars, depending on the spectral range where emission is observed (however, some NS, like the Crab pulsar, show pulsation in all these spectral bands). Moreover, we distinguish between isolated neutron stars and neutron stars in binaries.

Radio pulsars: are isolated, rotating, magnetized neutron stars with periods $P \gtrsim 30ms$. Pulses are currently explained with the so-called *lighthouse model*: as the neutron star spins, charged particles are accelerated along magnetic field lines and form a beam. These accelerating particles emit electromagnetic radiation, detected as a radio pulse every time the beam crosses the observer's line of sight. Therefore, the pulse period, which can be accurately measured, simply corresponds to the NS rotation period. One of the most meaningful parameters describing these objects is \dot{P} , the rate at which period changes with time. In fact, NS rotating model implies that the star gradually slows down, since emitted electromagnetic radiation carries away kinetic rotational energy, and the rate at which this happens depends on the braking mechanism. According to the model described above, the star's magnetic dipole must be misaligned with respect to its rotational axis of a certain angle, exhibiting a varying dipole moment when observed at large distances: the radiation of this magnetic dipole extracts rotational energy from the star. Although \dot{P} measurements show that small corrections due to other slowing processes should be taken into

account, assuming that magnetic braking constitutes the dominant pulsar slow-down mechanism, pulsar age and surface magnetic field can be estimated [20]:

$$\tau = \frac{P}{2\dot{P}} \quad B_s \approx 3 \times 10^{15} (P\dot{P})^{1/2} \quad (3.15)$$

According to these calculations, the age of isolated radio pulsars ranges from $10^3 - 10^4$ years for the young ones, usually associated with the remnant of the supernova in which they were formed, up to $\sim 10^8$ years for old pulsars, whether, for what concerns magnetic flux, its density has been estimated to lie between $10^7 - 10^9 T$. These properties are generally summarized in a $P - \dot{P}$ diagram (Fig.3.3), which can be considered an equivalent of Hertzsprung-Russel diagram used for stars, since the position of pulsars on this plot can be interpreted as an evolutionary sequence.

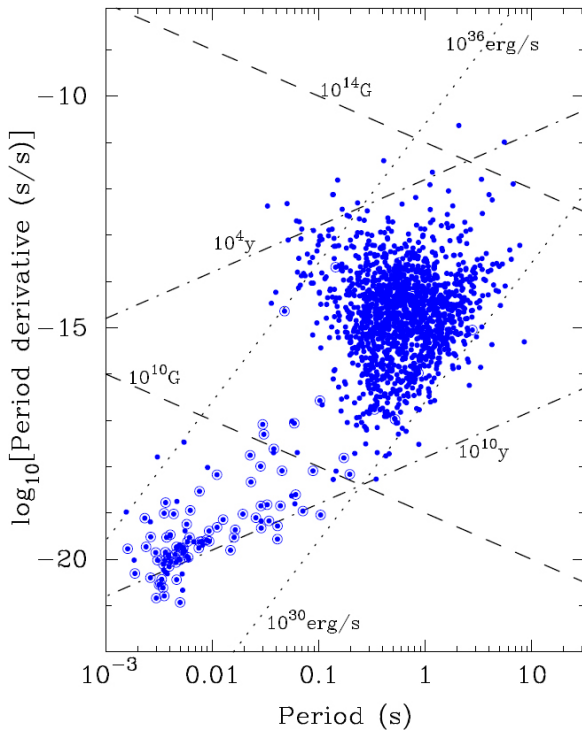


Figure 3.3: Plot of \dot{P} as a function of P , known as $P - \dot{P}$ diagram. Open circles highlight binary pulsars. Lines of characteristic age (dash-dotted), constant magnetic field (dashed) and spin-down energy loss rate (dotted) are shown, [23].

X-ray binaries: NS can also be found in binaries, usually with main sequence stars, white dwarfs or another neutron star (up to now no binaries with a black hole have been observed). In X-ray binaries the NS accretes matter from the companion, feeding an X-ray emission. Many of them have been observed and usually they are distinguished in *low-mass X-ray binaries* (some of which have been identified in globular clusters) and *high-mass X-ray binaries* (as Cygnus X-1 and Vela X-1), according to the mass of the companion star. In general, binary pulsars with high mass companions ($M_c \gtrsim 1M_\odot$) evolve on more eccentric orbits, $0.15 \lesssim e \lesssim 0.9$, while low-mass binaries ($M_c \lesssim 0.7M_\odot$, usually white dwarfs) tend to have a circular orbit, with $10^{-5} \lesssim e \lesssim 0.01$, since the tidal forces during the accretion process tend to circularize it [23]. The dynamical parameters

of the X-ray binary can be used to estimate the mass of the neutron star, but, as we said before, Keplerian parameters do not provide an estimate of the single-component masses.

Binary pulsars: binaries containing a pulsar play a central role in astrophysics, since the compactness of both their components requires general relativity to describe these systems. This implies that the study of binary pulsars provides very sensitive tests of General Relativity and an accurate measurement of NS masses.

Millisecond pulsar: NS with a very short (order of ms) and stable pulses, condition which implies that they should have weak magnetic fields. Most of them are found in binaries, which provides an explanation for such very short periods: mass transfer from the primary star onto the neutron star transports angular momentum, causing a spin-up. Indeed, accretion radius around the star is determined by magnetic pressure, and a weak one allows accretion very near the NS surface, with a subsequent larger spin-up. Association of millisecond pulsars with binaries suggests that they can be found in globular clusters too, where some low-mass X-ray binaries have been observed. Some are also observed as isolated objects, probably as a result of the binary disruption caused by the companion star explosion.

Magnetars: they are a particular category of NS, including soft γ -ray repeaters and anomalous X-ray pulsars, with periods $2 \lesssim P \lesssim 15\text{s}$ but very large spin-down rates. They are generally characterized by very short lifetimes and large magnetic flux densities, much greater than those of normal radio pulsars population, and their source of energy must somehow involve internal magnetic field, since rotation is too slow to account for it. These objects could also represent extreme example of normal radio pulsars with very strong magnetic fields affecting their emission.

3.7 Neutron star binaries

3.7.1 Formation channels of neutron star binaries

We saw that neutron stars are commonly accepted to be one of the possible fates of dead stars. More uncertain is the formation process of neutron stars binaries, whose existence has been confirmed by many astrophysical observations. The general picture, usually referred to as *standard channel*, is reported in Fig.3.4: in a binary system made of two massive stars, the more massive one leaves the main sequence, goes through a giant phase and finally undergoes a supernova explosion, leaving behind the most compact neutron star of the future binary. Then the secondary star moves off the main sequence and expands to fill its Roche lobe. During the following phase, named *Common Envelope* (CE) phase, the first neutron star orbits in the extended outer layers of the secondary star. Although still not completely understood, the CE represents a crucial stage for the formation of a BNS, because the dynamical friction that characterizes this phase could shrink the stars' separation to values that allow them to merge within a Hubble time.

Moreover, this severe separation reduction releases energy, until the secondary star expels its envelope, leaving behind its core. At this point, its exposed helium-core undergoes a supernova

explosion, which can unbind the system or result in a tight binary, depending on the magnitude and orientation of the supernova kick. It could happen that during the CE phase the primary collapses to a black hole, generating a BH-NS system, which is very similar to a BNS under many aspects. This evolutionary pathway affects differently the parameters and properties of the two NS in the binary: while the primary could accrete matter from the companion star, during the CE phase or with some stable mass transfer episode, resulting in a rapid rotation and loss of magnetic field, the secondary, that never accretes matter, is likely to spin down but maintain a strong magnetic field [26].

Another possible formation channel of BNS systems may be the dynamical interaction of two isolated neutron stars in dense stellar regions like globular clusters. This process, called *dynamical capture*, produces binaries with higher ellipticities with respect to the ones formed via standard channel. Although it is not known yet what fraction of BNS would be produced by this process, it is expected that such binaries form a much smaller population.

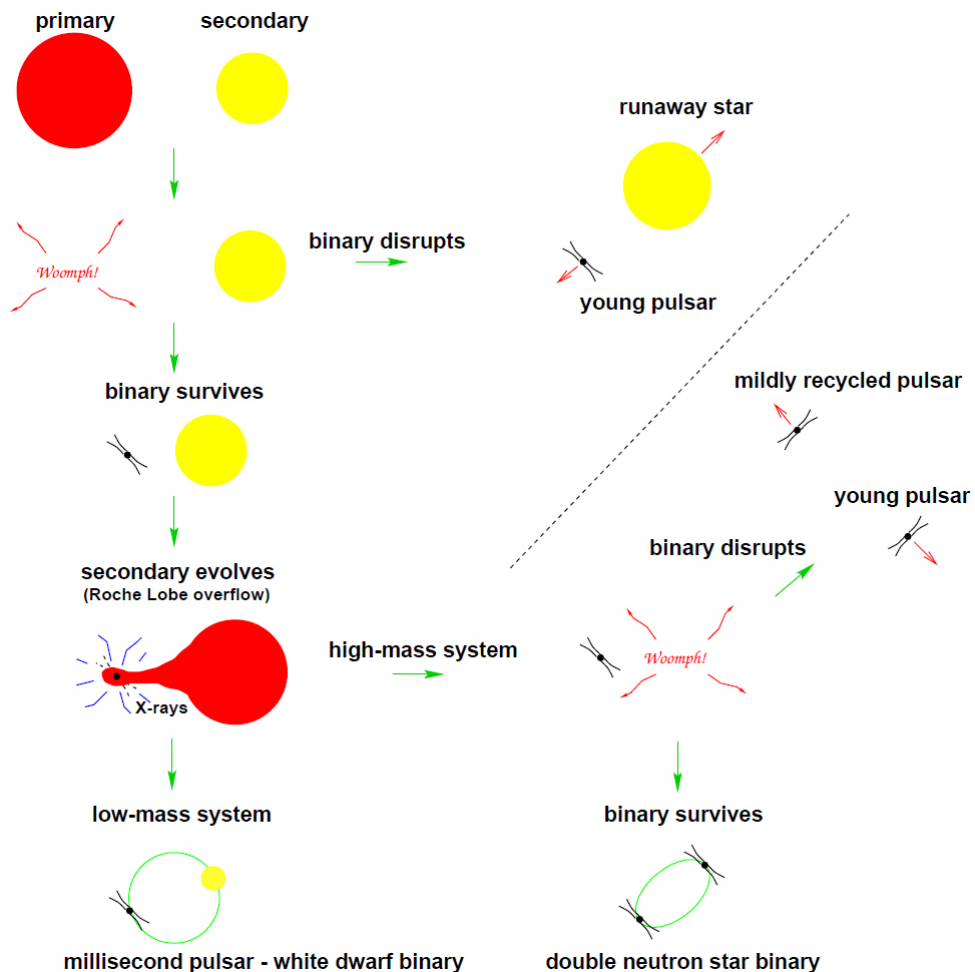


Figure 3.4: Cartoon showing the *standard formation channel* of a binary neutron star from a massive binary, from [26]

3.7.2 Binary merger stages

The evolution of a binary NS system is usually divided into three phases: inspiral, merger and post-merger (or ringdown).

After the binary formation, the two NSs orbit around each other for millions of years, evolving on the radiation-reaction timescale, namely the timescale set by the loss of energy and momentum via gravitational radiation. During this **inspiral phase** the binary orbital distance (and therefore the orbital period) progressively decays, until the NS separation becomes sufficiently small to make finite-size effects, like tidal deformation, important. While the inspiral phase can be efficiently described by a Quasi-Equilibrium formalism with a Post-Newtonian expansion, when the radiation timescale becomes comparable to the dynamical one, i.e. at small separations, only full GR simulations (implemented via Numerical Relativity) can describe the system.

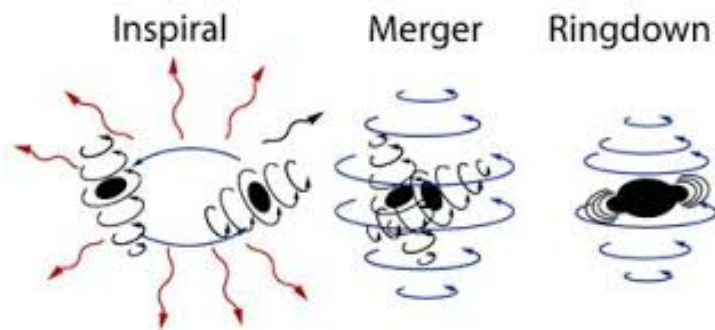


Figure 3.5: Cartoon representing the main stages of a compact object binary coalescence.

When the binary separation becomes only few times the NSs radii, the BNS enters the so-called **merger phase**, a dynamical instability sets on and the stars plunge together.

During the **post-merger** phase the system settles to a new dynamically stable configuration, where the mass and rotational features of the remnant determine the gravitational wave signal form. As shown in figure 3.6, depending on the binary mass there are different possible fates for the remnant: if the total mass is large enough, the NSs promptly collapse to a black hole, while if it is less than the maximum mass supported by the nuclear matter EOS a new stable NS is formed. Finally, an intermediate total mass leads to the formation of a *supramassive* or *hypermassive* neutron star, that eventually collapses, with different timescales, to a black hole. The post-merger phase dynamics and the possible remnants will be analyzed in more details in next section.

3.7.3 Post-merger

Every EOS used to describe matter in neutron stars provides a maximum mass that can be supported by nuclear reactions pressure against gravitational collapse. Anyway, rotation can increase this value: numerical calculations [29] performed with various EOS have shown that, in general, the maximum mass for a spinning neutron star $M_{max,s}$ is by 15 – 20% larger than M_{max} . Neutron stars with a mass above M_{max} but below the limit for a uniformly rotating NS are referred to as **Supramassive** (SMNS). On the other hand, if the NS is differentially rotating, namely the inner region rotates faster than the envelope, the centrifugal force can help supporting the self-gravity of

the remnant, implying a higher allowed maximum mass. Such differentially rotating neutron stars with mass exceeding $M_{max,s}$ are called **Hypermassive** neutron stars (HMNSs).

In general, SMNS are stable against gravitational collapse until angular momentum is present. The typical angular momentum dissipation process in this case is electromagnetic emission such as magnetic dipole radiation, with a dissipation timescale typically much longer than 1s. For HMNS, instead, instability could arise also due to angular momentum transport, that can happen via various possible processes. A part from purely hydrodynamical effects, if a magnetic field is present, angular momentum can be transported also due to magnetic winding and the effective viscosity caused by magnetorotational instability (MRI). For strong magnetic fields ($B \geq 10^{15} G$), their typical timescales are similar, of the order of $\sim 10^2 ms$.

Finally, in general, also thermal effects should be taken into account. Neutron stars are usually treated as cold, i.e. assuming that they are in a zero-temperature state, but during the merger process the temperature of the remnant can be increased up tp 30-50 MeV, [25]. The thermal pressure P_{th} gained with this temperature increase is $\sim 10\% P_{cold}$, where P_{cold} represents the cold-part pressure caused by the repulsive nuclear force. Therefore, we can consider [25] that both M_{max} and $M_{max,s}$ are increased by $\sim 0.1 M_\odot$ as a consequence of these thermal effects. Such thermal energy will be finally dissipated in a short timescale $\sim 1 - 10 s$ through neutrino cooling.

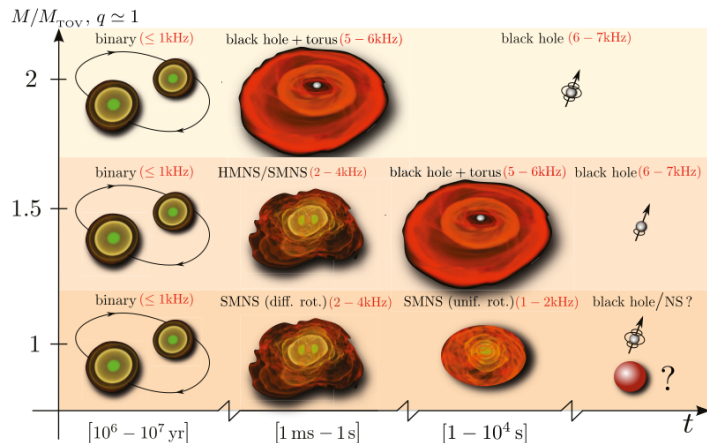


Figure 3.6: Schematic representation of the various stages in the evolution of an equal-mass neutron star binary. Depending on the initial total mass, the binary can collapse promptly to a black hole surrounded by a torus (top row), or produce an HMNS (or a SMNS) that, in the end, collapse to a black hole and a torus (middle row), or lead to a SMNS (first differentially and then uniformly rotating) that eventually yields a black hole or a non-rotating neutron star (bottom row). the typical frequencies of gravitational waves emitted in the different phases are indicated in red. [28]

Figure 3.6 schematically represents the evolution of a BNS depending on its total mass M , measured as a ratio with respect to the maximum allowed mass for a static isolated neutron star M/M_{max} . If the progenitor system is very massive, say with $M/M_{max} \sim 1.5 - 2.0$, the merger will result in a prompt collapse to a rotating black hole surrounded by a hot accretion torus. The torus will then accrete to the black hole within a timescale determined by gravitational

radiation, magnetic fields or viscous processes, depending on the most efficient process to remove angular momentum. Anyway, all of these timescales are estimated to be of the order $1 - 10s$, and the final product is an isolated rotating black hole in vacuum. If the remnant has mass not too high but still above M_{max} , corresponding to $M/M_{max} \sim 1.3 - 1.5$, the result will be a HMNS, dynamically unstable due to its large angular momentum and shear, leading to nonlinear instabilities. Following the angular momentum dissipation or transport processes described above, the HMNS could become unstable against gravitational collapse and therefore collapse to a black hole plus torus configuration as the one described for the previous case, or slow-down to a uniformly rotating NS, evolving to a SMNS, which in turn loses angular momentum until it collapses to a rotating black hole with an accretion torus. Since SMNS could also be differentially rotating, the merger remnant, if $M/M_{max} \leq 1.3M_\odot$, may be directly a SMNS, which evolves to a uniformly rotating SMNS and then to a black hole as before.

This general description based on mass gives an idea of the evolution of the system, but the fate of a BNS, with a given mass, can be slightly different depending on the EOS describing the NS. In general, the mass of the two NS in the binary are not sufficient to determine the system evolution, but also the EOS is required.

Many properties of this post-merger remnant, from the lifetime (determined by the evolution timescale), to the gravitational spectrum and the final torus characteristics depend on the EOS and mass of the progenitor neutron stars.

3.7.4 Gravitational waves from BNS mergers

The detection of gravitational waves emitted by the post-merger of a BNS coalescence could play a fundamental role in determining some properties of neutron stars and therefore gather information about the equation of state describing their matter. In particular, from the dominant oscillation frequency of the post-merger remnant, that in the case of HMNS or SMNS lies between $1 - 4\text{ kHz}$, one can obtain accurate simultaneous measurements of mass and radius. Moreover, if more binaries with different masses are detected, the maximum mass for a non-rotating NS, the corresponding radius and the maximum central density could be inferred [27].

In a work of 2016 [30], Takami and Rezzolla performed an analysis of gravitational wave signals emitted by 56 simulated binaries, with six different equations of state and ten possible values of masses. The study includes inspiral, merger and post-merger phase, and is focused on the spectral characterization of gravitational waves signal.

As a first result, they showed that the gravitational waveform depends on the equation of state and the binary mass (Fig.3.7).

In a deeper analysis, they considered the spectral properties of these gravitational waves signal, concluding mainly that:

- Gravitational wave frequency at the maximum amplitude, f_{max} , is related to the tidal deformability of the two stars
- The post-merger signal can be divided into a transient phase, lasting a few milliseconds, and a quasi-stationary phase, with different characteristics

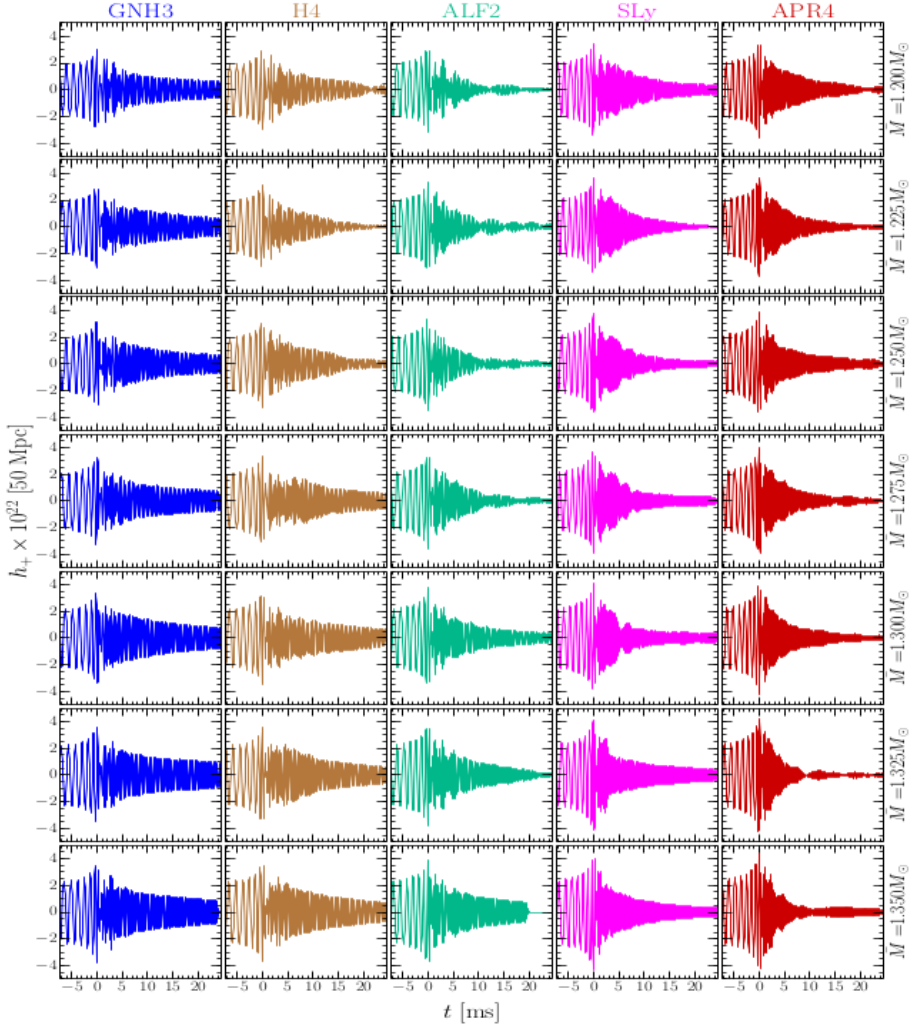


Figure 3.7: Gravitational waveforms for various equations of state. Each row corresponds to a different gravitational mass of the binary. All these models have formed long-lived HMNS with $\tau > 20\text{ms}$, [30].

- The strongest features of post-merger are confined to four typical frequencies, one of which is dominant with respect to the others
- The correlation of these frequencies with NS compactness and tidal deformability yields to quasi-universal relations

Therefore, the detection and characterization of gravitational wave signals from BNS post-merger remnants would bring very important information about NS physics.

3.8 Detection of GW signal from a BNS

On the 17th of August 2017, a gravitational wave signal, GW170817, emitted by a low-mass compact binary was detected [31]. It was the loudest gravitational wave signal yet observed, with a combined signal-to-noise ratio (SNR) of 32.4. At the moment of detection, the interferometer

network included LIGO-Livingston, LIGO-Hanford and Virgo. The detector horizon [37][8], namely the maximum luminosity distance at which the detector could observe a BNS with $SNR \leq 8$, averaging over source position in sky, was 218 Mpc for LIGO-Livingston, 107 Mpc for LIGO-Hanford and 58 Mpc for Virgo.

As shown in Fig. 3.8, the signal was clearly visible in the two LIGO detectors, whereas not in Virgo data due both to the lower BNS horizon and to the direction of the source with respect to the detector's antenna pattern.

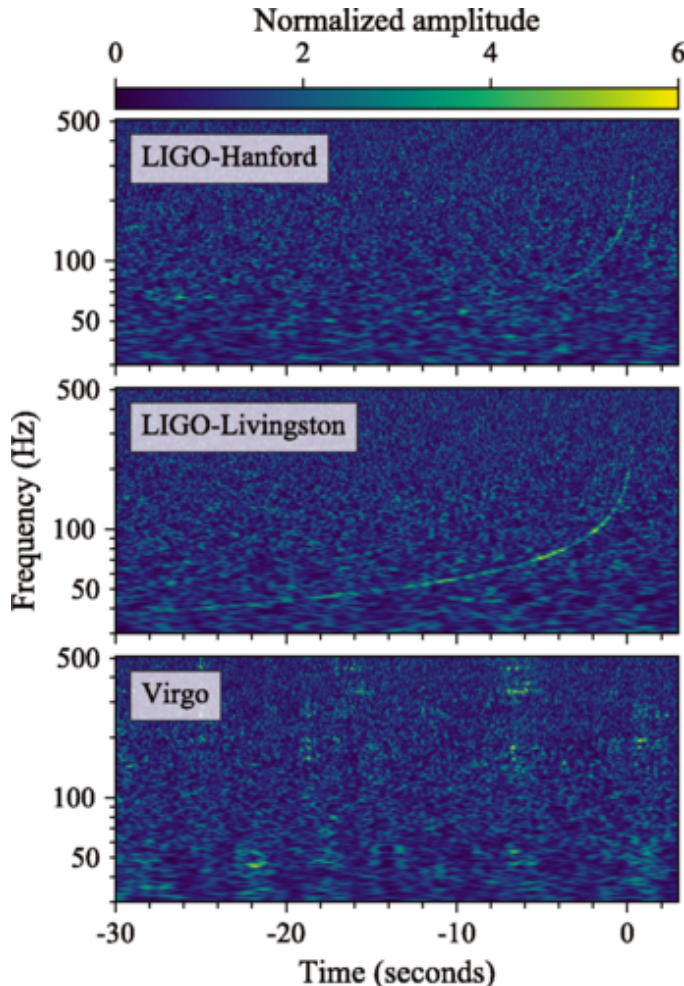


Figure 3.8: Time-frequency representation of data containing the gravitational-wave event GW170817, observed by the LIGO-Hanford (top), LIGO-Livingstone (middle) and Virgo (bottom) detectors. Times are shown relative to August 17, 2017 12:41:04 UTC. The amplitude scale in each detector is normalized to that detector's noise amplitude spectral density. [31]

Although Virgo data, due to the signal weakness, were not used for the estimation of source parameters, they played a fundamental role for a precise sky localization of the source to an area of 28 deg^2 , much better than the 191 deg^2 of LIGO-network [31], that allowed to trigger promptly an electromagnetic follow-up campaign. More precisely, the source was localized to a region of sky 380 Mpc^3 in volume, near the southern constellation Hydra. The luminosity distance of the source was estimated to be $40^{+8}_{-14} \text{ Mpc}$, making it the closest GW source ever observed. As we said see in Section 1.7, the source parameter that can be better estimated from the gravitational signal

emitted by a binary system during the inspiral phase is the chirp mass, in this case constrained to $M_{chirp} = 1.188^{+0.004}_{-0.002} M_\odot$. Anyway, the gravitational waveform emitted by a BNS is influenced also by the *effective spin parameter* [38]

$$\chi_{eff} \equiv \frac{m_1 \chi_1 \cos \theta_1 + m_2 \chi_2 \cos \theta_2}{m_1 + m_2} \quad (3.16)$$

where θ_1, θ_2 are the angles between spin vectors and the orbital momentum vector, χ_1 and χ_2 the dimensionless spin magnitudes of merging objects, defined as

$$\chi_i = \frac{c|\mathbf{S}_i|}{Gm_i^2}, \quad (3.17)$$

Physically, χ_{eff} represents the mass-weighted sum of the spin projections along the axis of orbital angular momentum.

The estimates of mass components m_1 and m_2 and of mass ratio q depend on the assumptions made about the spin. Admitting spin magnitude up to the maximum allowed value, $|\chi| \leq 0.89$, it was obtained $m_1 \in (1.36, 2.26) M_\odot$ and $m_2 \in (0.86, 1.36) M_\odot$. On the other hand, restricting the spin magnitude to $|\chi| \leq 0.05$, consistent with the observed NS population (PSR J0737-3039A has the most extreme spin known up to now, $\chi \lesssim 0.04$ [39]), the component masses were estimated to lie in a range between $m_1 \in (1.36, 1.60) M_\odot$ and $m_2 \in (1.17, 1.36) M_\odot$, with total mass of the system $2.74^{+0.04}_{-0.01} M_\odot$ [31]. The consistency of mass estimates with the dynamically measured masses of known NS in binaries and the multiple subsequent observations in electromagnetic spectrum suggested that the source was a neutron star binary.

Conversely to what happens in the coalescence of black holes, during a BNS inspiral each star's gravitational field induces a tidal deformation on the companion. From a quantitative point of view, it translates into a phase difference with respect to a BBH signal, that, at leading order, is proportional to the tidal parameter

$$\Lambda = \frac{2}{3} k_2 C^{-5} \quad (3.18)$$

with k_2 relativistic Love number at $l = 2$ [41] and $C \equiv Gm/(c^2R)$ compactness.

The *tidal deformability* Λ describes how much a neutron star is deformed in the presence of a tidal field and depends on the matter equation of state. To leading order to Λ_1 and Λ_2 , the gravitational wave phase is determined by the parameter ([31] and references therein)

$$\tilde{\Lambda} = \frac{16}{3} \frac{(m_1 + 12m_2) m_1^4 \Lambda_1 + (m_2 + 12m_1) m_2^4 \Lambda_2}{(m_1 + m_2)^5} \quad (3.19)$$

The first analysis, that allowed the tidal parameters of the two components to vary independently, placed the upper limits $\tilde{\Lambda} \leq 800$ in the low-spin case and $\tilde{\Lambda} \leq 700$ in the high-spin one. The constraints on Λ_1 and Λ_2 disfavored equations of state that predict less compact stars.

A subsequent analysis ([33], [32]) improves the previous estimations by assuming that both bodies were neutron stars, described by the same equation of state (assumption justified by the fact that every neutron star should represent the equilibrium ground-state) and whose spins are consistent with astrophysical observations. This analysis is performed with two different methods: using some relations not dependent on EOS and exploiting a parametrized EOS.

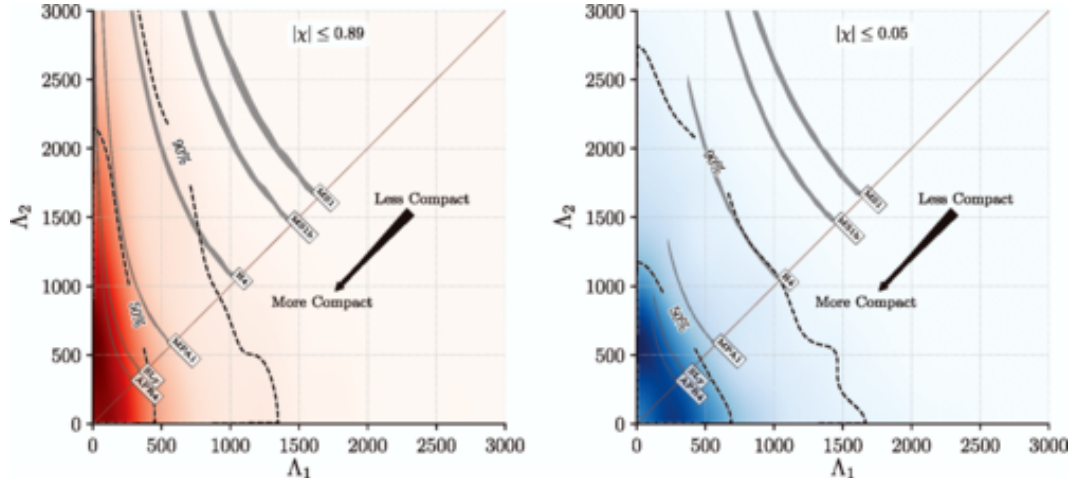


Figure 3.9: Probability density for the tidal deformability parameters of the high and low mass components inferred from the detected signal using the post-Newtonian model. Contours enclosing 90% and 50% of the probability density are overlaid (dashed lines). The diagonal dashed line indicates the $\Lambda_1 = \Lambda_2$ boundary. Constraints are shown for the high-spin scenario $|\chi| \leq 0.89$ (left panel) and for the low-spin $|\chi| \leq 0.05$ (right panel). As a comparison, predictions for tidal deformability given by a set of representative equations of state are plotted (shaded filled regions), all of which support stars of $2.01M_\odot$. EOS that produce less compact stars, such as MS1 and MS1b, predict Λ values outside the 90% contour. [31]

With the first method, radii were estimated as $R_1 = 10.8_{-1.7}^{+2.0}$ km and $R_2 = 10.7_{-1.5}^{+2.1}$ km. Employing the EoS parametrization, instead, it was obtained $R_1 = 11.9_{-1.4}^{+1.4}$ km and $R_2 = 11.9_{-1.4}^{+1.4}$ km. The difference between the two approaches derives from the fact that, while the first result is determined only by GW measurement, the parametrized EOS analysis imposes a further observational constraint, namely that the EOS must support masses up to $1.97M_\odot$, the highest NS mass measured up to now, which is taken as a lower limit for maximum NS mass. This produces a bias towards greater values, because small radii are generally predicted by softer EOSs, which, on the other hand, do not allow high mass values.

The analysis performed to constrain properties of the binary component bodies used the inspiral phase of GW signal. However, as we said in Section 3.7.3, the compact remnant left after the merger could have different fates depending on the mass of inspiraling objects and on equation of state ruling nuclear matter. Hence, the post-merger GW signal could reveal a lot of information. Unfortunately, post-merger signal from HMNS or short-lived SMNS involves higher frequencies, of the order of some kHz, range in which, currently, the detectors are much less sensitive. The same problem arises in the case of a prompt collapse to a black hole, for which the post-merger estimated frequency is about ~ 6 kHz [36]. Only in the case of a long-lived remnant the post-merger involves frequencies less than some kHz.

A search ([36]) for short ($\lesssim 1$ s) and intermediate ($\lesssim 500$ s) signals from the remnant of GW170817 binary NS merger was performed, but with null result. However, the estimation of an upper bound for an hypothetical post-merger GW signal showed that the post-merger signal of a similar event should be detectable when advanced detectors reach the design sensitivity or in next-generation detectors [32][36].

3.8.1 GRB and EM counterparts

On August 17, 2017 the Fermi Gamma-ray Burst Monitor and the Anti-Coincidence Shield for the Spectrometer for INTEGRAL observed, independently from LIGO and Virgo detection, the gamma-ray burst GRB 170817A. The probability of a near simultaneous temporal and spatial observation of GRB 170817A and GW170817 occurring by chance is estimated to be 5.0×10^{-8} , which leads to the conclusion that the two observations were correlated [35].

The GRB detection occurred $1.734 \pm 0.054\text{s}$ after the coalescence time, and subsequent analysis determined the burst duration to be $T_{90} = 2.0 \pm 0.5\text{s}$, where T_{90} defined as the interval over which 90% of the burst fluence is accumulated in the energy range $50 - 300\text{keV}$. From the T_{90} measurement, GRB 170817A was classified as a short GRB.

A major astrophysical consequence of this joint detection is the confirmation that NS binaries are indeed one of the possible sources of short GRBs.

One of the most interesting features of GRB 170817A lies in its energetics. Indeed, the estimated isotropic energy release in gamma rays during GRB 170817A is $E_{iso} = (3.1 \pm 0.7) \times 10^{46}\text{erg}$ and the isotropic peak luminosity $L_{iso} = (1.6 \pm 0.6) \times 10^{47}\text{ergs}^{-1}$, in the standard 1 keV-10 MeV energy band. Notice that, in view of the fact that GRBs are believed to be relativistically beamed, thus with a collimated emission, isotropic energetics are upper bounds on the true total ones.

Compared with the distribution of detected GRBs with measured redshift, GRB 170817A is two orders of magnitude closer but up to six orders of magnitude less energetic. In [35], several explanations for such dimness are proposed and analyzed, among which the most feasible are

- GRBs are produced according to the standard uniform top-hat jets model, but we viewed it from beyond the the half-jet opening angle
- Presence of a more complex geometry that involves a structured jet, which provides a wider range of angles from which the observer could still detect the emission

The observation of a short GRB associated with a BNS merger can be used to derive constraints on the EoS of NS matter. In particular, there exist two possible models of the merger remnant that powered the GRB: it collapsed to a rotating black hole with a surrounding disk that powered the sGRB, or the merger formed a rapidly rotating, strongly magnetized NS with an accretion disk. The fate of a merging BNS is determined mainly by its component masses and equation of state, therefore a comparison between the cited models and masses obtained from GW signal could constrain some equations of state [35].

The joint observation of gravitational wave and a short GRB can also be studied for its implications in fundamental physics, in particular about [35]:

- *Speed of gravity:* knowing the delay time and the approximate distance of the source, one can constrain the fractional speed difference between light and gravitational waves. The conservative limit, obtained from lower bound for distance, is

$$-3 \times 10^{-15} \leq \frac{v_{gw} - v_{em}}{v_{em}} \leq +7 \times 10^{-16} \quad (3.20)$$

- *Test of the Equivalence Principle* by probing whether electromagnetic and gravitational radiation are affected by background gravitational potentials in the same way or not. This test can be performed exploiting the Shapiro effect, according to which the propagation time of massless particles in curved spacetime, thus in the presence of gravitational fields, is slightly increased with respect to the flat spacetime case. In the definition of Shapiro delay one can add a factor γ that parametrizes the deviation from Einstein-Maxwell theory, which minimally couples classical electromagnetism to general relativity (and in which $\gamma_{gw} = \gamma_{em} = 1$). Allowing for different values of γ for propagation of electromagnetic and gravitational waves, it was found

$$-2.6 \times 10^{-7} \leq \gamma_{gw} - \gamma_{em} \leq 1.2 \times 10^{-6} \quad (3.21)$$

In addition, such a joint detection provides important information about the central engine of SGRBs. In particular, two explanations, both compatible with the data, can account for the delay between GW and GRB trigger times. On one side, it can be intrinsic to the central engine, reflecting the time elapsed from the components merger to the formation of a remnant black hole with the resulting jet. This interpretation results particularly fascinating, since it includes the possibility of a long-lived massive NS survived from seconds to minutes after the merger. Alternatively, the delay could arise in the jet propagation, for example in the time it takes for the jet to break out of the dense and gaseous environment produced by non-relativistic ejecta.

Both these scenarios are explored and their consequences evaluated in [35].

Electromagnetic counterparts

The precise source localization obtained thanks to LIGO-Virgo data allowed a systematic search for electromagnetic counterparts of the gravitational wave signal. A few hours, $\sim 11h$, after the coalescence time, an optical counterpart was observed that did not match any known asteroid or supernova. It was located in the NCG4993 galaxy, at a distance $\simeq 40Mpc$ consistent with the source luminosity distance estimated from the gravitational wave signal [34].

In the following weeks, observations were made also in the ultraviolet, optical and infrared. In particular, early ultraviolet observations revealed a blue transient that faded within 48 hours, while optical and infrared observations showed a redward evolution over $\sim 10days$. The evolution of spectral energy distribution, rapid fading and emergence of broad spectral features indicated that the source had physical properties similar to the ones predicted by kilonovae models. The late-time infrared excess associated with GRB170817A was interpreted as the signature of r-process nucleosynthesis[34].

Following early non-detections, X-ray and radio emission were discovered at the transient's position respectively ~ 9 and ~ 16 day after the merger [34]. X-ray observations of GRB afterglows are important to constrain the geometry of the outflow, its energy output, and the orientation of the system with respect to the observer's line of sight.

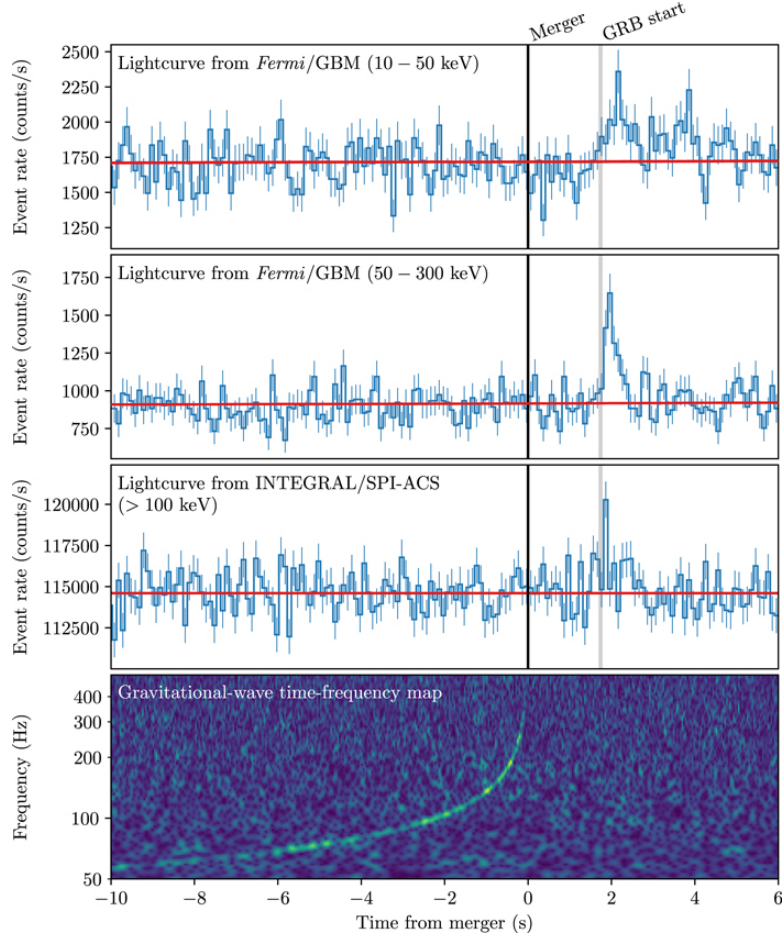


Figure 3.10: Joint detection of GW170817 and GRB 170817A, [35]

On the other hand, no ultra-high-energy gamma-rays nor neutrino candidates consistent with the source were found in follow-up searches.

All these detections are consistent with a BNS merger, that produces electromagnetic signals through two different processes[34][40]. First, during the merger, in dynamical and accretion-disk-wind ejecta some nuclei are synthesized via the rapid neutron-capture process (r-process). After the merger, these heavy nuclei start to decay radioactively, producing the early optical and infrared emission. Later on, the interaction of the merger ejecta with the ambient medium generates a different radio emission.

Chapter 4

Coherent WaveBurst pipeline and simulated signals

The aim is to study the post-merger signal of binary neutron stars coalescence, using simulated waveforms for different equations of state. As we said in Section 3.7.3, the post merger features should be very different for varying models, therefore their analysis constitutes a powerful tool to discriminate NS equation of state. Post-merger is very difficult to detect because of the low sensitivity of current detectors in the high frequencies region it involves. For this reason no measured data are available, therefore I worked with simulated data provided by the Trento-University Numerical Relativity group. In the first part of this chapter I briefly introduce the cWB algorithm used for the analysis. Then I describe the simulation stage of the analysis and the different models considered.

4.1 cWB algorithm

The targets of advanced ground-based interferometers include GW bursts from different possible sources, such as core-collapse supernovae or merging of compact objects binaries. The inner workings of some phenomena among these, like the post-merger phase of BNS coalescence, are difficult to model; moreover some sources of gravitational wave bursts are still uncertain, therefore the search for GW transients requires an algorithm as general as possible, with minimal assumptions on the source characteristics. As said in Section 2.7, dealing with a network of detectors the analysis algorithm can require coincidence and coherence of the signal. cWB employs a coherent approach, which leads to many advantages:

- sensitivity is not limited by least sensitive detector
- some coherent statistics can be built in order to discriminate real GW signals from environmental or instrumental noise (for example, non-gaussian detector noise can mimic a GW signal)

The data from different detectors, combined in a coherent way, are then analyzed in the framework of constraint maximum likelihood method [56], that we briefly describe below.

4.1.1 Likelihood method

We start considering a single detector with data $x[i]$. There are two mutually exclusive hypothesis: the absence H_0 or the presence H_1 of a gravitational wave signal in the data stream, both of them described by a joint probability density $p(x|H_0)$ and $p(x|H_1)$ respectively. Any decision rule would imply two possible errors: false alarm, selection of H_1 when H_0 is true, and false dismissal, selection of H_0 when H_1 is true. In order to set a decision rule, the Neyman-Pearson criterion has been chosen [56], which states that the best decision rule ensures the lowest false dismissal probability for fixed false alarm probability. According to this criterion, the rule accepts H_1 when the *likelihood ratio* $\Lambda(x)$, defined as [56]

$$\Lambda(x) = \frac{p(x|H_1)}{p(x|H_0)}, \quad (4.1)$$

is greater than a threshold fixed by the specified false alarm probability and the opposite for H_0 .

Assuming for the detector a Gaussian white noise with zero mean, characterized by a standard deviation σ , the probability densities associated to the hypothesis H_0 and H_1 become

$$p(x|H_0) = \prod_{i=1}^N \frac{1}{\sqrt{2\pi}\sigma^2} \exp\left(-\frac{x^2[i]}{2\sigma^2}\right) \quad (4.2)$$

$$p(x|H_1) = \prod_{i=1}^N \frac{1}{\sqrt{2\pi}\sigma^2} \exp\left(-\frac{(x[i] - \xi[i])^2}{2\sigma^2}\right) \quad (4.3)$$

where $\xi = F_+ h_+ + F_\times h_\times$ is the detector response to a gravitational-wave signal (h_+, h_\times) .

Thus, the likelihood ratio can be expressed as

$$L = \ln(\Lambda(x)) = \sum_{i=1}^N \frac{1}{\sigma^2} \left(x[i] \xi[i] - \frac{1}{2} \xi^2[i] \right). \quad (4.4)$$

Extending this formalism to a network of K detectors, supposing uncorrelated noise from different detectors, the likelihood yields [56]

$$\mathcal{L} = \sum_{k=1}^K \sum_{i=1}^N \frac{1}{\sigma^2} \left(x[i] \xi[i] - \frac{1}{2} \xi^2[i] \right). \quad (4.5)$$

By maximizing the functional \mathcal{L} , the GW waveforms h_+ and h_\times can be estimated [54] and the source parameters reconstructed [55], as we will explain later for the case of cWB pipeline.

4.1.2 Coherent waveBurst

The cWB algorithm, based on c++/ROOT and developed by the LIGO Scientific Collaboration (LSC), can work without making any a priori assumption on the signal morphology or on the source, which is the case of this thesis, or with weak assumptions on the signal model. In the following sections we describe the main steps of cWB pipeline:

- Wavelet transformation and data conditioning
- Multi-resolution analysis and selection of pixels clusters in time-frequency map
- Likelihood maximization and selection of coherent triggers

WDM transform and data conditioning

Detectors data time series are analyzed in the time-frequency (TF) domain, since a GW transient signal can be identified as a pattern on TF plane thanks to its excess power above detector stationary noise. The time-frequency representation is obtained via a Discrete Wavelet Transform, namely projecting data on a local orthonormal basis of wavelet functions [60]. A set of complementary wavelets allows to decompose data without gaps or overlaps, so that also the inverse transform is well defined. Moreover, with this approach data are critically sampled, the energy is conserved and the statistical independence of TF data ensures a straight-forward application of reconstruction algorithms [53]. Wavelet series give a time-scale representation of data where each wavelet scale can be associated with a certain frequency band of the initial time series, therefore wavelet time-scale spectra can be displayed as TF scalogram, where the scale is replaced by the central frequency of the band. In particular, cWB employs the Wilson-Daubechies-Meyer (WDM) transform, which acts as a kind of band-pass filter like wavelets, but offers a more accurate separation of spectral components, and creates TF maps with fixed pixels dimensions (for more details on WDM transform see [53]).

In order to remove predictable noise components from the data, Linear Prediction Error (LPE) filters are applied. Usually, these filters are applied in time domain: in order to use them on data decomposed in discrete wavelets, LPE filters are constructed and applied separately to each wavelet frequency layer.

Finally, data whitening is accomplished: assuming quasi-stationary and Gaussian noise, its WDM power spectral density can be estimated. cWB considers the TF map with finest frequency resolution and, for each layer, computes several values of the noise RMS by using a running average. Then the TF data samples are normalized by the noise RMS and the whitened (or noise-scaled) data are given by [55]

$$w_k[i, j] = \frac{x_k[i, j]}{\sqrt{\sigma_k^2[i, j]}}. \quad (4.6)$$

Pixels selection

cWB pipeline performs wavelet decomposition at different resolution levels (Multi-Resolution Analysis) and, for each WDM resolution, the excess power pixels (also called *black* or *hot pixels*) are selected for the subsequent analysis. Hot pixels are chosen according to a threshold defined by the *black pixels probability* (bpp) whose value is approximately the fraction of pixels selected by the algorithm for each TF resolution. In cWB, events are defined as groups of pixels, namely clusters, in TF data. Different clusters are combined into a single event according to the *Tgap* and *Fgap* threshold, that will be explained more in detail later.

Likelihood maximization and selection of coherent triggers

In general, the likelihood functional is calculated as a sum over the selected data samples (Eq. 4.5). Data from a network of K detectors form a discrete series $x_k[i, j]$, with k detector index in the network and i, j time-frequency pixel index.

To simplify notation, we can consider a K-dimensional space where each dimension represents a detector. In this space we define the vectors

$$\begin{aligned} F_+ &= \{F_{1+}, F_{2+}, \dots, F_{K+}\} \\ F_\times &= \{F_{1\times}, F_{2\times}, \dots, F_{K\times}\} \\ x[i, j] &= \{x_1[i, j], x_2[i, j], \dots, x_K[i, j]\} \\ A &= \{A_1, A_2, \dots, A_K\} \end{aligned}$$

where F is the detector antenna pattern introduced in Section 2.6 and A the *complex antenna pattern*, defined as

$$A = \frac{1}{2} (F_+ + iF_x) \quad (4.7)$$

$$\tilde{A} = \frac{1}{2} (F_+ - iF_x). \quad (4.8)$$

We can introduce also the normalized vectors

$$\begin{aligned} f_+[i, j] &= \left\{ \frac{F_{1+}}{\sigma_1[i, j]}, \frac{F_{2+}}{\sigma_2[i, j]}, \dots, \frac{F_{K+}}{\sigma_K[i, j]} \right\} \\ f_\times[i, j] &= \left\{ \frac{F_{1\times}}{\sigma_1[i, j]}, \frac{F_{2\times}}{\sigma_2[i, j]}, \dots, \frac{F_{K\times}}{\sigma_K[i, j]} \right\} \\ w[i, j] &= \left\{ \frac{x_1[i, j]}{\sigma_1[i, j]}, \frac{x_2[i, j]}{\sigma_2[i, j]}, \dots, \frac{x_K[i, j]}{\sigma_K[i, j]} \right\}. \end{aligned}$$

and define a specific coordinate frame, called the **Dominant Polarization Frame (DPF)**, characterized by $(f_+ \cdot f_\times) = 0$ and $|f_\times| \leq |f_+|$, [56].

In the DPF the likelihood functional can be written as $\mathcal{L} = \mathcal{L}_+ + \mathcal{L}_\times$, where [54]

$$\mathcal{L}_+ = \sum_{i,j=1}^N \left[(\mathbf{w} \cdot \mathbf{f}_+) h_+ - \frac{1}{2} |\mathbf{f}_+|^2 h_+^2 \right] \quad (4.9)$$

$$\mathcal{L}_\times = \sum_{i,j=1}^N \left[(\mathbf{w} \cdot \mathbf{f}_\times) h_\times - \frac{1}{2} |\mathbf{f}_\times|^2 h_\times^2 \right]. \quad (4.10)$$

The equations for the GW waveform are obtained by variation of the likelihood functional, which results in the equations

$$(\mathbf{w} \cdot \mathbf{f}_+) = |\mathbf{f}_+|^2 h_+ \quad (4.11)$$

$$(\mathbf{w} \cdot \mathbf{f}_\times) = |\mathbf{f}_\times|^2 h_\times \quad (4.12)$$

or, in matricial form,

$$\begin{bmatrix} (\mathbf{w}[i] \cdot \mathbf{e}_+[i]) \\ (\mathbf{w}[i] \cdot \mathbf{e}_\times[i]) \end{bmatrix} = \begin{bmatrix} |\mathbf{f}_+[i]| & 0 \\ 0 & |\mathbf{f}_\times[i]| \end{bmatrix} \begin{bmatrix} h_+[i] \\ h_\times[i] \end{bmatrix} \quad (4.13)$$

The norms $|\mathbf{f}_+|^2$ and $|\mathbf{f}_\times|^2$ characterize the network sensitivity to the h_+ and h_\times polarizations. Substituting the solutions to these equations into the functional $\mathcal{L}[\mathbf{h}]$ and maximizing over source coordinates (θ, ϕ) , the *maximum likelihood statistics* can be found [54]:

$$L_m(i, j)_{\theta, \phi} = \max_{\theta, \phi} \{L_p(i, j, \theta, \phi)\}, \quad (4.14)$$

which represents the maximum possible energy detected by the network at a given TF location (i, j) .

Calculated as a function of time and frequency, it gives a likelihood time-frequency map (an example is shown in Fig.4.1) [54]. A single data sample in this map is called LTF pixel and is characterized by its time-frequency coordinates (i, j) and by the wavelet amplitudes $w_k(i, j, \theta, \phi)$.

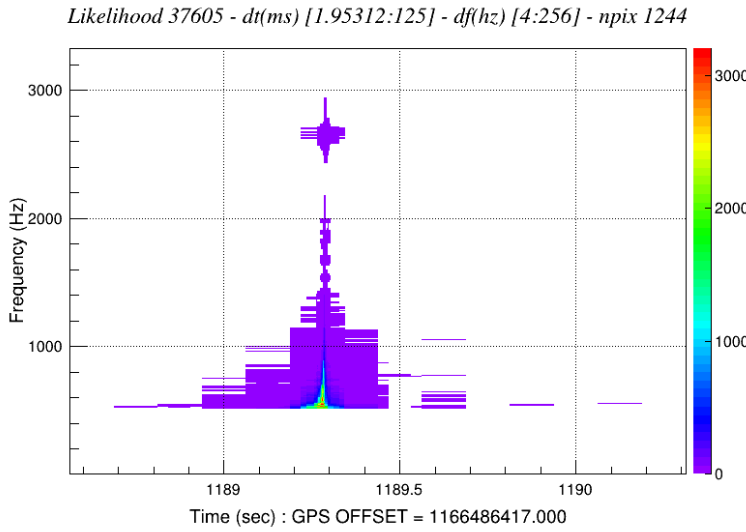


Figure 4.1: Example of likelihood time-frequency map for an event.

The maximum likelihood 4.14 can be written [55] as a quadratic form

$$L_{max} = \sum_{i \in C} \mathbf{w}[i] P[i] \mathbf{w}^T[i] \quad (4.15)$$

where the matrix $P[i]$ is the projector constructed from the components of the unit vectors $\mathbf{e}_+ \frac{\mathbf{f}_+}{|\mathbf{f}_+|}$ and $\mathbf{e}_x = \frac{\mathbf{f}_x}{|\mathbf{f}_x|}$:

$$P_{nm}[i] = e_{n+}[i]e_{m+}[i] + e_{n\times}[i]e_{m\times}[i]. \quad (4.16)$$

The null space of P corresponds to the residual detector noise, the "null stream" E_n , obtained subtracting the reconstructed signal energy from the total energy of the signal.

Eq.4.15 can be split into two parts, the incoherent E_i and coherent E_c energy [57]:

$$E_i = \sum_{i \in C} \sum_n w_n[i] P_{nm}[i] w_n[i] \quad (4.17)$$

$$E_c = \sum_{i \in C} \sum_{n \neq m} w_n[i] P_{nm}[i] w_m[i] \quad (4.18)$$

E_n , E_c and E_i are widely used to construct events selection cuts, as the network correlation coefficient c_c and the burst detection statistic η_c , [55]. The network correlation coefficient

$$c_c = \frac{E_c}{|E_c| + E_n} \quad (4.19)$$

constitutes a powerful consistency test to discriminate genuine GW events, when the signals are coherent and $E_c \gg E_n$ giving $c_c \sim 1$, from spurious events, $c_c \ll 1$, produced by the detectors.

Instead, the burst detection statistics, defined as

$$\eta_c = \left(\frac{c_c E_c K}{K - 1} \right)^{1/2}, \quad (4.20)$$

provides an estimator of the coherent signal-to-noise ratio for correlated GW signals recorded by different detectors. Coherent triggers, where "coherent" refers to the fact that, with this procedure, the trigger is defined for the entire network and not only for the single detector, are selected according to this ranking statistics [51].

Once the coherent triggers have been identified, the next step is the reconstruction of GW burst parameters, like the two GW polarizations, source coordinates and individual detector responses [55].

Regulators

Depending on the configuration, detector noise and source sky location, the detector network sensitivity can be really different for the two GW components: $|\mathbf{f}_\times| \ll |\mathbf{f}_+|$. In this case, most of the SNR would be carried by the \mathbf{f}_+ component, and the \mathbf{f}_\times network response is very unlikely to be reconstructed. The *alignment factor* [55]

$$\alpha = \frac{|\mathbf{f}_\times|}{|\mathbf{f}_+|} \quad (4.21)$$

tells how well the \times polarization of the wave is detected by the network. For perfectly co-aligned detectors $\alpha = 0$, as they can detect only one GW polarization component. The LIGO network, with only Livingston and Hanford detectors, has $\alpha \ll 1$ for a significant portion of the sky. To improve polarization coverage, more detectors with optimally oriented arms [55] should be added to the network, see Fig.4.2. A full polarization coverage is reached for $\alpha \sim 1$ and improves also the reconstruction of source parameters and sky coordinates.

For this reason some network constrains are introduced [56], with the aim to eliminate unlikely solutions for the likelihood functional and reduce the false alarm rate due to instrumental and environmental artifacts in the data [55]. cWB pipeline implements two main regulators: γ regulator, controlled by the γ parameter, makes a prediction of the reconstructed response; δ regulator, controlled by δ parameter, enhances the constraint for 2-detectors subnetworks, when other detectors are not present or act simply as spectators, for example the Livingston-Hanford subnetwork in the Livingston-Hanford-Virgo network when the event is produced at low Virgo sensitivity (more details can be found on [51]).

4.2 Waveform models

The equation of state of matter at high densities as the ones in neutron stars cannot be studied in laboratory. This lack of data represents one of the main obstacles in testing the possible models, although in the last years nuclear matter studies, especially for what concerns nuclear symmetry

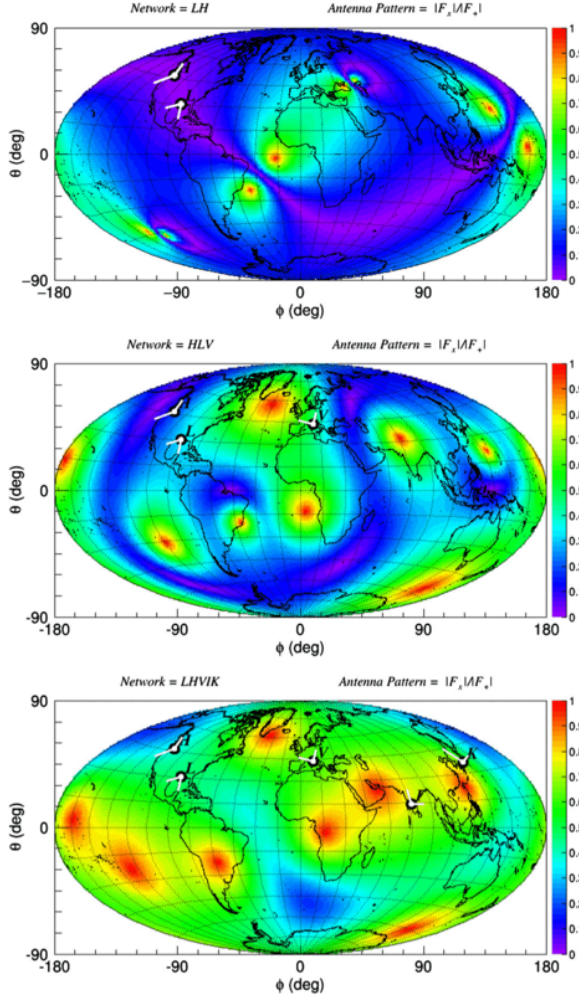


Figure 4.2: Distribution of *network alignment* α over the sky for Livingston-Hanford network (top), Livingston-Hanford-Virgo (middle) and Livingston-Hanford-Virgo-Kagra-LIGOIndia (bottom). Figure from [55].

energy, gave a more practical insight into the problem (see [42]). The main differences in NS equations of state arise from the matter composition and nucleon-nucleon interaction potential taken into account. Here we considered the following models:

- SHT (Shen, Horowitz, Teig [43]): based on a relativistic mean field model with density dependent coupling. For uniform matter, calculations were performed on a wide range of temperatures, densities and proton fractions, and matched to non-uniform matter as the density decreases, while outer layers with lower density are taken into account thanks to a virial expansion for a non-ideal gas of nucleons and nuclei.
- LS220 (Lattimer Swesty, [44]): compressible liquid drop model with a Skyrme force, it includes the effects of interactions and degeneracy of nucleons outside nuclei, together with nuclear deformations and possible phase transitions to uniform nuclear matter at subnuclear densities. It contains an adjustable nuclear force that allows for the input of various parameters, such as bulk and surface symmetry energies, bulk incompressibility and symmetric matter surface tension. In particular, the waveform I used was calculated from a variant

with incompressibility modulus $K = 220$ MeV, hence the name LS220.

- APR4 (Akmal-Pandharipande-Ravenhall, [45]): this model adds three-nucleons corrections to the Argonne v18 two-nucleon interaction. The Hamiltonian obtained in this way predicts a transition in neutron star matter to a phase with neutral pion condensation at baryon density $n_b \sim 0.2 fm^{-3}$, and the presence of a layer, thick tens of meters, in which density changes rapidly from that of the normal phase to the condensed one. More massive neutron stars described by this EoS could also present a quark matter core. APR4 model describes cold neutron stars, but the data in the simulation used here were calculated with a piecewise polytropic approximation of it, plus an hybrid part in order to take into account thermal effects during the evolution.
- H4([46]): obtained within a relativistic mean field approach, it includes hyperons, above all Λ hyperon.

For each model, the evolution of the binary is influenced also by the total mass, the mass ratio q and the spin of the neutron stars. The models chosen for the analysis with their main features are reported in table 4.1, with names constructed as follows: EoS-NSmass-spin. Most configurations are taken as equal mass binaries, apart from the one described by APR4, which actually is denoted by UM. Most of the models chosen are predicted to have a remnant that survives for a certain time (indicated in the table as τ_{MNS}) as a HMNS or a SMNS before collapsing to a black hole, a part from one model that is expected to collapse promptly to a black hole, whose τ_{MNS} is thus indicated as "prompt". For more details on the simulation stages refer to the articles reported in the last column.

Model	M_b	M_∞	τ_{MNS} [ms]	f_{peak} [kHz]	M_{BH}	ref
SHT-M2.0-S	4.01	1.80	>9.4	2.66	...	[47]
SHT-M2.2-I	4.39	1.95	prompt	...	3.73	[47]
LS220-M1.5-S	3.12	1.41	7.7	3.17	2.67	[47]
H4-M1.5	3.04	1.40	12	2.67	2.47	[48]
APR4-UM	3.01	1.42, 1.29	SMNS	3.30	...	[49]

Table 4.1: Main NS binary parameters for the chosen models. M_b is the total baryonic mass of the system, M_∞ the gravitational mass of each star at infinite separation, τ_{MNS} the SMNS or HMNS lifetime, say the time interval before it collapses to a black hole, whose mass is reported as M_{BH} . Where the lifetime reports the indication "prompt", it means that the remnant does not form a HMNS or SMNS but collapses promptly to a black hole. Masses are given in solar mass units M_\odot .

4.3 cWB injections

Analysis on simulated data is performed by injecting many times, with a dedicated cWB tool, the Numerical-Relativity waveforms on simulated detector data, in order to test signal reconstruction

capability and study the reconstructed events. For the analysis described here, we performed one injection every 200s, on time segments of maximum length 1200s. We considered eleven different values of source distance: [56.56, 40, 28.28, 20, 14.14, 9.9, 7, 5, 3.53, 2.5, 1.77, 0.88] Mpc. For each of them, injected distance was selected in a continuous interval of possible values within $\pm 5\%$ from the central one. Fig. 4.3 shows the injected source distance distribution and the injected SNR distribution as a function of source distance. Moreover, waveforms are injected uniformly across the sky: distribution of the injected latitude ϕ and longitude $\cos\theta$ are shown in figures 4.4 and 4.5. Here ϕ and θ are expressed in *cWB coordinate system*, namely with $\theta = [0 : 180]$ degrees, where $\theta = 0^\circ$ represents the North Pole and $\theta = 180^\circ$ the South Pole, and $\phi = [0 : 360]$ degrees, with $\phi = 0^\circ$ at the Greenwich meridian and ϕ increasing in east direction.

As we said in Section 2.6, the detector response depends on the wave polarization, namely on the components h_+ and h_\times , which in turn are determined by ι , the inclination angle of the orbit plane with respect to the line of sight. In order to account for all possible orientations of the source, also ι was selected randomly for each distance.

The simulated noise employed for the analysis follows the PSD curve designed for observation run O4 (Fig.4.6); for each frequency, noise is assumed to follow a gaussian distribution with unitary sigma.

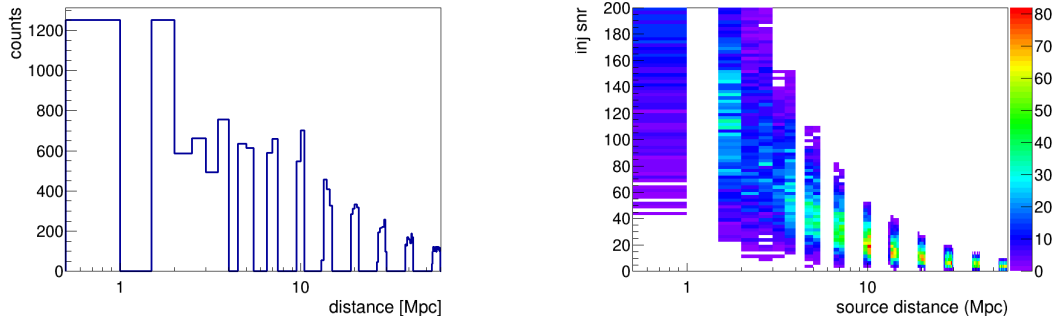


Figure 4.3: Distance distribution (*left*) and injected SNR as a function of injected distance (*right*).

Data were simulated on a three-detectors network, including LIGO-Livingston, LIGO-Hanford and Virgo. Since we want to study the post-merger signal, the search was performed in the frequency

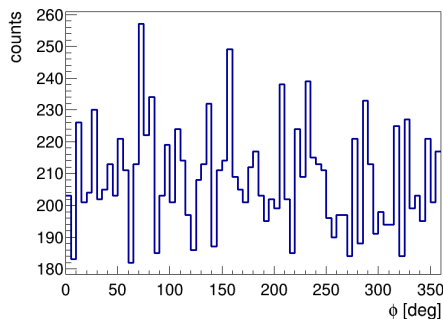


Figure 4.4: ϕ angle distribution.

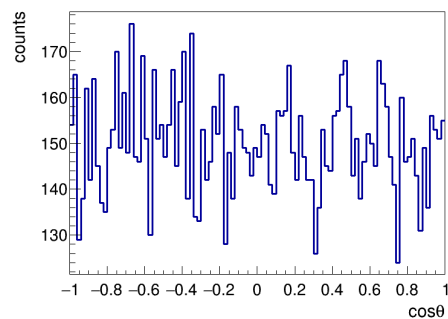


Figure 4.5: $\cos\theta$ distribution

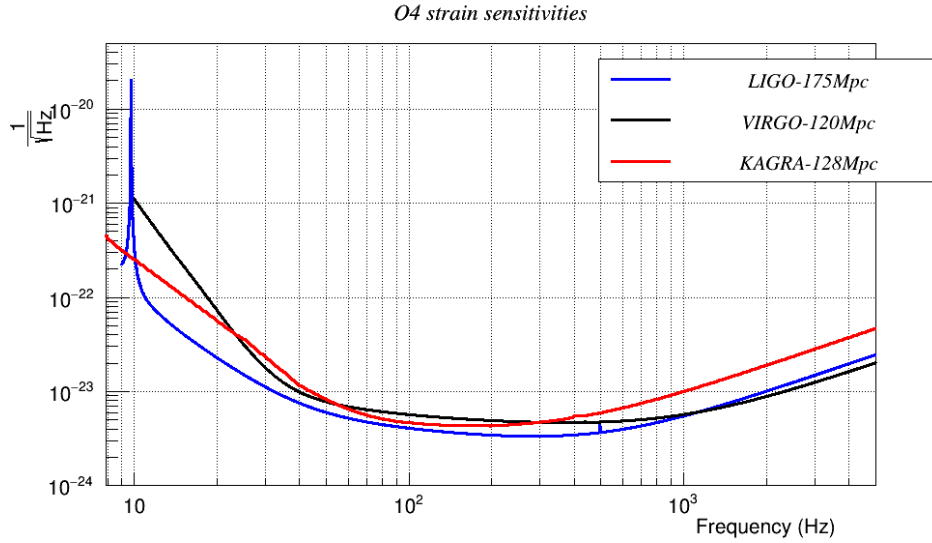


Figure 4.6: Strain sensitivity predicted for O4 for the advanced LIGO, advanced Virgo and KAGRA detectors. [52]

band $[512 - 4096] \text{Hz}$ with seven different time-frequency resolutions (see Table 4.2). This restricted frequency band implies that the reconstructed SNR computed by cWB is forced to be lower than the SNR computed with optimal matched filtering methods, as e.g PyCBC, that instead takes into account also the entire inspiral phase [64][65] and generally indicated as the event SNR.

Rate [Hz]	Layers	df [Hz]	dt[ms]
8	1024	4	125
16	512	8	62.5
32	256	16	31.25
64	128	32	15.625
128	64	64	7.8125
256	32	128	3.90625
512	16	256	1.95312
1024	8	512	0.97652

Table 4.2: Table reporting the time and frequency features of each level. *Layers* is the number of frequency layers in the WDM transform, and *Rate* is given by $dt = 1/\text{Rate}$. The pixel area is fixed by $df \cdot dt = 1/2$.

As we discussed in Section 2.7, the presence of a third detector allows to gain sensitivity also for the cross polarization component of a gravitational wave signal. While the Livingston and Hanford detectors, due to their orientation, could detect only the plus polarization component of an incoming gravitational wave, the position of Virgo allows to detect signal also along the cross one. For this reason the regulators are set as for the three-detectors case.

With regard to the cluster thresholds [51], the chosen values are reported in Table 4.3:

- bpp = Black Pixel Probability: fraction of most energetic pixels selected from TF map to construct events
- $netRHO$ = threshold on ρ , in production stage a cluster is selected if $\rho > netRHO$
- $Tgap$ = allowed time gap between clusters, expressed in seconds
- $Fgap$ = allowed frequency gap between clusters, expressed in Hz
- $TFgap$ = threshold on time-frequency separation between two pixels. Together with $Tgap$ and $Fgap$ constitutes the thresholds applied to decide whether two clusters, separately reconstructed, are part of the same event or not.

Setting parameters	
bpp	0.001
netRHO	4.0
Tgap	0.5
Fgap	1024.0
TFgap	64.0

Table 4.3: Configuration setup of the main analysis parameters chosen.

Since the events we want to study are expected to include post-merger, the values of $Tgap$ and, above all, $Fgap$ are taken much higher than usual, because post-merger involves frequencies $\sim 1kHz$ higher than the merger ones. Such high values are necessary in order to avoid fragmentation of events, namely an event reconstructed as multiple ones. However, some fragmentation still occurs, therefore if one injection is reconstructed in two or more separated events at almost the same time, only the one with higher SNR is kept. Obviously, this procedure implies that for fragmented events we lose a part of the signal, that usually is the post-merger one. For that reason I accomplished a study on events multiplicity, i.e. in how many parts a single event is reconstructed, for the purpose to see how many post-merger events are lost in this way. Results (Fig.4.7) pointed out that with the selected parameters the percentage of events reconstructed in two or more pieces, and hence the percentage of lost events, is order of few percents, thus acceptable for the kind of analysis we want to carry out.

4.4 Theoretical parameters

Figures from 4.8 to 4.12 show data time series and the respective power spectral density for each model, more precisely for the signal in cross polarization h_x (the injected signals in cross and plus polarization are equal). Injections involve last few cycles of the inspiral, merger and post-merger phase, and are performed for a source at a distance of 10 kpc.

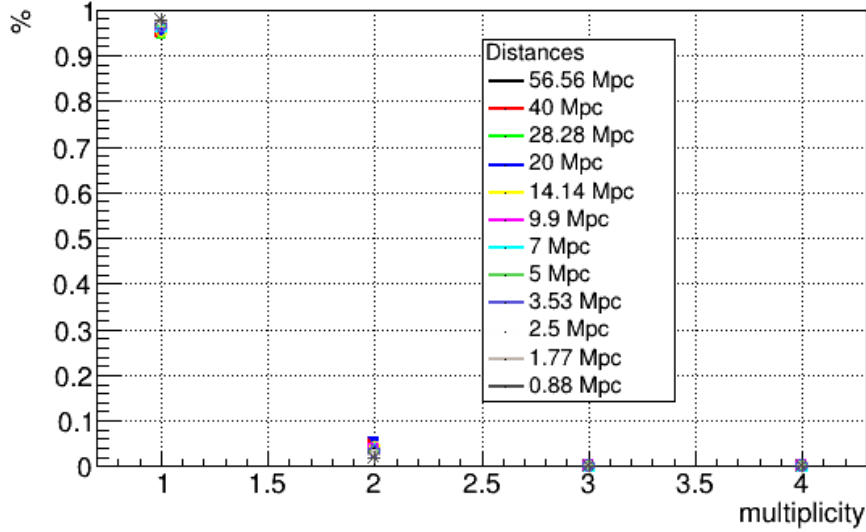


Figure 4.7: Multiplicity of reconstructed events for SHT model. Each color represents a different source distance: this plot shows that multiplicity does not depend on distance in general and that only few percents of the events are fragmented during reconstruction.

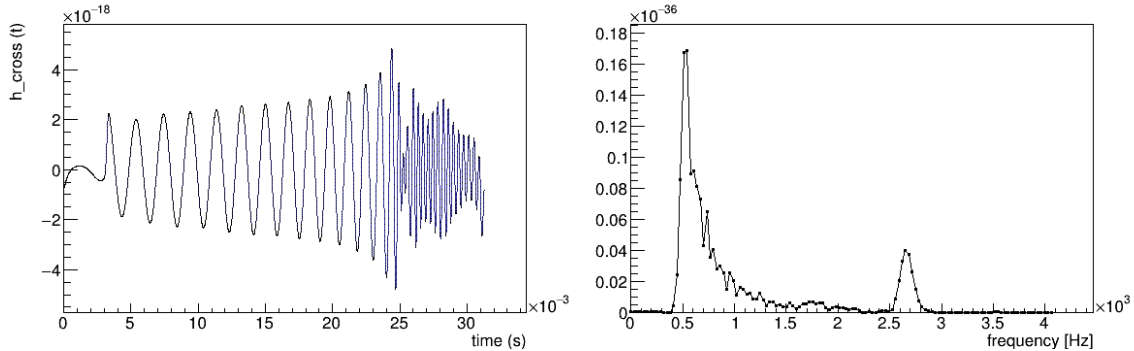


Figure 4.8: Data time series and power spectral density for SHT-M2.0-S model.

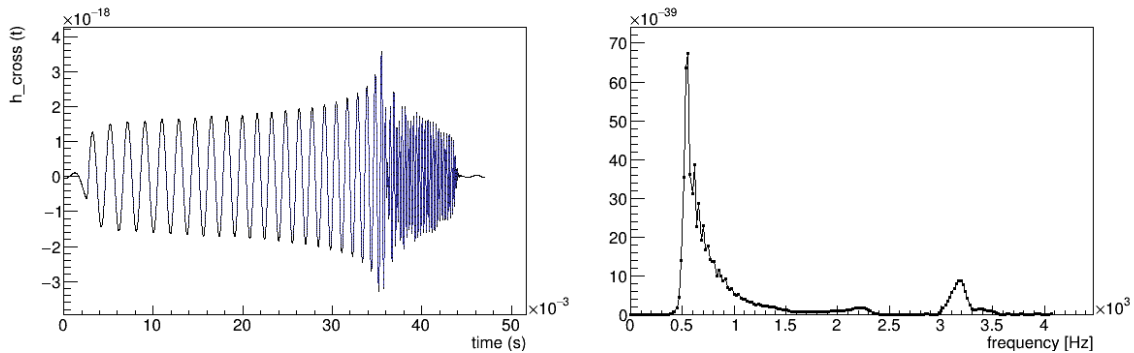


Figure 4.9: Data time series and power spectral density for LS220 model.

While the limit on the right is due to the cut in frequency I set, the second peak corresponds to the post-merger phase and therefore is a crucial parameter to characterize it. For each model,

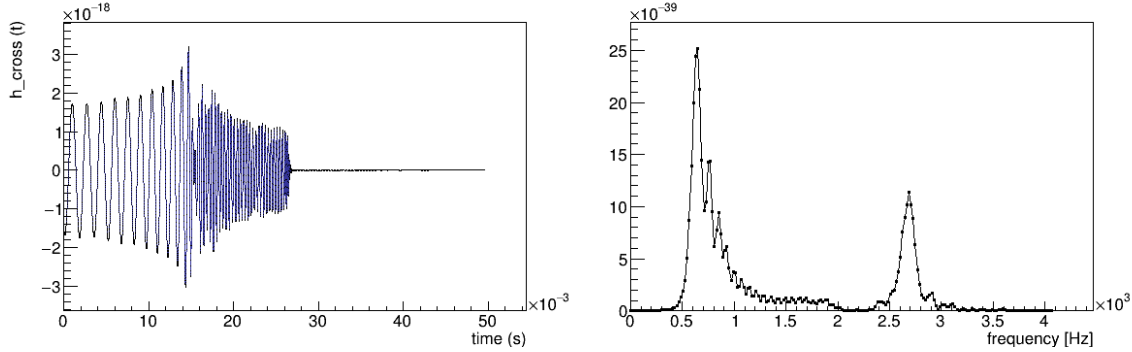


Figure 4.10: Data time series and power spectral density for H4 model.

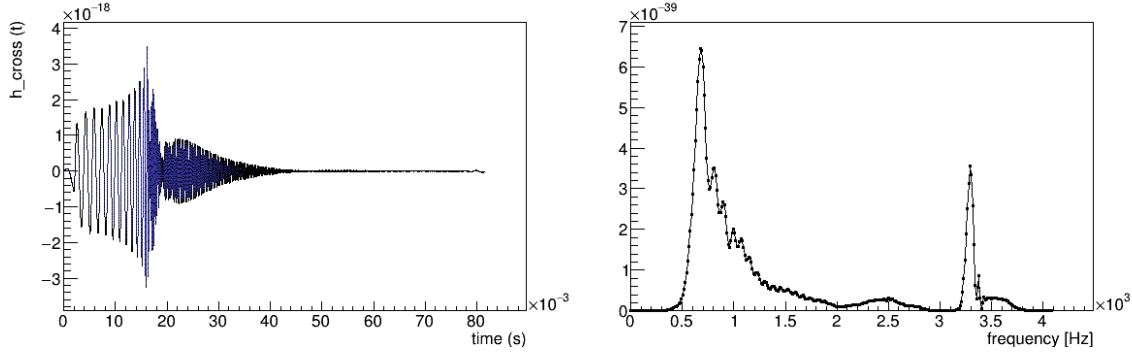


Figure 4.11: Data time series and power spectral density for APR4 model.

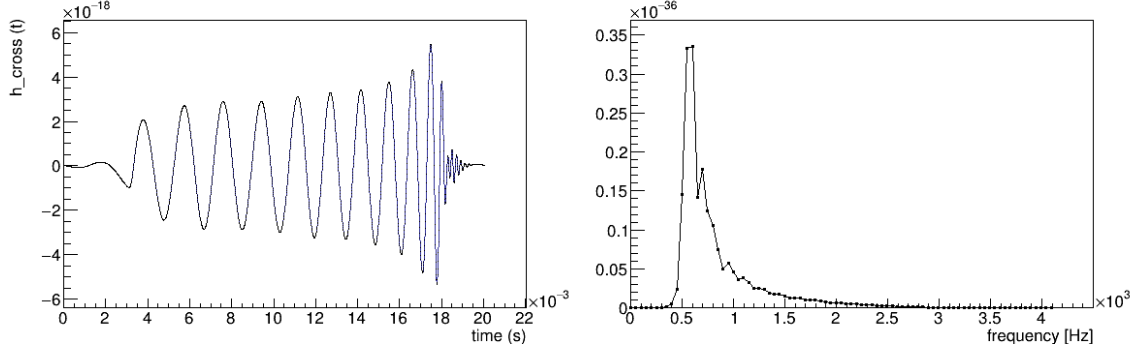


Figure 4.12: Data time series and power spectral density for SHT-M2.2-I model.

its estimated value is reported in table 4.4, together with

$$\tilde{h}_{\text{rss}}(f)_{,\text{ratio}} = \frac{\sum_{f>1280\text{Hz}} (\tilde{h}_x(f)^2 + \tilde{h}_+(f)^2) df}{\sum_f (\tilde{h}_x(f)^2 + \tilde{h}_+(f)^2) df}, \quad (4.22)$$

namely the ratio between $\tilde{h}_{\text{rss}}(f)$ computed for frequencies above $f = 1280\text{Hz}$ and the one calculated over the whole spectrum (in this range of frequency).

In general, for a sampled signal $h(t_i)$, the *root-square-sum amplitude* h_{rss} of detector responses is defined as [57]

$$h_{\text{rss}} = \sqrt{\sum_i \frac{(h_+^2(t_i) + h_x^2(t_i))}{f_s}} \quad (4.23)$$

with f_s sampling rate.

The limit value $f = 1280\text{Hz}$ has been chosen because it is the edge of a layer (feature that will be used for the analysis described in following chapter) and every model predicts frequencies of post-merger signals above this value. The SHT-M2.2-I does not present a high frequency peak, consistent with the fact that it is expected to collapse promptly to a black hole.

Model	f_{pm} [Hz]	$\tilde{h}_{rss}(f)$ ratio
SHT-M2.0-S	2650	0.21
LS220-M1.5-S	3200	0.21(5)
H4-M1.5	2700	0.34
APR4-UM	3300	0.31
SHT-M2.2-I	not present	0.13

Table 4.4: Estimate of the post-merger peak in PSD, f_{pm} , and $\tilde{h}_{rss}(f)$ ratio for each model considered.

Table 4.4 makes it clear that the listed parameters vary between the different models, therefore represent an important estimator to distinguish them.

Chapter 5

Characterization of post-merger signal

In previous section we saw how the coherent WaveBurst algorithm works and how we simulate gravitational wave signals from binary neutron stars mergers, describing the different models and configurations taken into account. In this chapter we present the results obtained for what concerns the characterization of post-merger signals reconstructed from simulations. In particular, we are interested in a characterization of the main time-frequency features of reconstructed signals.

5.1 Waveform examples

For each model considered and previously described, figure 5.1 to 5.5 show the time-frequency map and time series of an example of reconstructed event. The pipeline recalculates the TF map, at a fixed resolution, starting from the signal reconstructed in time for each detector. This TF map covers 99.9% of the reconstructed signal.

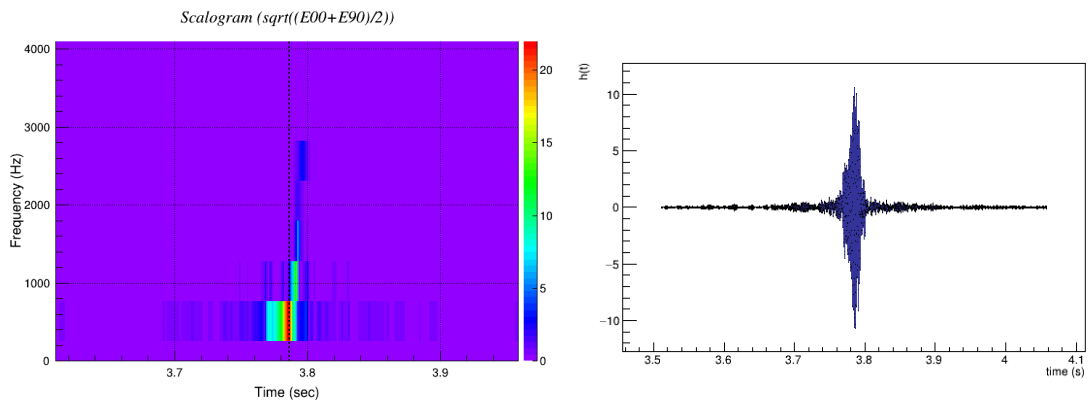


Figure 5.1: Example of time frequency map (left) and reconstructed waveform (right) for SHT-M2.0-S model.

The results for a single detector shown in this chapter concern the Livingston detector, but the same analysis is carried out also on data from Hanford and Virgo.

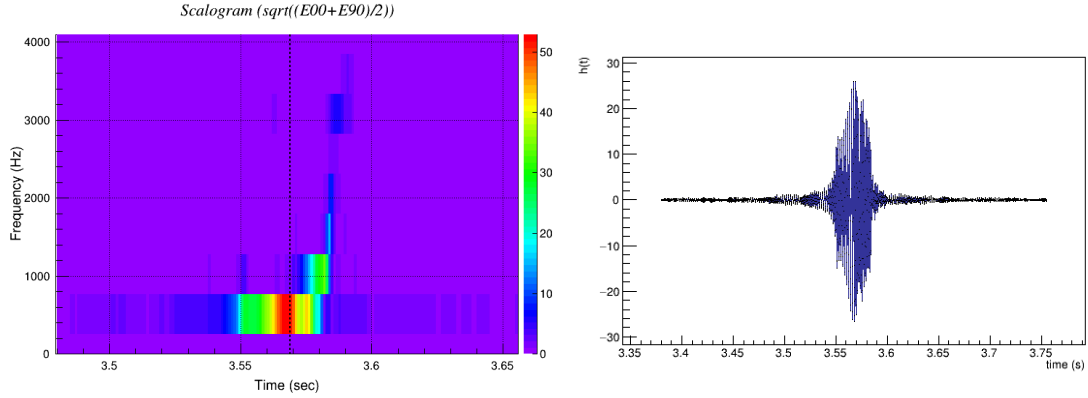


Figure 5.2: Example of time frequency map (left) and reconstructed waveform (right) for LS220 model.

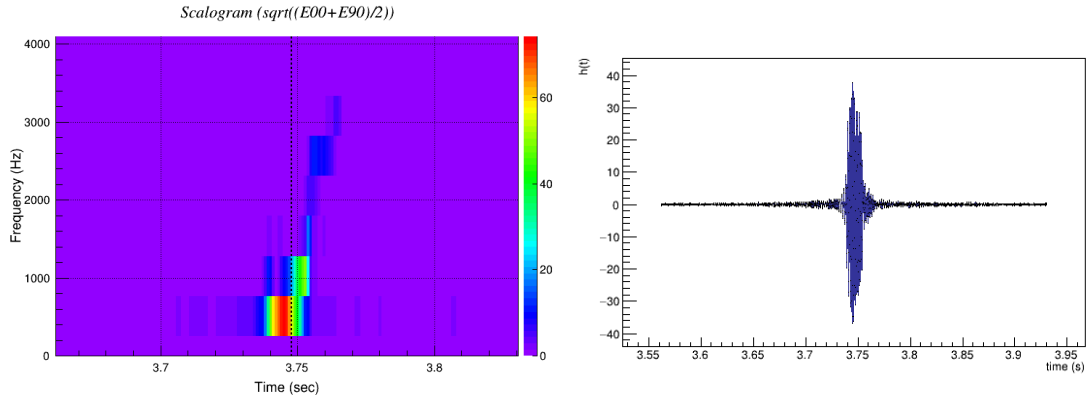


Figure 5.3: Example of time frequency map (left) and reconstructed waveform (right) for H4 model.

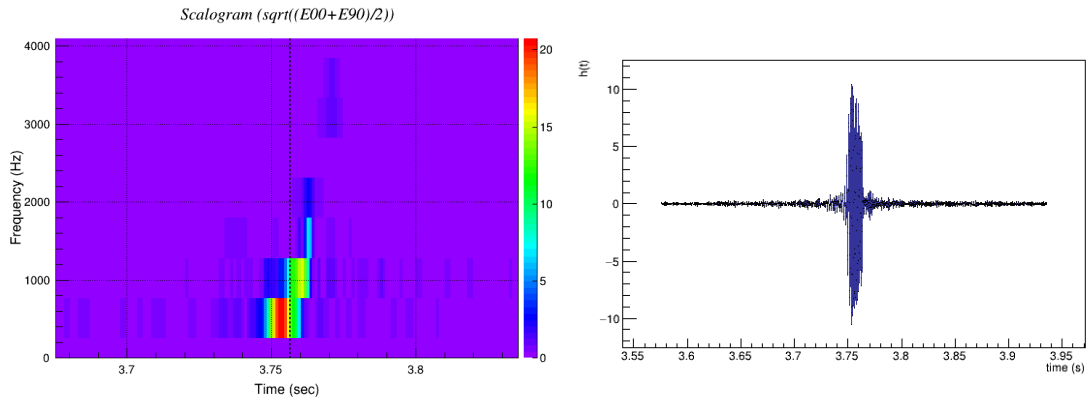


Figure 5.4: Example of time frequency map (left) and reconstructed waveform (right) for APR4 model.

5.1.1 SNR checks

As a first step, some checks have been made in order to verify the goodness of events reconstruction. I studied the reconstructed SNR as a function of the injected one, both for the single detectors and for the detector network (Fig.5.6). The mean SNR per detector is given by

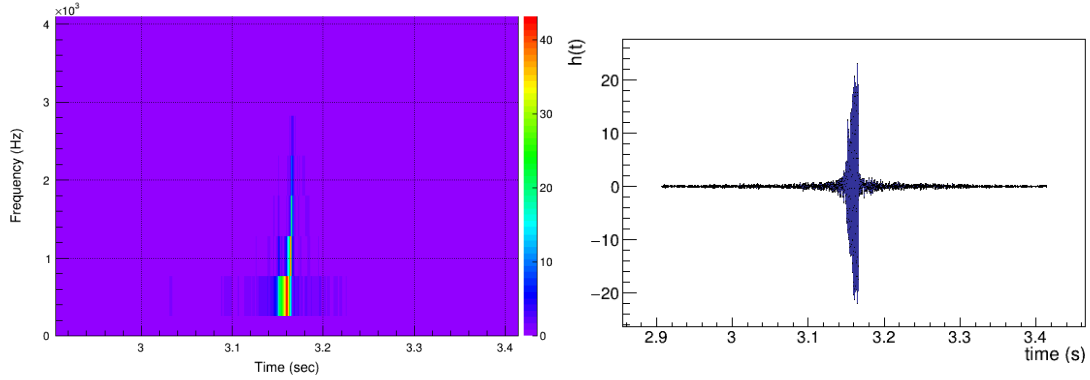


Figure 5.5: Example of time frequency map (left) and reconstructed waveform (right) for SHT-M2.2-I model.

$$SNR_{mean} = \sqrt{\frac{\sum_{k=1}^K SNR^2[k]}{K}} \quad (5.1)$$

with K number of detectors in the network.

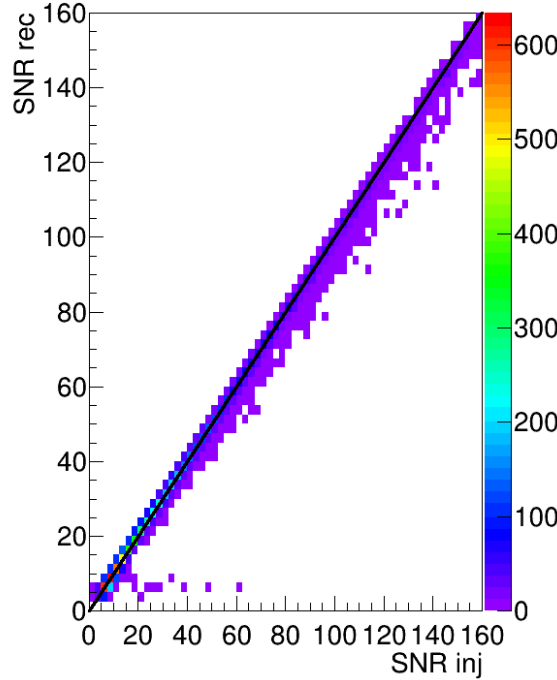


Figure 5.6: Reconstructed mean SNR as a function of injected mean SNR. The black line shows the unbiased linear model.

Since the reconstructed SNR corresponds to the maximum likelihood [57]

$$L_{max} = \frac{E - N}{2} \quad (5.2)$$

with energy

$$E = \sum_{ij} \sum_k \frac{w_k^2(i, j, \tau_k)}{\sigma_k^2(i, j)} \quad (5.3)$$

and null stream

$$N = \sum_{ij} \sum_k \frac{w_k^2(i, j, \tau_k) - \xi_k(i, j, \theta, \phi)}{\sigma_k^2(i, j)} \quad (5.4)$$

(where i and j are the time and frequency index, τ_k the k^{th} detector time of flight, θ and ϕ the sky position) we expect that the difference $SNR_{mean,inj} - SNR_{mean,rec}$ is approximately distributed as a unitary-sigma gaussian. However, since we are studying events with a post-merger that, presumably, are seen only for higher SNR, there could be a bias affecting the gaussianity. In order to study it, the reconstructed events are binned in intervals of 20-injected SNR: for each events sample the distribution of $SNR_{mean,inj} - SNR_{mean,rec}$ is reported in Fig.5.7 and fitted with a gaussian. From the plots in Fig.5.7 it is possible to observe how the events for each SNR_{inj} bin follow a gaussian distribution, although, especially at higher SNR, the distribution has a tail towards higher values of $SNR_{mean,inj} - SNR_{mean,rec}$. This is due to the fact that the reconstruction algorithm statistically misses some signal pixels, and is more accentuated at higher values of SNR because cWB was optimized for low and medium SNR.

The σ and mean of these distributions, estimated through the gaussian fit, are plotted in Fig.5.8 as functions of the central value of the SNR_{inj} interval they refer to. As expected, $\sigma \sim 1$, although it slightly increases at higher SNR, compatible with the broadening of the distribution described above. The mean value of the distributions, as expected, is compatible with zero, except for high SNR, in which case it is affected by the presence of tails of events with large bias.

Fig.5.9 displays the behavior, as a function of injected SNR, of the *size*, defined as the number of wavelet time-frequency pixels composing the events [51]. The slower increase of size with respect to injected SNR is compatible with a dismissal of signal pixel at higher SNR, which, as said before, explains the deviations of $SNR_{mean,inj} - SNR_{mean,rec}$ distributions with respect to standard gaussian. Therefore, the reconstructed SNR is suitably modeled and its bias in the high frequency range understood.

5.1.2 General time-frequency features of the reconstructed signals

In all the following analysis we considered only events with likelihood $L > 10$, where

$$L = \sqrt{\sum_{k=1}^K SNR_{rec}^2[k]}, \quad (5.5)$$

because below this value the signal is in general very weak and no post-merger can be seen. Fig. 5.10 (left and center) shows both the energy weighted bandwidth and the bandwidth defined as difference between frequencies of highest and lowest frequency of reconstructed pixels as functions of ρ , the estimator of coherent SNR per detector defined as [55]

$$\rho = \frac{E_C}{K - 1} \quad (5.6)$$

with E_C coherent energy and K number of detectors in the network.

With increasing SNR, also the bandwidth grows: at higher SNR the post-merger is more likely to be detected. Once we see the post-merger, the bandwidth includes also its frequency and hence

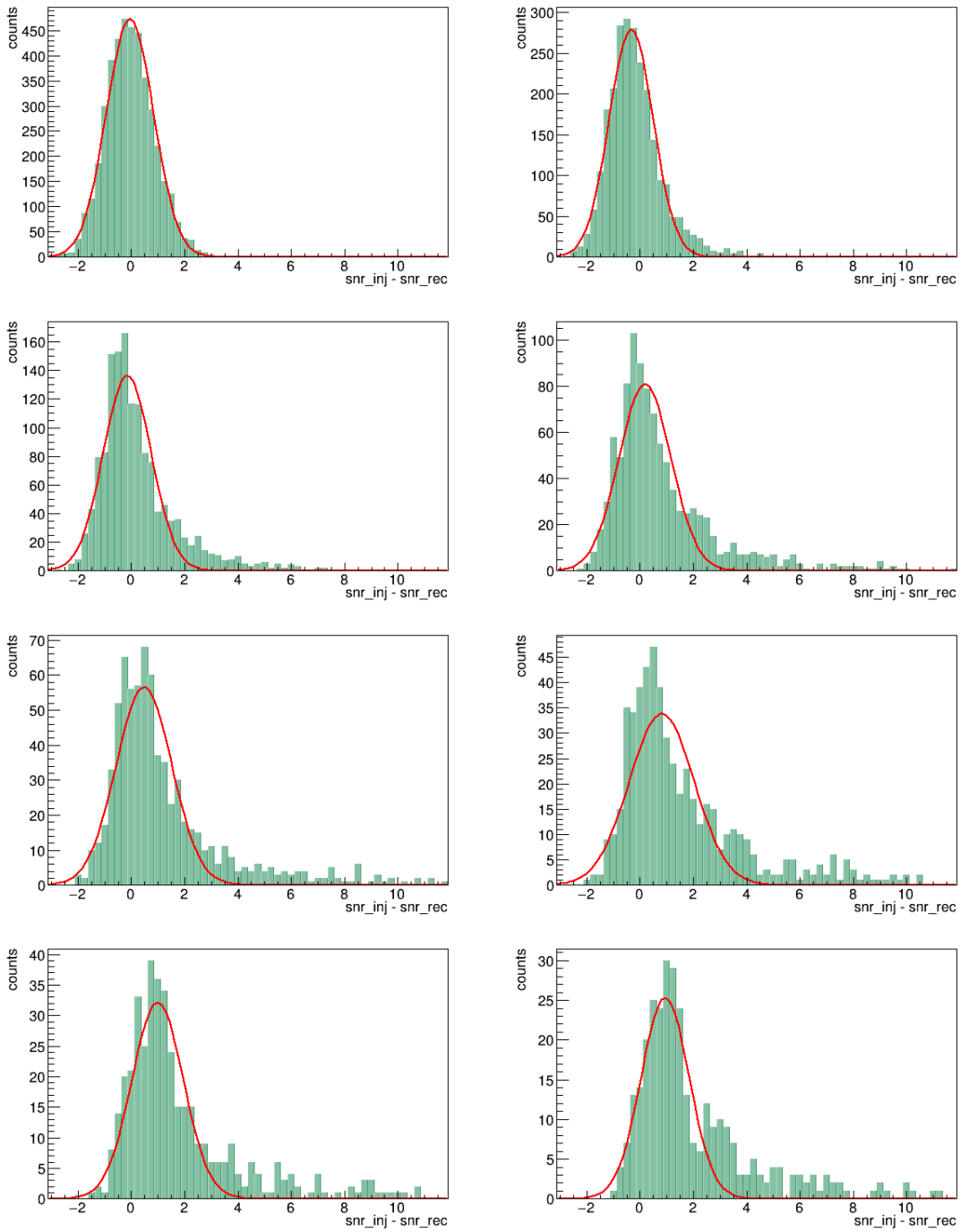


Figure 5.7: Starting from the top, $SNR_{net,inj} - SNR_{net,rec}$ distribution for the different set of events binned in intervals of 20-injected SNR. The red curve represents the gaussian fit.

reaches the kHz. The maximum bandwidth plot (Fig.5.10, left) clearly displays that at lower ρ , for which only the merger has been detected and reconstructed, most events have a bandwidth below 1kHz, while at higher ρ the most populated band is 2048-4096 Hz, matching the frequency difference expected between merger and post-merger signal.

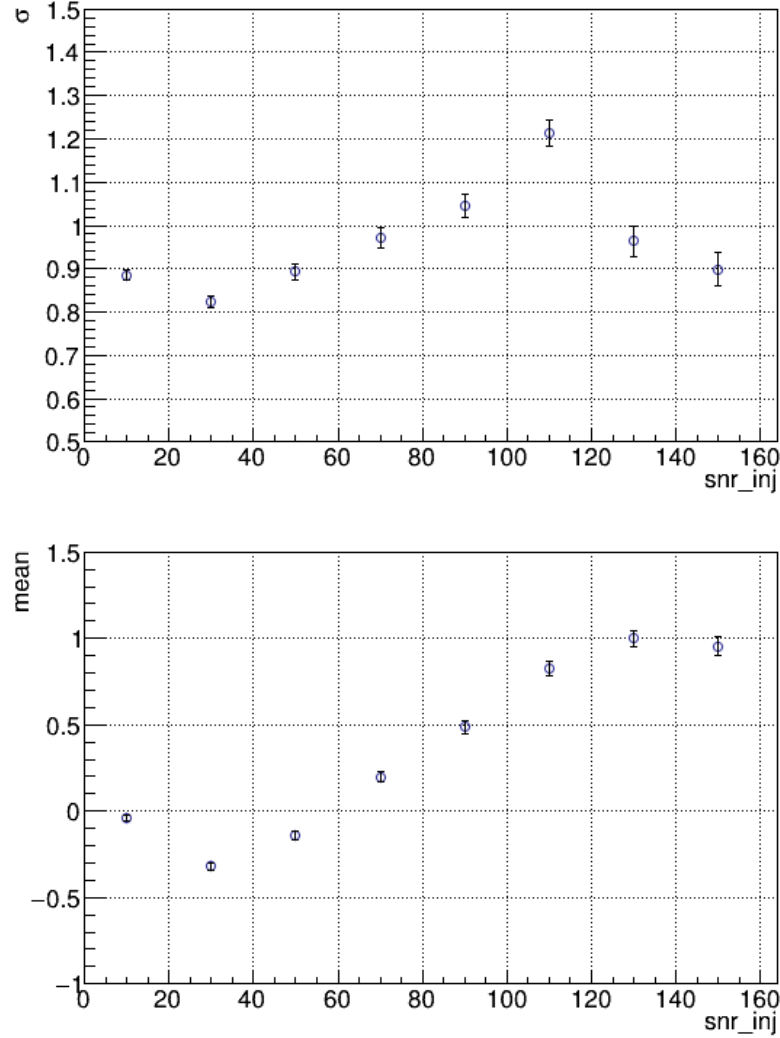


Figure 5.8: σ and mean parameters of the gaussian fit of $SNR_{net,inj} - SNR_{net,rec}$ distribution for the different injected-SNR intervals. The error bars display the statistical error.

5.2 Post-merger identification

In order to identify the post-merger in the reconstructed gravitational wave signal, we divide the TF map in 4 quadrants, setting a cut in frequency and time (an example of the applied cuts is shown in figure 5.11). As said in Section 4.1.2, the TF map is the time-frequency representation of the signal obtained with the Wilson-Daubechies-Meyer transform. It is divided in *layers* along the frequency axis, of width given by df , and *slices* along the time axis, of width dt . The grid of layers and slices defines the pixels of area $df \times dt$, each one with an energy given by the WDM amplitude. The time and frequency cuts are selected following the procedure developed in [50]. Since the merger and evolution timescales are very short, of the order of few ms, the analysis is performed with a fixed step $dt = 0.98ms \sim 1ms$. The price to pay is a low resolution for what concerns frequency: since the pixels area is constant, given by $dfdt = 1/2$, such a precision in time implies $df = 512Hz$.

The frequency cut is decided a priori as $f_{cut} = 1792Hz$, considering that the post-merger

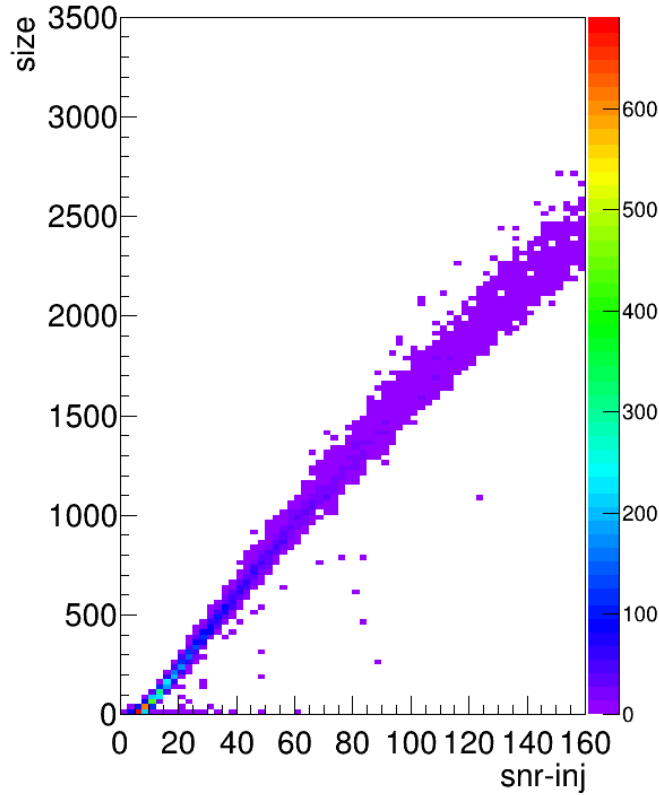


Figure 5.9: Size as a function of injected SNR.

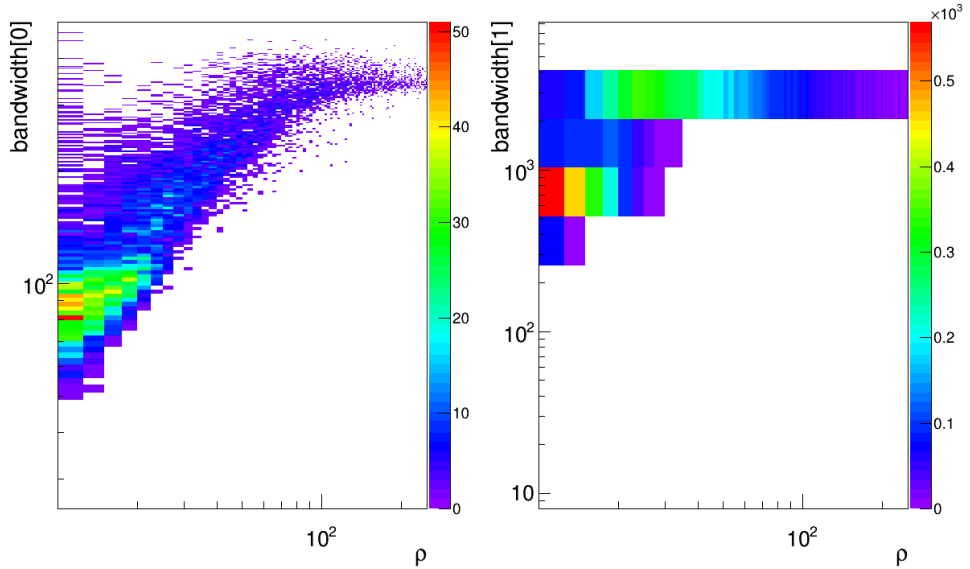


Figure 5.10: Example of checks performed on reconstructed signal's bandwidth for SHT model. In the plot on the right, the difference between pixels' highest and lowest frequency is shown in \log_2 bins in order to highlight the behavior in different frequencies bands

signal is expected to involve frequencies above this value. For what concerns time, we calculate the

energy-weighted time for each layer

$$\bar{t}_j = \frac{\sum_{i=1}^M t_{j,i} \cdot en_{j,i}}{En_j} \quad (5.7)$$

where j and i are, respectively, the layer and slice indices, M the total number of slices, $t_{j,i}$ and $en_{j,i}$ the time and energy of the (j,i) pixel, $En_j = \sum_i en_{j,i}$ the total energy of the layer. On account of the fact that the time interval between merger and post-merger is very short, we want to set the cut right after the merger time, even though this implies that also some late-merger signal is picked-up in the PM quadrant. The cut is taken at $t_{cut} = \bar{t}_2 + dt$, where dt represents the slice width in time and \bar{t}_2 an estimate of the merger time (layer 2 involves frequencies between 768 Hz and 1280 Hz, typical of merger phase). A study of the difference between \bar{t}_2 and \bar{t}_1 (Fig.5.12) showed that \bar{t}_2 is typically between 5 and 8 ms after \bar{t}_1 , therefore for those events at low SNR which do not have signal in layer 2 the cut is taken at $t_{cut} = \bar{t}_1 + 5dt$.

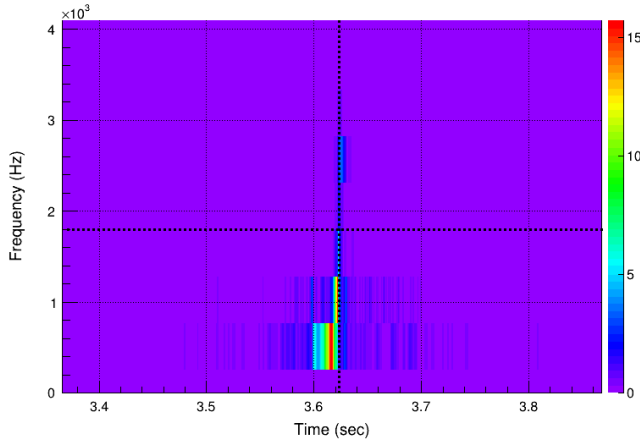


Figure 5.11: Example of time-frequency map for a reconstructed event, with the time and frequency cut identified by black dashed lines.

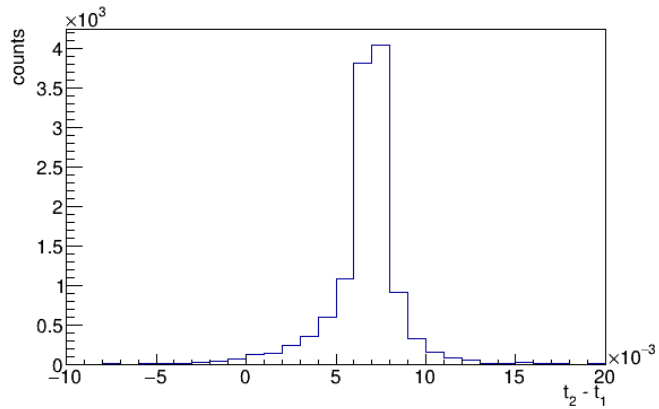


Figure 5.12: Example of $\bar{t}_2 - \bar{t}_1$ distribution for a reconstructed event.

In all the subsequent analysis, when working on the reconstructed event TF map, I considered only pixels with energy $en_{i,j} > 10^{-3}$. An example of pixels energy distribution for a reconstructed event is shown in Fig.5.13.

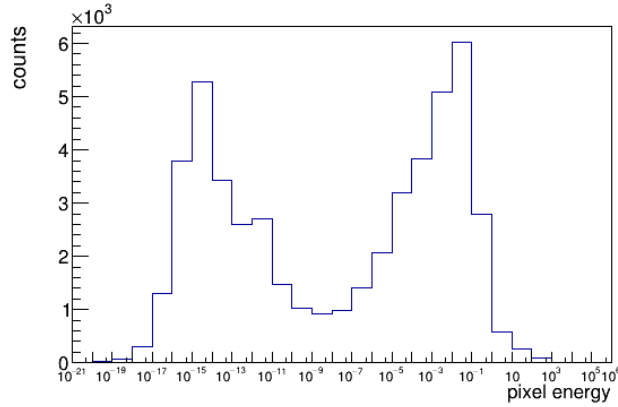


Figure 5.13: Pixels energy distribution for a reconstructed event.

5.3 Post-merger characterization in time

For the purpose to characterize the evolution in time of the post-merger signal, a first study concerns the cumulative SNR of the event. Some examples are shown in Fig.5.14 and 5.15, where the red dotted line represents t_{cut} . It can be noticed that most of the SNR increase takes place before t_{cut} , therefore, in general, only a small part can be attributed to post-merger.

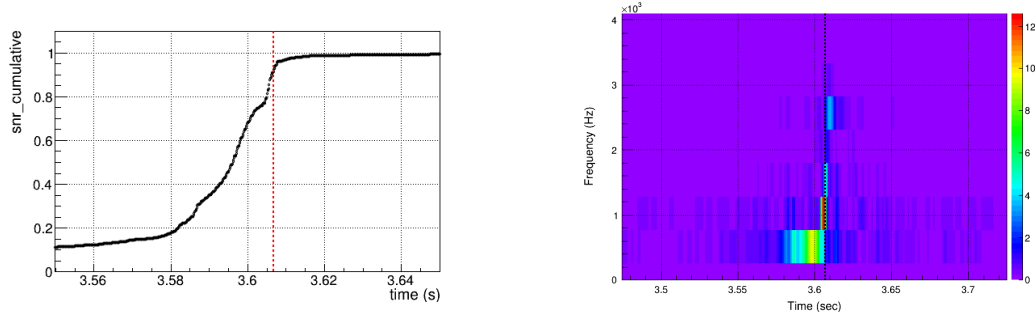


Figure 5.14: Example of SNR cumulative distribution zoomed around t_{cut} (left) with the corresponding event TF map (right).

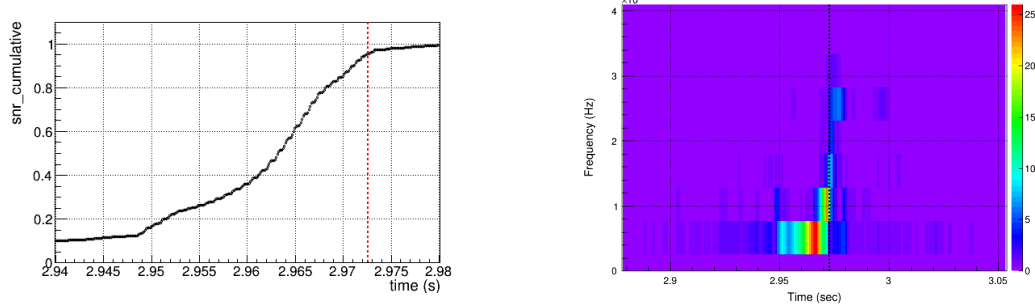


Figure 5.15: Example of SNR cumulative distribution zoomed around t_{cut} (left) with the corresponding event TF map (right).

Then, we can study the cumulative energy of the post-merger signal, namely the cumulative energy distribution computed only in the PM quadrant, parameter that will be used also later for the estimation of post-merger duration (Fig.5.30). However, we must underline that these cumulative energy distributions can be affected by a bias due to likelihood pixelization: during the reconstruction stage, the pipeline decides a pixelization for the likelihood that can imply a minimal temporal resolution greater with respect to the one of the fixed resolution analysis we perform.

Another post-merger feature interesting to study is the *luminosity profile* of the emitted gravitational wave in the PM quadrant, where the luminosity is defined as the amount of energy emitted per fixed time, in this case per time step dt . Here we display an example of this luminosity profile for some events (Fig.5.16 and 5.17), but in general this characterization is done only for events chosen with the cuts that will be summarized later (see Table 5.1). In order to study how the signal in different frequency bands contributes to luminosity, we considered the TF map region delimited by $t > t_{cut}$ and $f > 1280\text{Hz}$. The reported examples show in red the luminosity profile for $1280\text{Hz} < f < 1792\text{Hz}$, in green for $f > 1792\text{Hz}$ and in black the total one. The first, higher peak is due to a dominant contribution by the energy released in frequency band $1280 - 1792\text{Hz}$, and therefore related to late-merger signal. The post-merger part of the profile, namely the one for $f > f_{cut} = 1792\text{Hz}$, although reaching smaller values, is clearly visible and produces a peak some ms later in time. The luminosity profile of the post-merger gravitational wave could give information about the kind of remnant left after the neutron star binary coalescence [58]. However, also this quantity is affected by the pixelization problem previously explained for the cumulative energy, since the temporal resolution determined by the likelihood pixelization chosen by the pipeline could be greater than the one showed in the luminosity plots. It is interesting to compare the luminosity profile for a binary neutron star configuration expected to live as a HMNS or SMNS for a few ms and the one of a configuration that collapses promptly to a black hole. In Fig.5.18 an example is shown for SHT model, in the irrotational configuration with masses $2.2M_\odot$ (SHT-M2.2-I), and in the configuration with masses $2.0M_\odot$ (SHT-M2.0-S) and presence of spin. While the luminosity profile of the last model shows the two peaks due to late-merger and post-merger, the promptly-collapsing configuration has only one, very steep peak, almost entirely due to the signal in $1280 - 1792\text{Hz}$ band, and shows no evidence of the presence of a later luminosity peak at higher frequencies.

5.3.1 Energy ratio

A very interesting piece of information concerns how much energy is carried by the reconstructed post-merger signal with respect to the total event energy, namely

$$E_{ratio} = \frac{E_{PM}}{E_{tot}} \quad (5.8)$$

where E_{PM} is the energy computed in the PM quadrant, delimited by t_{cut} and f_{cut} , and E_{tot} the one computed over the whole TF map. However, due to fragmentation or signal weakness some events do not have a post-merger, and, in these cases, the tools for PM characterization cannot be applied clearly. For this reason, I computed the energy weighted time \bar{t}_4 in the post-merger quadrant and

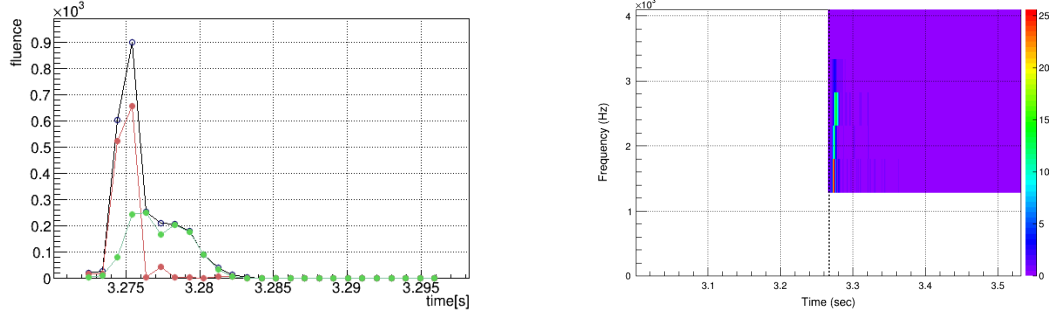


Figure 5.16: Example of an event luminosity profile (left) and respective TF map(right). In order to distinguish the behavior at different frequencies, beyond the total event luminosity (black), we show the luminosity profile at frequencies between $1280 - 1792\text{Hz}$ in red and for frequencies above 1792 Hz in green.

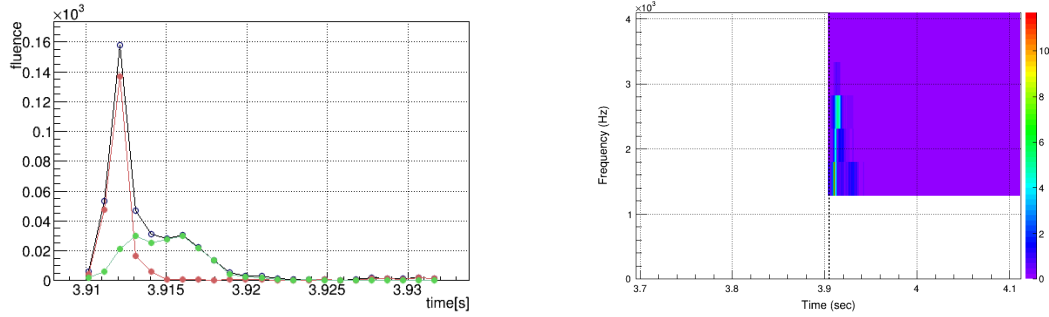


Figure 5.17: Example of an event luminosity profile (left) and respective TF map(right). In order to distinguish the behavior at different frequencies, beyond the total event luminosity (black), we show the luminosity profile at frequencies between $1280 - 1792\text{Hz}$ in red and for frequencies above 1792 Hz in green.

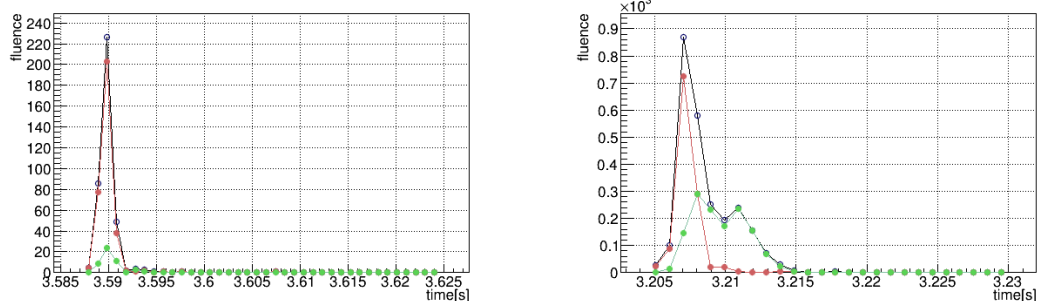


Figure 5.18: Example of an event luminosity profile for model SHT-M2.2-I, expected to collapse promptly to a black hole(left), and one for model SHT-M2.2-S (right), which is expected to survive a few ms before the collapse.

the energy-weighted time \bar{t}_3 in the TF map region delimited by t_{cut} and $f > 1280\text{Hz}$, in order to verify that there exists a post-merger event at higher frequencies. For all the following post-merger analysis I considered only events for which $\bar{t}_4 > \bar{t}_3$.

Going back to the post-merger energy, Figures 5.19 to 5.22 show the distribution of E_{ratio} with its cumulative for every waveform model analyzed, taking into account only the reconstructed

events with $L > 10$ and $\bar{t}_4 > \bar{t}_3$.

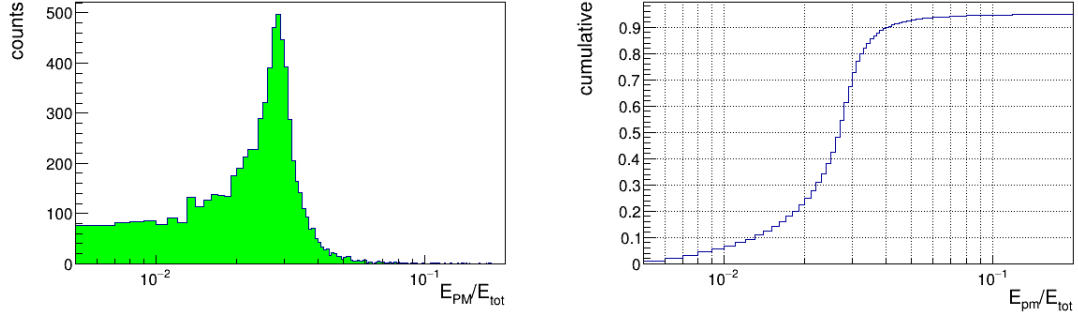


Figure 5.19: E_{ratio} distribution (left) and its cumulative (right) for SHT-M2.2-S model.

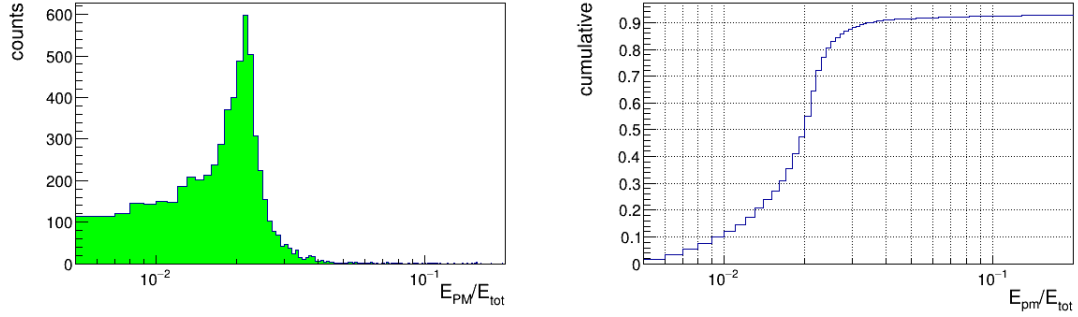


Figure 5.20: E_{ratio} distribution (left) and its cumulative (right) for LS220 model.

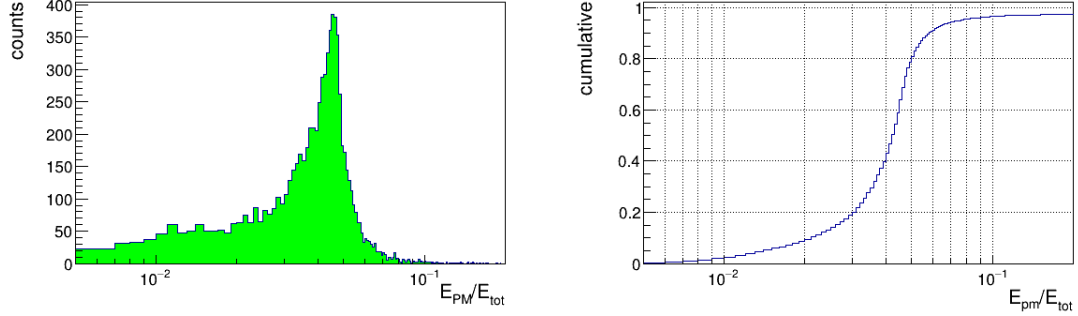


Figure 5.21: E_{ratio} distribution (left) and its cumulative (right) for H4 model.

From these distributions we can infer mainly two things: the reconstructed post-merger energy is in general few percent of the total reconstructed signal energy, and the energy ratio distribution is peaked at different values depending on the model.

E_{ratio} becomes also a useful parameter in order to further discriminate whether a sufficiently energetic post-merger signal is present or not. For the following steps of the analysis, we considered only events with

$$E_{\text{ratio}} \geq 0.5\% \quad (5.9)$$

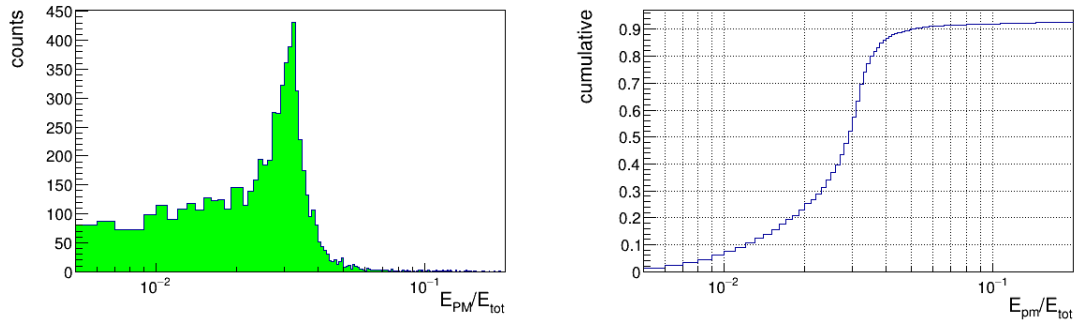


Figure 5.22: E_{ratio} distribution (left) and its cumulative (right) for APR4 model.

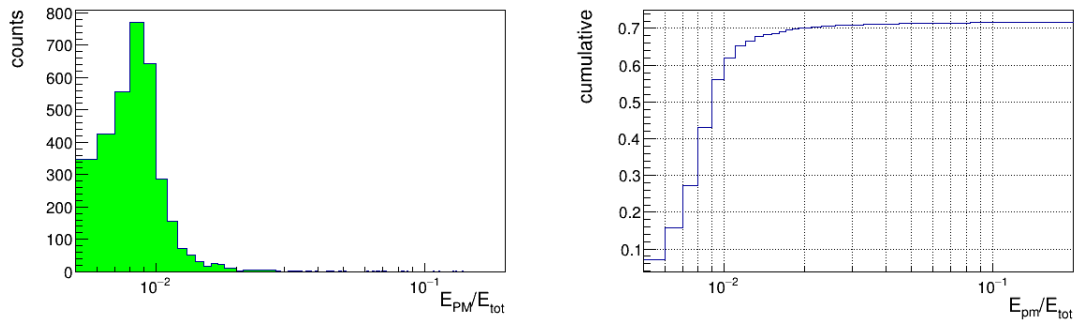


Figure 5.23: E_{ratio} distribution (left) and its cumulative (right) for SHT-M2.2-I model.

In Fig.5.24 is shown an example of behavior of E_{ratio} as a function of the mean reconstructed SNR for the SHT-M2.0-S model.

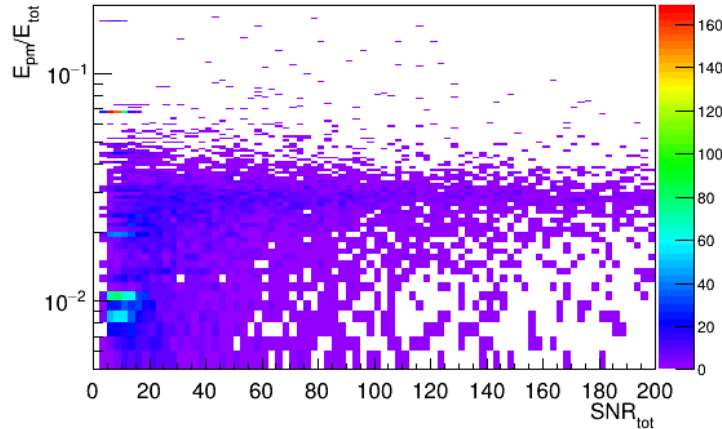


Figure 5.24: Example ov events E_{ratio} distribution as a function of their reconstructed SNR

To summarize, in order to consider only reconstructed events with a post-merger signal, for all the following analysis we take into account only events chosen with the cuts reported in Table 5.1. Table 5.2 contains for each model the total number of reconstructed events, the number of those with $L > 10$ and of the ones that are compatible with all the cuts and hence are considered for the analysis.

Events cuts
$L > 10$
$\bar{t}_4 > \bar{t}_3$
$E_{ratio} > 0.5\%$

Table 5.1: Summary of the cuts set on the reconstructed events for the post-merger characterization analysis.

Model	Entries	$L > 10$	All cuts
SHT-M2.0-S	12807	12360	7237
LS220-M1.5-S	13040	12607	6411
H4-M1.5	12990	12522	7921
APR4-UM	12867	12436	6853
SHT-M2.2-I	13167	12736	4887

Table 5.2: Table reporting, for the various models considered, the total number of reconstructed events, the number of those events with $likel > 10$ and the ones that pass all the cuts.

A first feature that can be used to characterize the post-merger is the energy distribution at high frequencies. In particular, we are interested in studying, always for $t > t_{cut}$, how much energy is there in the reconstructed signal between 1280 and 1792 Hz, and for $f > 1792\text{Hz}$. Figures from 5.25 to 5.29 show the distribution of E_{PM}/E_3 and its cumulative for the various models.

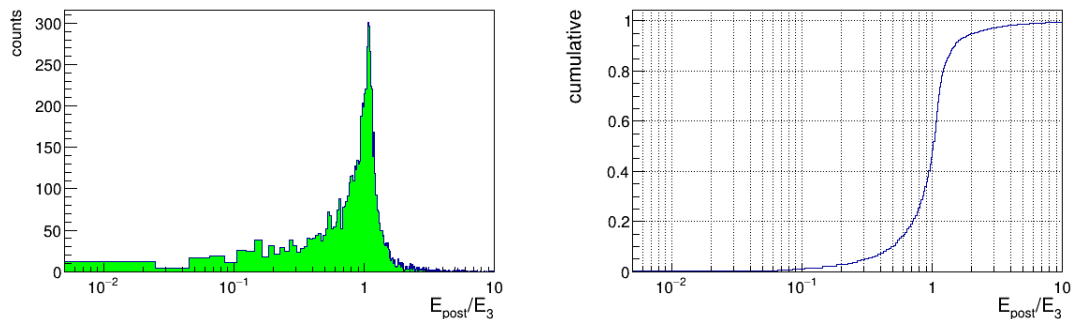


Figure 5.25: E_{PM}/E_3 distribution (left) and its cumulative (right) for SHT-M2.2-I model.

5.3.2 Time duration of post-merger signal

The aim now is to study the duration of the post-merger signal and its time evolution. For this purpose, for each event, I identified the time at which the cumulative energy distribution in the post-merger quadrant reaches 10% and 90%, called respectively t_{10} and t_{90} . More precisely, since we measure time in a quantized way, with step dt , I take t_{10} as the time of the pixel just before the effective time the cumulative reaches 10%, and t_{90} as the time of the pixel immediately after the

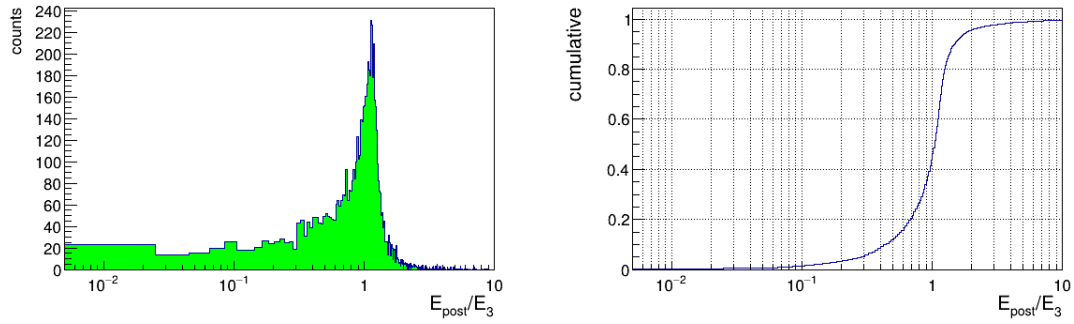


Figure 5.26: E_{PM}/E_3 distribution (left) and its cumulative (right) for LS220 model.

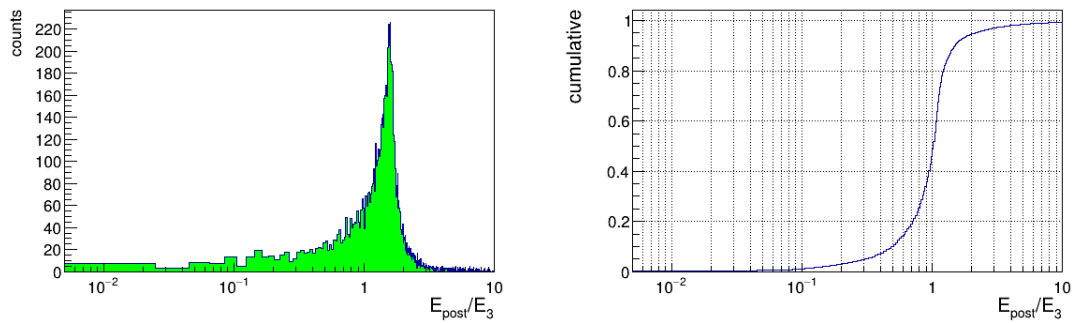


Figure 5.27: E_{PM}/E_3 distribution (left) and its cumulative (right) for H4 model.

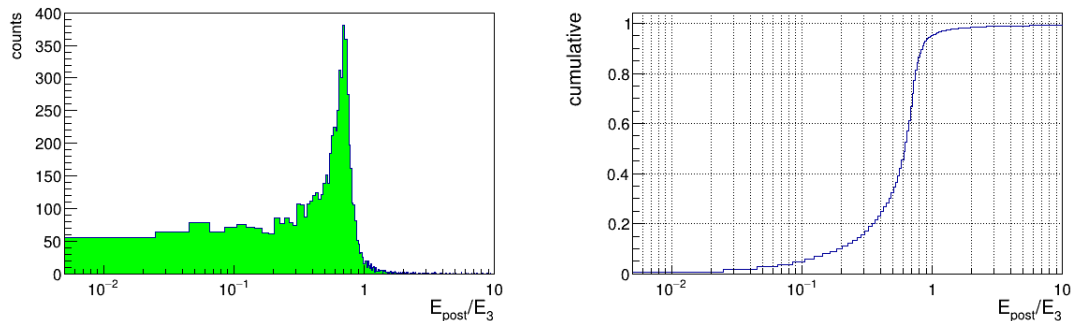


Figure 5.28: E_{PM}/E_3 distribution (left) and its cumulative (right) for APR4 model.

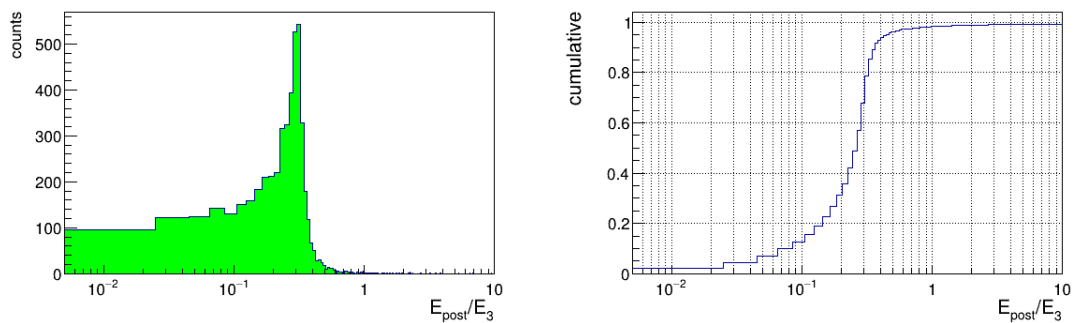


Figure 5.29: E_{PM}/E_3 distribution (left) and its cumulative (right) for BH model.

time it reaches 90%. Some example are shown in Fig.5.30, where the black dotted line represents

t_{10} and the red dotted line t_{90} .

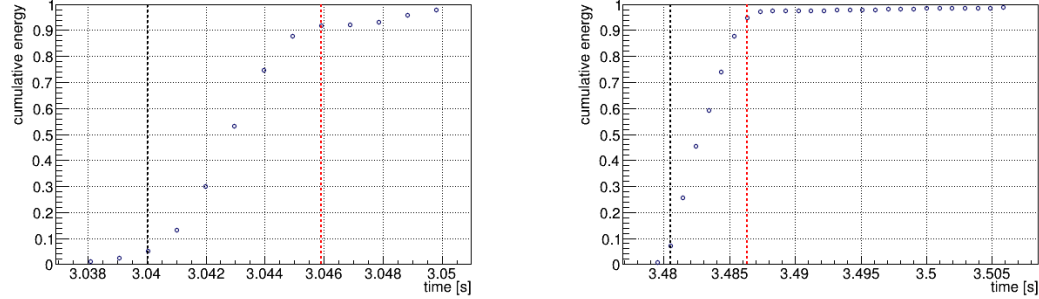


Figure 5.30: Example of cumulative energy distribution for a couple of events, with t_{10} and t_{90} reported by black and red dotted lines respectively.

We define the time duration of post-merger signal as

$$\Delta t = t_{90} - t_{10} \quad (5.10)$$

This quantity, corresponding to the time interval in which 80% of PM-quadrant signal is detected, has been calculated for each event. The Δt distribution for each model is shown in Fig.5.31.

These plots play a fundamental role in our discussion, since they highlight how post-merger duration does depend on the waveform model, therefore on the EoS assumed for neutron stars. The peak values, the width and the trend of the distribution are different for the various model considered.

In order too see how the SNR of the event affects this distribution, figures 5.32 to 5.36 display the Δt distribution, for the various models, of events in different slots of SNR: 15 ± 5 , 30 ± 5 , 60 ± 5 and 120 ± 5 . Increasing the SNR, the distribution becomes narrower.

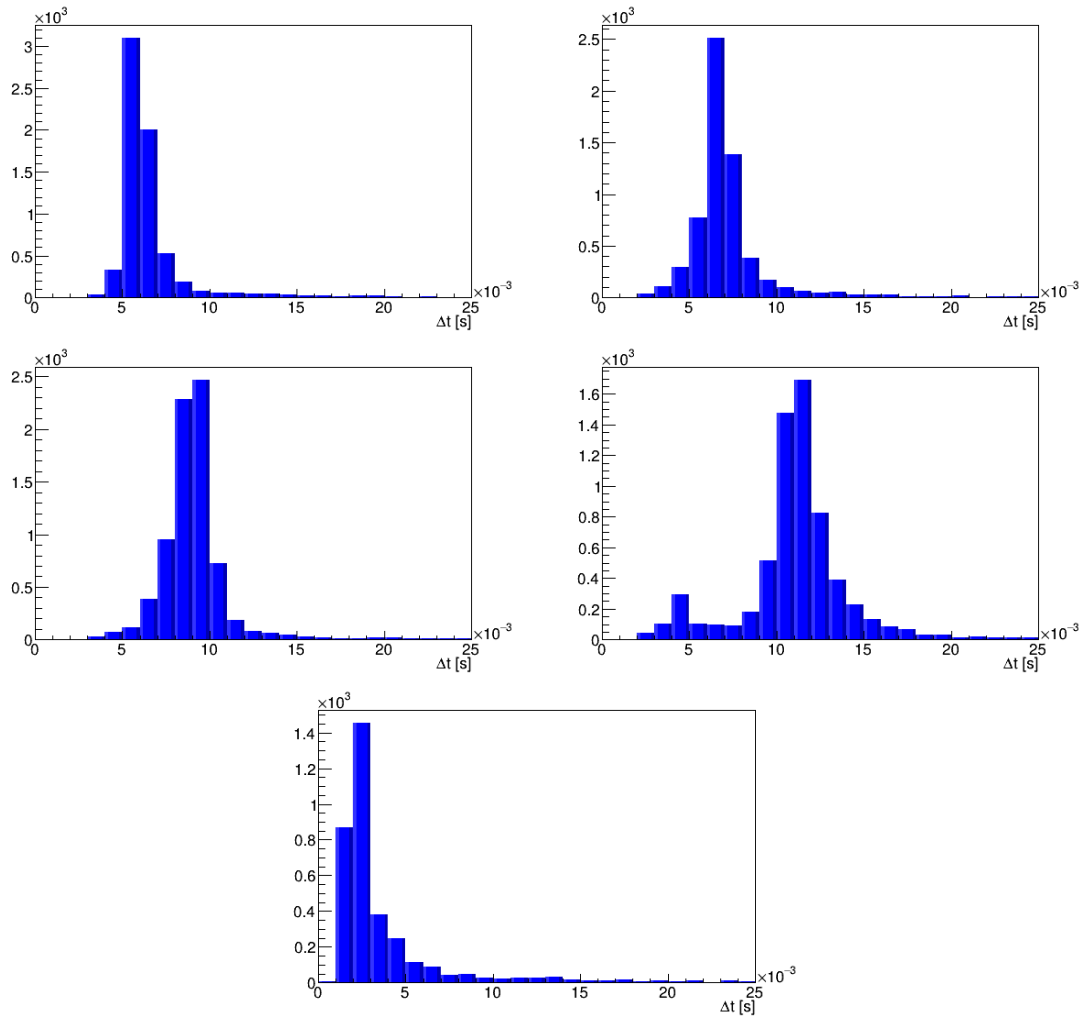


Figure 5.31: Post-merger Δt normalized distribution for SHT-M2.0-S model (*top left*), LS220 model (*top right*), H4 model (*middle left*), APR4 model (*middle right*) and SHT-M2.2-I model (*bottom*).

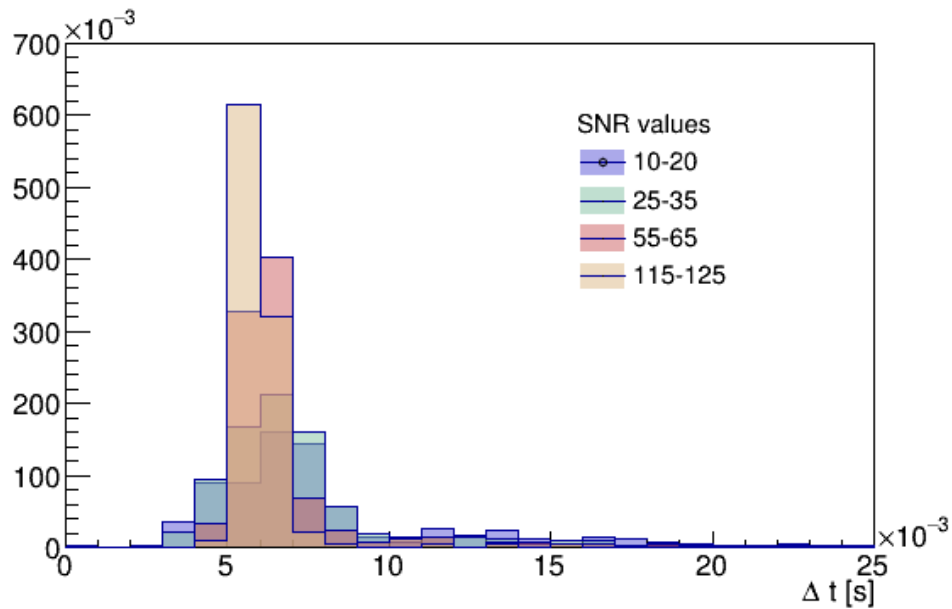


Figure 5.32: Δt normalized distribution of events with different values of reconstructed SNR for SHT-2.0-S model.

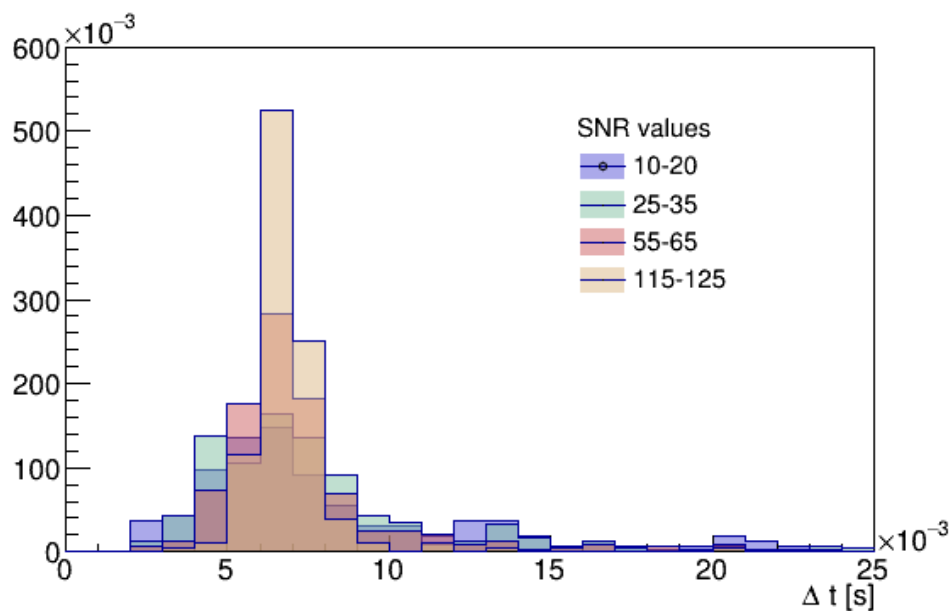


Figure 5.33: Δt normalized distribution of events with different values of reconstructed SNR for LS220 model.

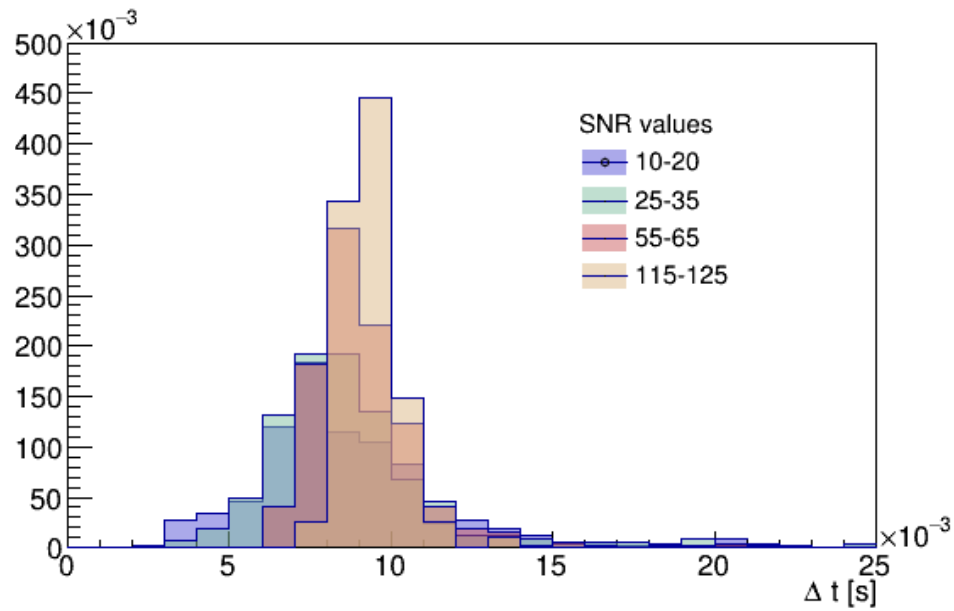


Figure 5.34: Δt normalized distribution of events with different values of reconstructed SNR for H4 model.

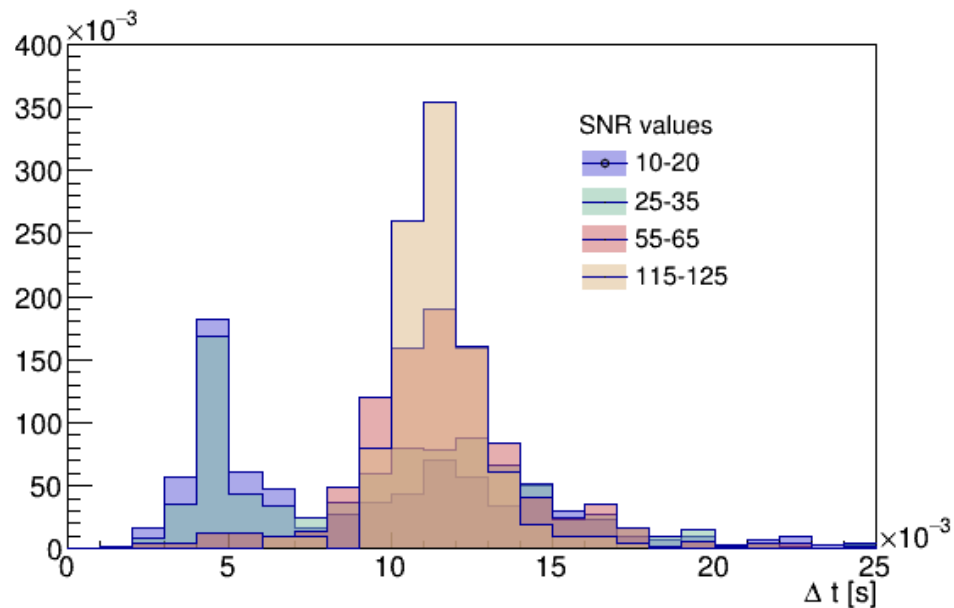


Figure 5.35: Δt normalized distribution of events with different values of reconstructed SNR for APR4 model.

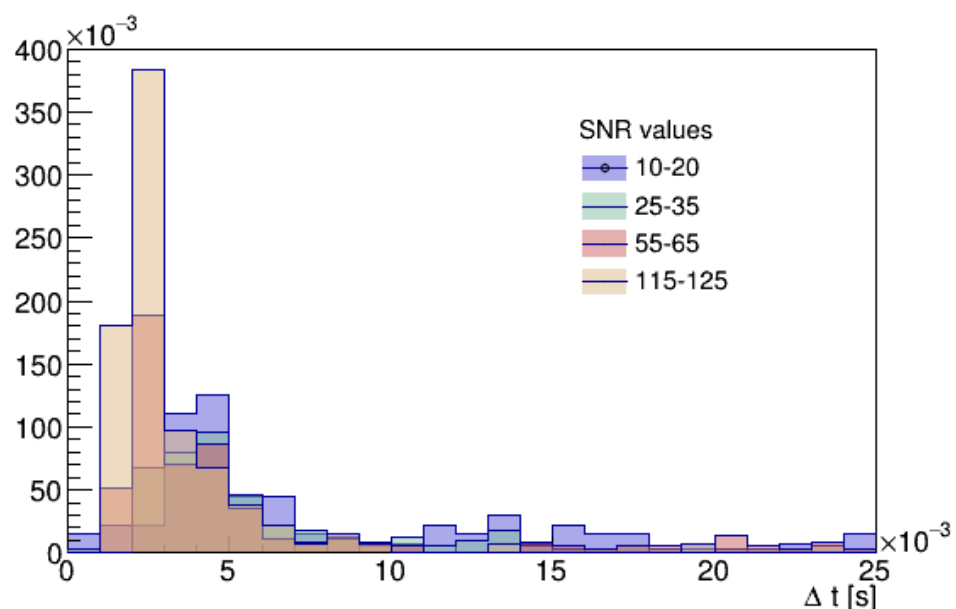


Figure 5.36: Δt normalized distribution of events with different values of reconstructed SNR for SHT-M2.2-I model.

5.4 Spectral characterization

For the purpose to characterize the post-merger in frequency domain, the first feature we want to estimate is the frequency peak of post-merger signal. To do that, the signal is brought back to time domain with an anti-WDM transform and its Power Spectral Density is computed starting from the Fast Fourier transform (FFT). For all this operation I considered only the data in PM quadrant; some examples are shown in Fig.5.37 and Fig.5.38. The main frequency peak is then fitted with a gaussian function, in order to estimate the central frequency. In some cases the PSD has two peaks, one corresponding to the post-merger signal and one at lower frequencies due to some remaining late-merger signal.

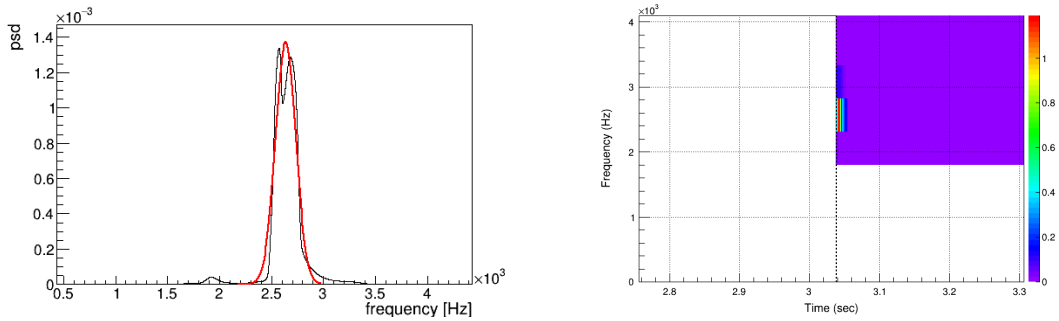


Figure 5.37: Example of an event PSD in PM quadrant (left) and respective TF map(right). The red curve represents the gaussian function used to fit the frequency peak. In this case, the post-merger signal is very clean, resulting in very well defined PSD peak in the frequency range expected for post-merger.

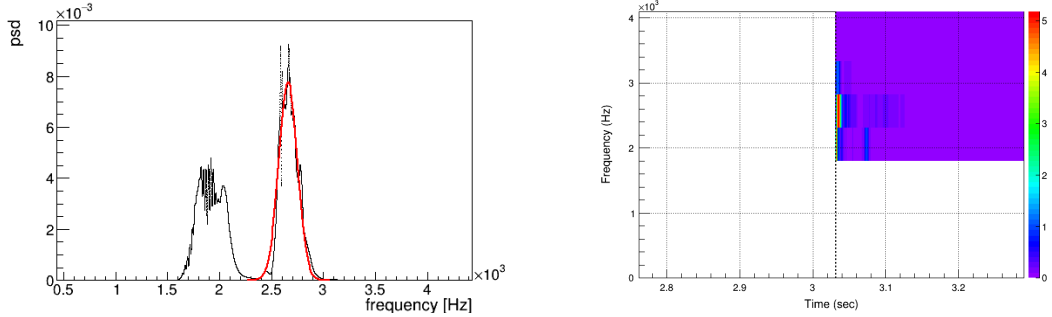


Figure 5.38: Example of an event PSD in PM quadrant (left) and respective TF map(right). In this case the late merger brings an important contribution to the PM quadrant signal, indeed the first PSD peak is very high. Although the late-merger signal has a higher SNR, it is spread a wider range of frequencies, therefore the PSD peak is not well defined and results lower with respect to the post-merger one.

Different estimators are the energy weighted frequency and bandwidth in the PM quadrant. In order to calculate them, we considered TF maps of reconstructed events with a better resolution in frequency, choosing $df = 64\text{Hz}$ and, consequently, $dt = \approx 7.8\text{ms}$. This choice implies that we loose all the precision in time, but here we are not interested in the time evolution of the signal.

For the identification of the post-merger quadrant we keep the t_{cut} previously found and, in order to cut at a layer edge, the frequency cut is now taken at $f'_{cut} = 1760\text{Hz}$. An example of TF map with this resolution and cut is shown in Fig.5.39.

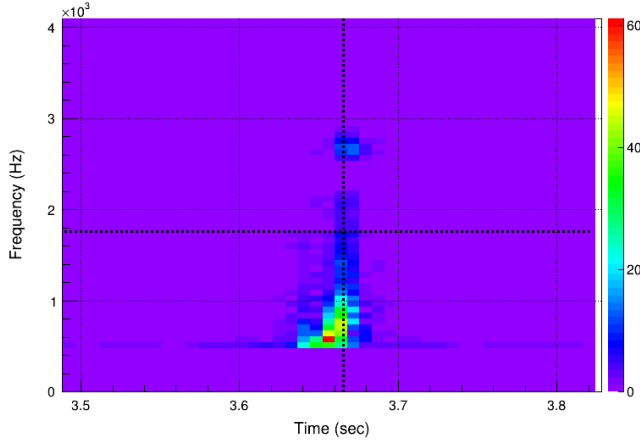


Figure 5.39: TF map of a reconstructed event at frequency resolution $df = 64\text{Hz}$. The black dotted lines represent t_{cut} and f'_{cut} chosen for the post-merger quadrant identification.

The weighted frequency is then calculated as

$$f_w = \frac{\sum_{ij} f_{ij} \cdot en_{ij}}{\sum_{ij} en_{ij}} \quad (5.11)$$

where the pixel's frequency f_{ij} is taken as the the central frequency of the layer the pixel belongs to. The distribution of weighted frequency for the four analyzed waveform models are shown in Fig.5.40. These distributions and their peak values are different for the various models considered, in particular the distribution for the model expected to collapse promptly to a black hole is peaked at the lower end of the frequency range considered.

In Fig.5.41 is shown an example of behavior of the energy-weighted frequency as a function of the mean reconstructed SNR for the SHT-M2.0-S model.

On the same SNR bins used in the previous section, figures 5.42 to 5.46 illustrate the conditional pdf of the energy weighted frequency estimate for the different waveform models. The events at lower SNR follow a much wider distribution with, in general, two different peaks at lower and frequencies with respect to main peak, that instead corresponds to the distribution of events with higher SNR.

For what concerns the weighted frequency bandwidth, it is calculated as the weighted variance

$$b_w = \frac{\sum_{i=1}^N f_{c,i}^2 en_i}{\sum_{i=1}^N en_i} - \left(\frac{\sum_{i=1}^N f_{c,i} en_i}{\sum_{i=1}^N en_i} \right)^2. \quad (5.12)$$

The distribution of b_w over events is shown in figures 5.47 to 5.51for all the analyzed models. Models corresponding to a HMNS or SMNS have sharp distributions with well-defined peaks at different values, with some counts at small bandwidth corresponding to events in which the post-merger has not been reconstructed. The SHT-M2.2-I model, instead, displays a very different distribution, wider and at lower bandwidth values.

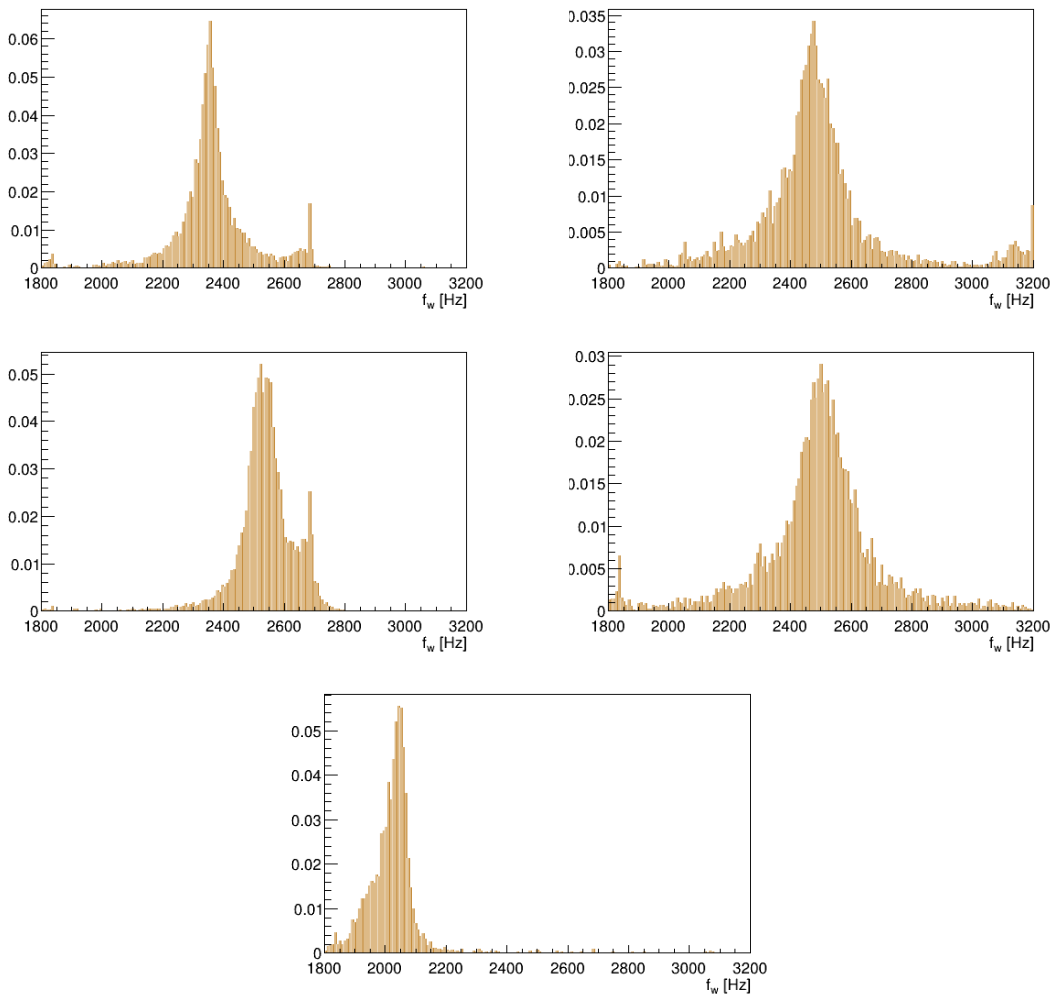


Figure 5.40: Normalized distribution of post-merger energy-weighted frequency for SHT-M2.0-S model (*top left*), LS220 model (*top right*), H4 model (*middle left*), APR4 model (*middle right*) and SHT-M2.2-I model (*bottom*).

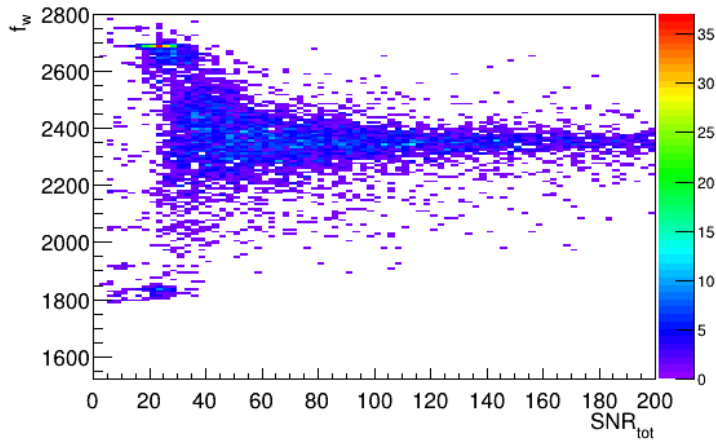


Figure 5.41: Example ov events energy-weighted frequency distribution as a function of their reconstructed SNR

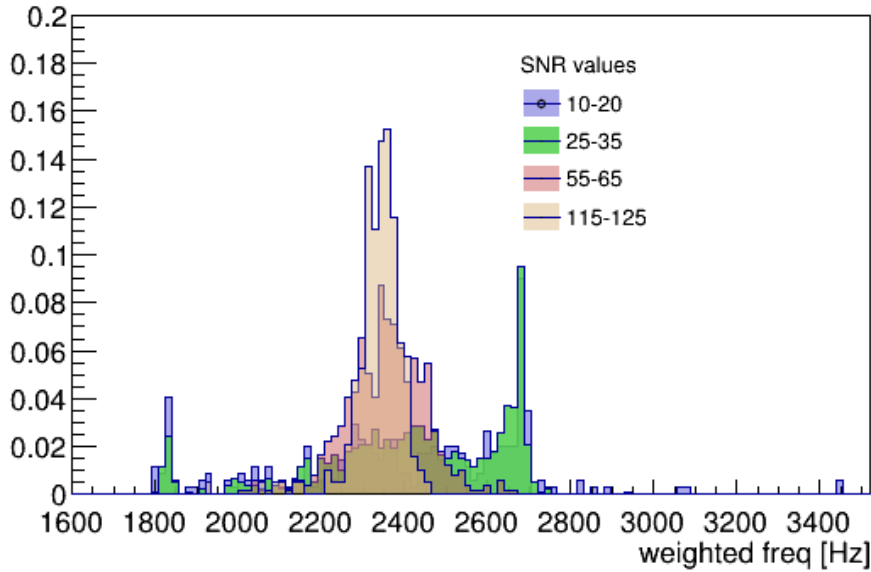


Figure 5.42: Weighted frequency distribution of events with different values of reconstructed SNR for SHT-2.0-S model.

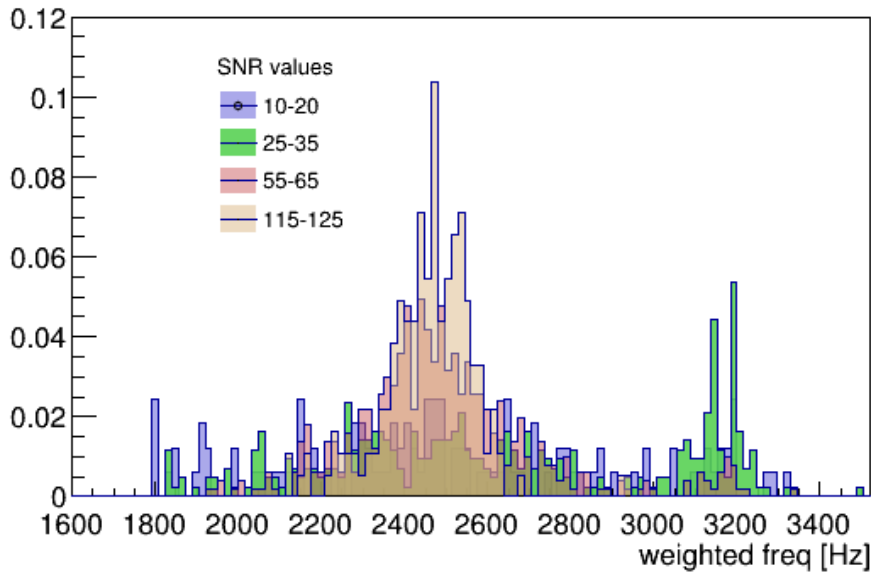


Figure 5.43: Weighted frequency distribution of events with different values of reconstructed SNR for LS220 model.

The distribution of our frequency and bandwidth estimates at moderate to strong SNR values show large morphological difference as a function of the waveform model. This information can therefore be used to help identify the presence of a post-merger emission from a NS remnant and enable some classification of the EOS, as discussed in the next chapter.

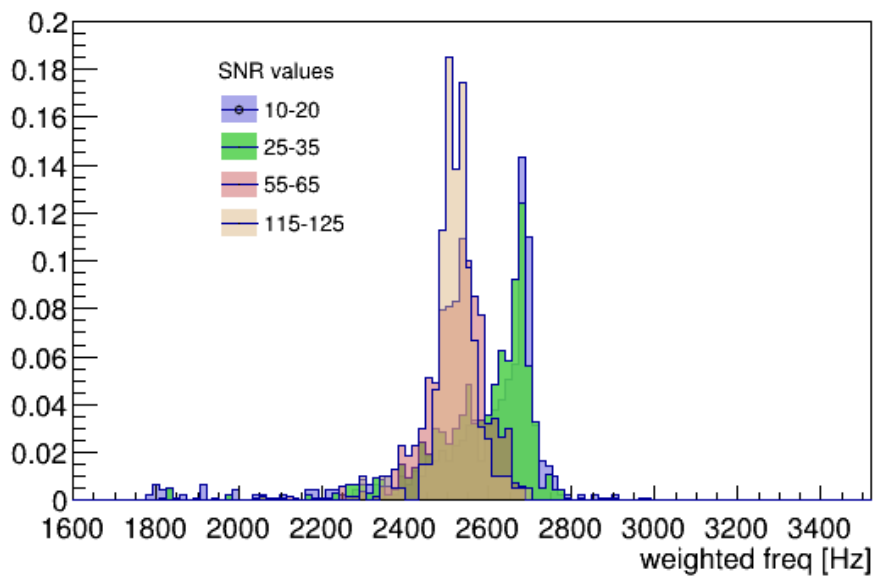


Figure 5.44: Weighted frequency distribution of events with different values of reconstructed SNR for H4 model.

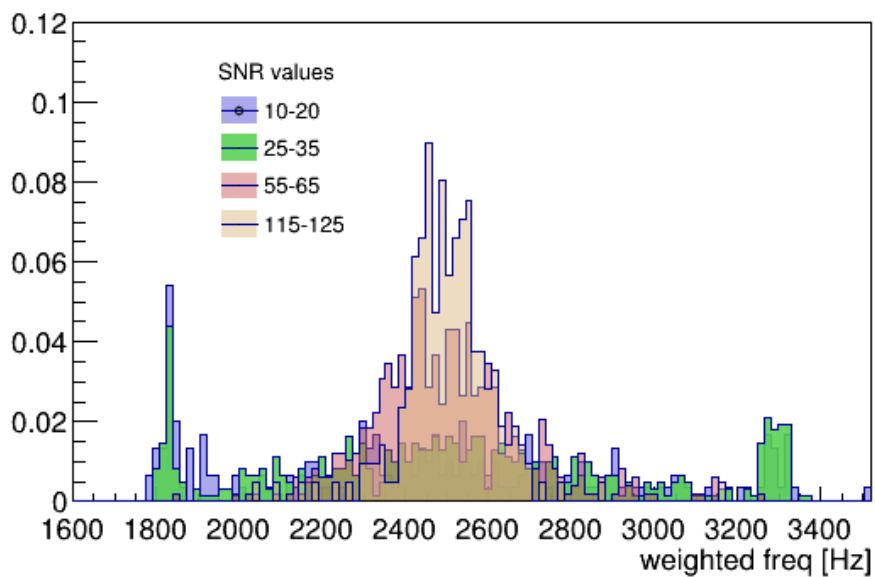


Figure 5.45: Weighted frequency distribution of events with different values of reconstructed SNR for APR4 model.

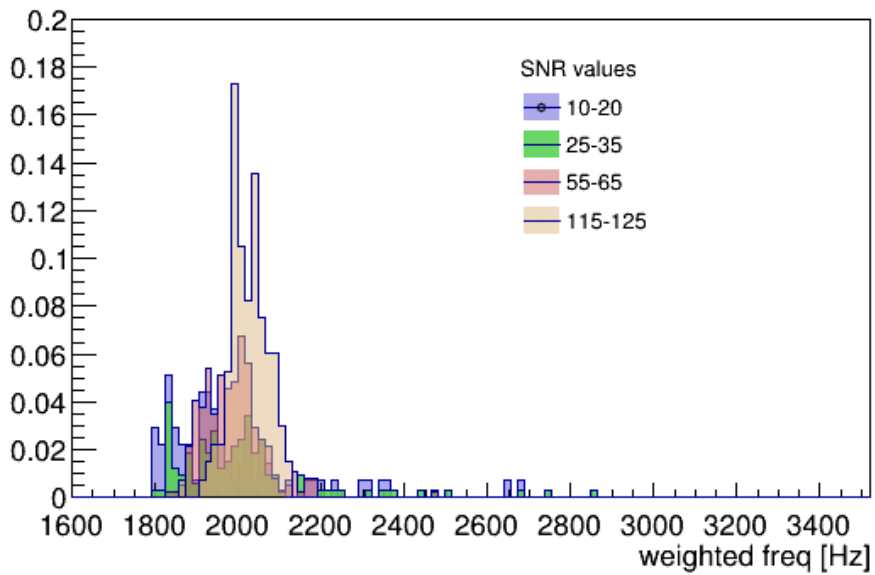


Figure 5.46: Weighted frequency distribution of events with different values of reconstructed SNR for SHT-M2.2-I model.

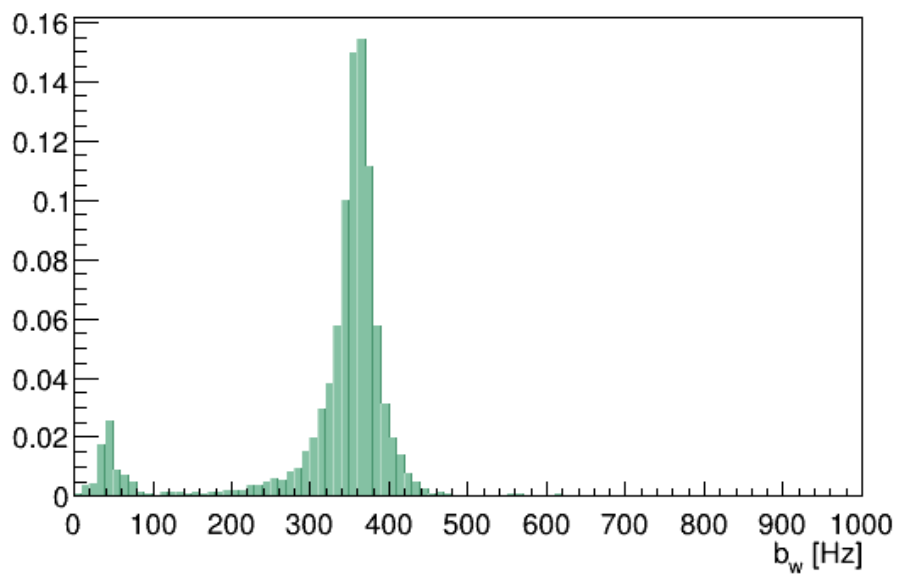


Figure 5.47: Post-merger energy-weighted normalized distribution for SHT-M2.0-S model.

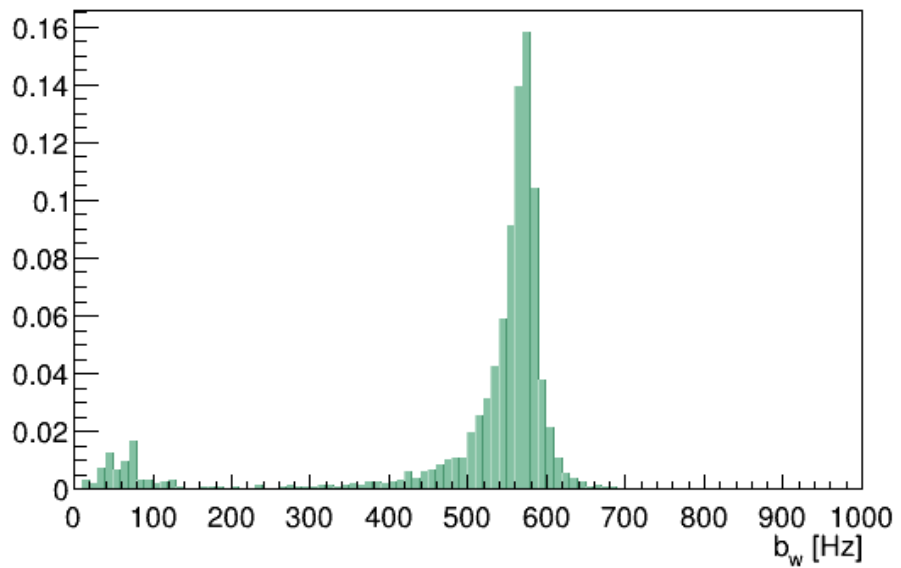


Figure 5.48: Post-merger energy-weighted normalized distribution for LS220 model.

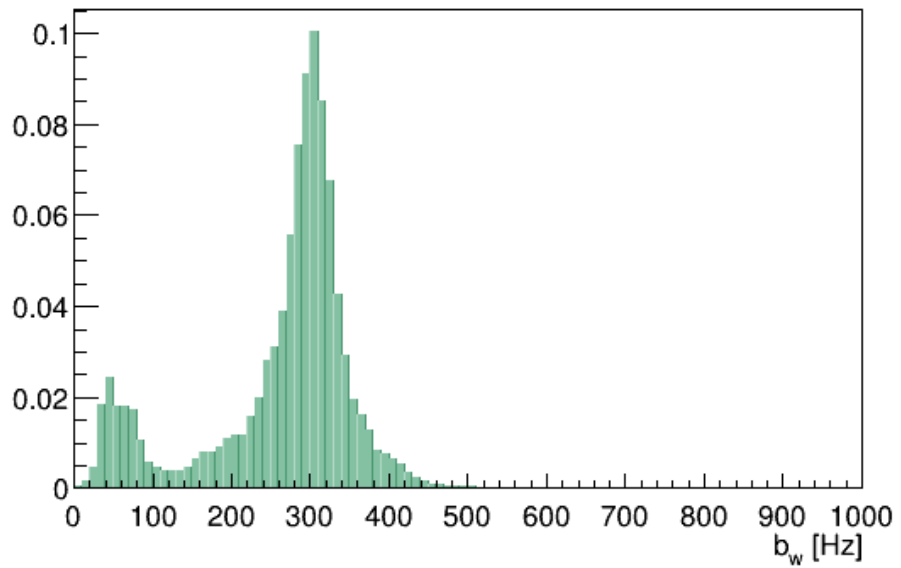


Figure 5.49: Post-merger energy-weighted bandwidth normalized distribution for H4 model.

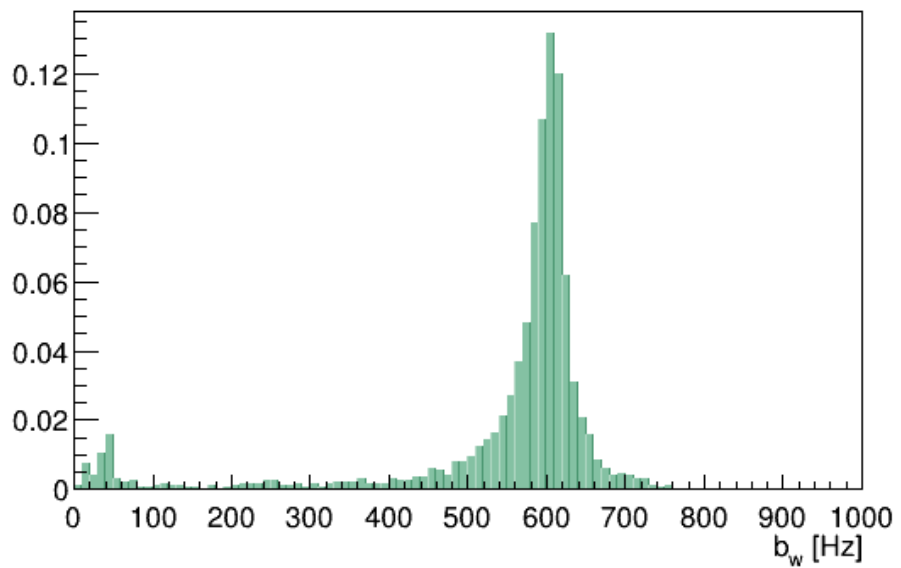


Figure 5.50: Post-merger energy-weighted bandwidth normalized distribution for APR4 model.

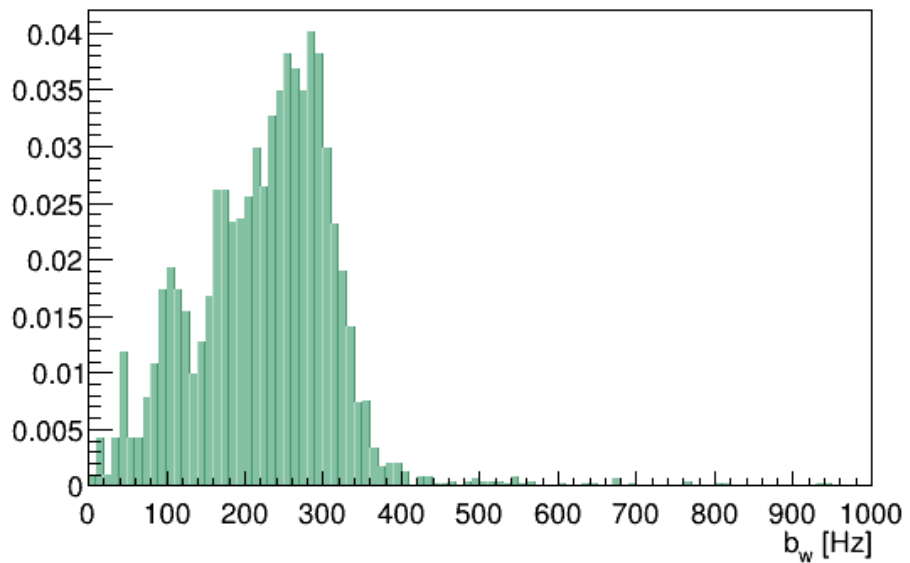


Figure 5.51: Post-merger energy-weighted bandwidth normalized distribution for SHT-M2.2-I model.

Chapter 6

Inferring properties of the post-merger source

In previous chapter we found a method to characterize the reconstructed post-merger gravitational wave signal from a BNS through some estimated parameters. The main estimators we have constructed are: ratio between the energy in the post merger region, for $f > 1792\,Hz$ and $t > t_{cut}$, and energy in the third layer, namely in frequency band $1280 - 1792\,Hz$; luminosity profile and post-merger signal duration, for what concerns time characterization; energy weighted frequency and bandwidth regarding spectral characterization. Now we want to use these estimators to draw some conclusions about the astrophysical interpretation of a signal. Working on simulated signals, we applied some thresholds, such as $E_{pm}/E_{tot} > 0.5\%$ (see Section 5.3.1), in order to pre-select sufficiently energetic post-merger signals on which perform the analysis. However, if a real post-merger is detected, in most cases its energy will be lower, therefore when working on real signals our method should be extended to a sub-threshold analysis. In the case of analysis of future real observations, this condition will be relaxed and this method must be extended to a sub-threshold analysis. Indeed, as already mentioned in Section 3.8, for the BNS detection GW170817 the post-merger search gave null result both for short ($\lesssim 1s$) and intermediate-duration ($\lesssim 500s$) signals [36]. The analysis reported in [36] set an upper limit on the root-sum-square of the GW strain emitted in $1 - 4\,kHz$, at 50% detection efficiency [62], of $h_{rss}^{50\%} = 2.1 \times 10^{-22}\,Hz^{-1/2}$ for short-lived HMNS, and, for SMNS or massive NS, an upper limit between $h_{rss}^{50\%} = 8.4 \times 10^{-22}\,Hz^{-1/2}$ and $h_{rss}^{50\%} = 5.9 \times 10^{-22}\,Hz^{-1/2}$ depending on the model, which is not yet achieving ranges of interests for the astrophysical interpretation.

The method we present in this chapter is a pilot study and must be extended to obtain a systematic approach. Our results and conclusions are necessarily limited to the waveform models we consider. However, none of the models taken into account has been excluded by the BNS detection [31] and they cover a good diversity of the possible signal parameter space.

Our goal here is to investigate the possible discrimination between two scenarios, the prompt-collapse to a black hole or the formation of a remnant that survives for a certain time as a HMNS or SMNS before collapsing to a black hole. Moreover, in presence of evidence for a NS remnant emission, we test the capability to select which equation of state better explains the observation. This is performed by considering the estimators characterized in previous section, E_{post}/E_3 , the

luminosity profile and the energy-weighted bandwidth.

6.1 Criteria for the detection of a post-merger emission

We describe a statistics test on the E_{post}/E_3 (defined in Sec.5.3.1) distribution, whose cumulative is shown in Fig.6.1 for every model considered. The reference distribution for a prompt-collapse to a black hole is given by the one for the SHT-M2.2-I model, the reference for the formation of a NS remnant instead is given by the sum of the other models PDF, assuming a flat prior. The two reference distributions are shown in Fig.6.2.

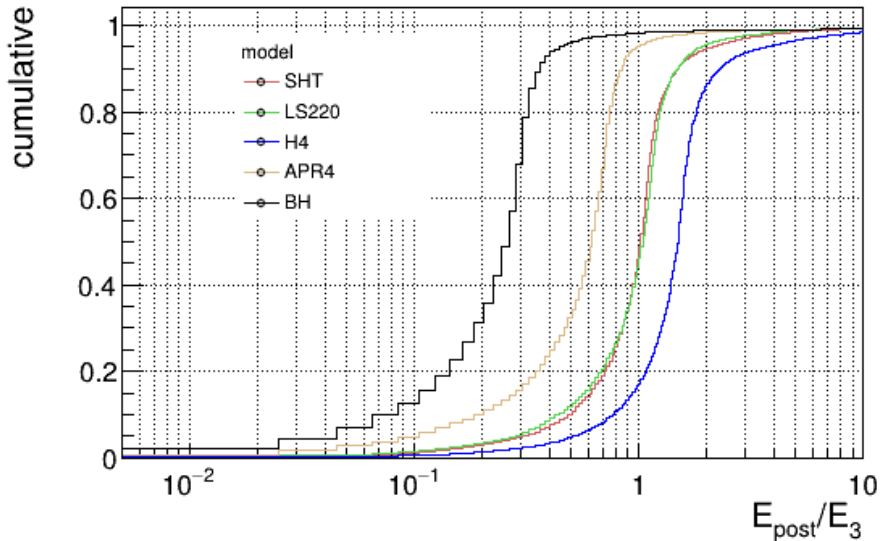


Figure 6.1: Cumulative distribution of E_{pm}/E_3 for the various models considered. The label BH indicates the SHT-M2.2-I model which is representative of a prompt collapse to a black hole.

As we highlighted in Chapter 4, the estimated features of the reconstructed signal strongly depends on its SNR. For this reason we performed the analysis described above considering events in different SNR bins, the same used in previous chapter (Fig.6.3).

The false dismissal probability (FDP) of a post-merger emission for a given false alarm probability (FAP), represented by a prompt-collapse to a black hole, are reported in Table 6.1, for the usual false alarm probability values $\sim 10\%$, $\sim 5\%$ and $\sim 1\%$. Results for the different SNR bins considered are also reported.

We accept only criteria for which less than $1/3$ of events with NS remnant formation are missed; the FDP probabilities that satisfy this threshold are highlighted in green in Table 6.1. In the general case, at least a 5% FAP must be allowed in order not to miss more than $\sim 30\%$ events. However, there are large differences between the various SNR bins. While for events with $10 \leq SNR \leq 20$ also a 10% FAP implies that approximately half of the events with NS remnant are missed, when $SNR \geq 55$ even a 1% FAP allows a FDP $< 1/3$. However, we remind that, as explained in Section 4.3, the SNR we consider is the one calculated by cWB, which in general is lower than the one

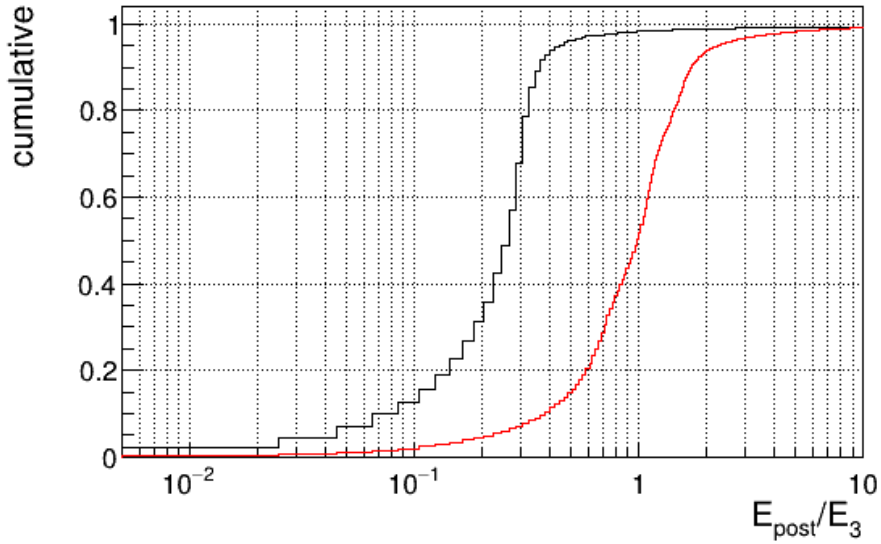


Figure 6.2: Cumulative distribution of E_{pm}/E_3 for the SHT-M2.2-I model, expected to collapse promptly to a black hole (black) and total cumulative distribution of E_{pm}/E_3 for the models expected to leave a HMNS or SMNS remnant, assuming a flat prior.

computed by optimal matched filtering methods , as e.g. PyCBC, and usually indicated as the event SNR. This is due to the fact that, while PyCBC considers also the entire inspiral phase, we limited the cWB reconstruction stage in the frequency band [512 – 4096]Hz, thus loosing a part of the signal.

FAP	FDP					Total
	SNR 10-20	SNR 25-35	SNR 55-65	SNR 115-125		
10%	0.514	0.309	0.063	0.031	0.097	
5%	0.774	0.368	0.085	0.033	0.129	
1%	0.896	0.838	0.289	0.049	0.970	

Table 6.1: FAP for the detection of a post-merger emission and corresponding FDP as a function of some SNR bins and for all simulated events. These results are based on the E_{pm}/E_3 distributions in Fig.6.2 and 6.3

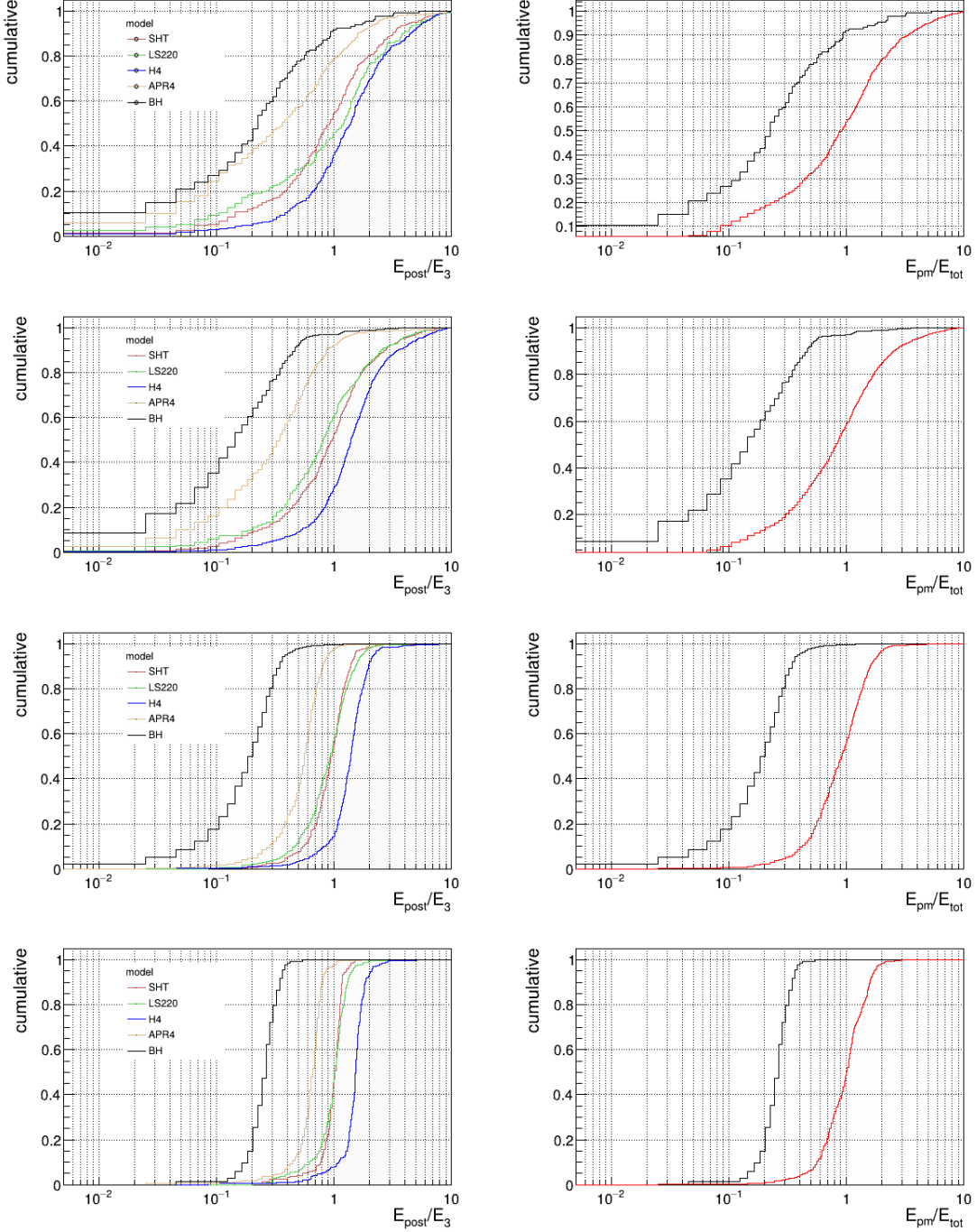


Figure 6.3: *Left:* Cumulative distribution of E_{pm}/E_3 for the various models considered. The label BH indicates the SHT-M2.2-I model which is expected to promptly collapse to a black hole. *Right:* Cumulative distribution of E_{pm}/E_3 for the SHT-M2.2-I model, expected to collapse promptly to a black hole (black) and total cumulative distribution of E_{pm}/E_3 for the models expected to leave a HMNS or SMNS remnant, with flat prior assumed. The plots are shown for events in different SNR bins. *Top row:* SNR between 10 and 20; *second row:* SNR between 25 and 35; *third row:* SNR between 55 and 65; *bottom row:* SNR between 115 and 125. As expected, for the lower SNR bins the distributions are not separate enough to ensure a low FAP and a low FDP, see Table 6.1

6.2 Luminosity profile

We want to investigate the difference in luminosity profiles for the various models, in particular for what concerns luminosity \mathcal{F}_3 in frequency band $1280 < f < 1792\text{Hz}$ and \mathcal{F}_{pm} for $f > 1792\text{Hz}$ (see Section 5.3). This is done by considering two features: the difference between median times and the profiles overlapping.

To be sure to take into account all the post-merger signal, including its initial part at lower energies, for this study we consider a different time cut with respect to the one used in previous chapter (see Section 5.2), setting $t'_{cut} = \bar{t}_1 + 2dt$, with \bar{t}_1 the energy-weighted time of frequency layer $256 - 768\text{Hz}$.

For what concerns the median time, we computed the time at which the cumulative energy in the two different frequency regions reaches 50%, $t_{med,3}$ and $t_{med,pm}$ respectively, and then calculated the difference $t_{med,pm} - t_{med,3}$, whose distribution is plotted in Fig.6.4 for the different models considered. Fig.6.4 shows clearly that, although some difference between the various models is present, with our actual tools and resolution it is not enough to reach a sufficient degree of discrimination among different emission models.

We define the luminosity profile overlapping function as

$$\mathcal{O} = \frac{\sum_i \mathcal{F}_3[i] \cdot \mathcal{F}_{pm}[i]}{\left(\sum_i \mathcal{F}_3[i]^2 \sum_i \mathcal{F}_{pm}[i]^2\right)^{1/2}} \quad (6.1)$$

where i is the time index. The resulting distributions for the different models are shown in Fig.6.5 (*left*). In this case, large differences are present between the considered models, in particular for what concerns the value at which distributions are peaked. As expected, the overlapping function for the prompt-collapse to black hole case is peaked near $\mathcal{O} \sim 1$, since in this case we do not expect a later peak, corresponding to post-merger, to be present. Therefore, this overlapping function could be a useful parameter to infer properties of the post-merger signal source.

As we said for the other estimated parameters, the reconstructed event SNR strongly influences the distribution. In Fig.6.5 (*right*) is shown the overlapping function PDF for events with $55 \leq SNR \leq 65$, value interval chosen because at lower SNR the PDFs become wider and less informative, while for higher SNR they are narrower but such signals are expected to be rarer.

In order to see how this SNR selection affects the PDFs, Table 6.2 reports the value of RMS and mean of the distributions for every model both for all events and for events with $55 \leq SNR \leq 65$. As expected, choosing this SNR bin distributions become narrower, with a lower RMS value, because we are excluding the tails caused by low-SNR events. On the other hand, the mean remains almost unaffected in all but one case.

6.3 Simulating an observation

In this section we investigate how to infer information about the post-merger GW source given an observed signal. We performed an additional simulation to build a set of ~ 100 events with a specific waveform model, namely SHT, within our test SNR bin (55-65). More precisely, we have

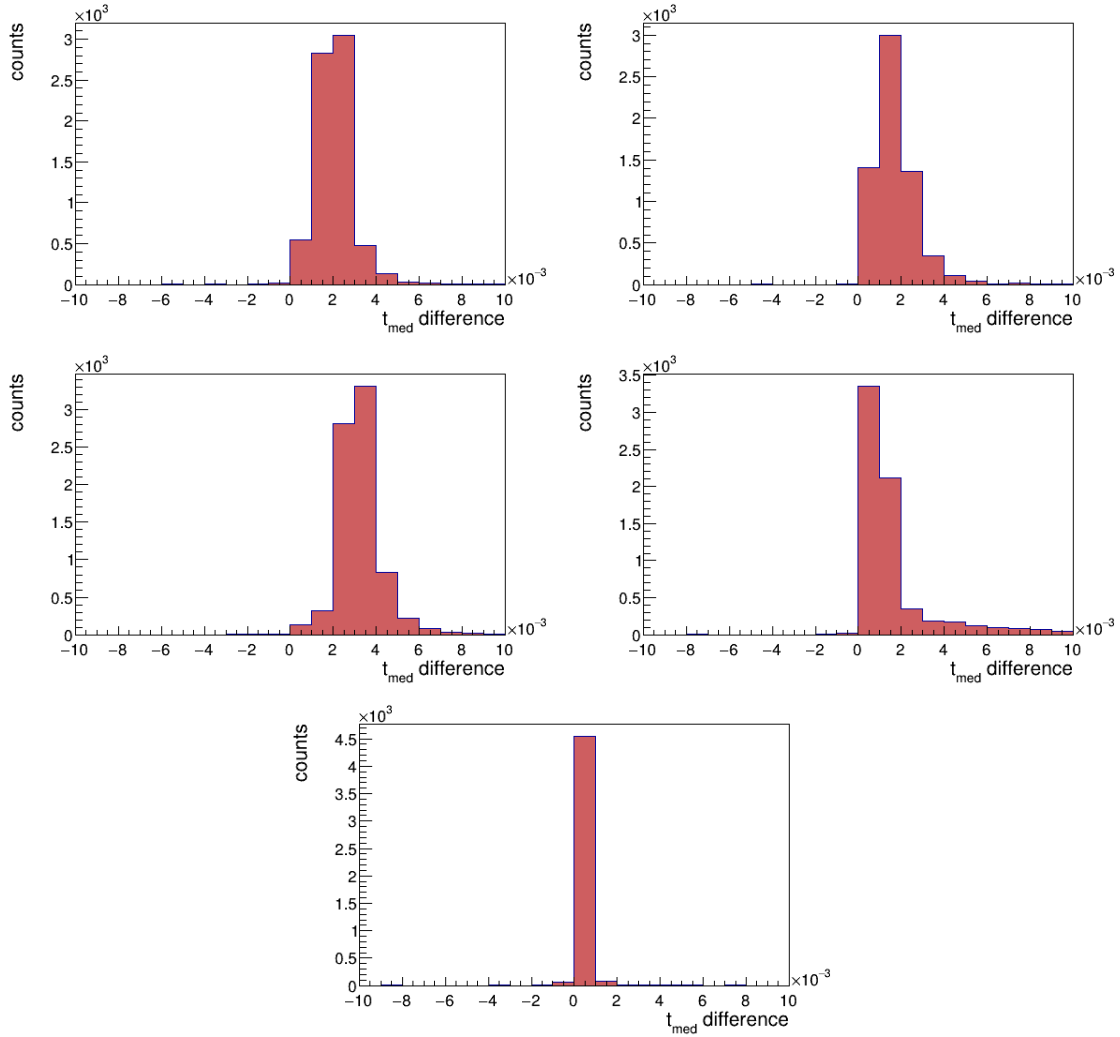


Figure 6.4: Distribution of $t_{med,pm} - t_{med,3}$ for SHT-M2.0-S model (*top left*), LS220 model (*top right*), H4 model (*middle left*), APR4 model (*middle right*) and SHT-M2.2-I model (*bottom*). The central bin values appear on the left bin ends.

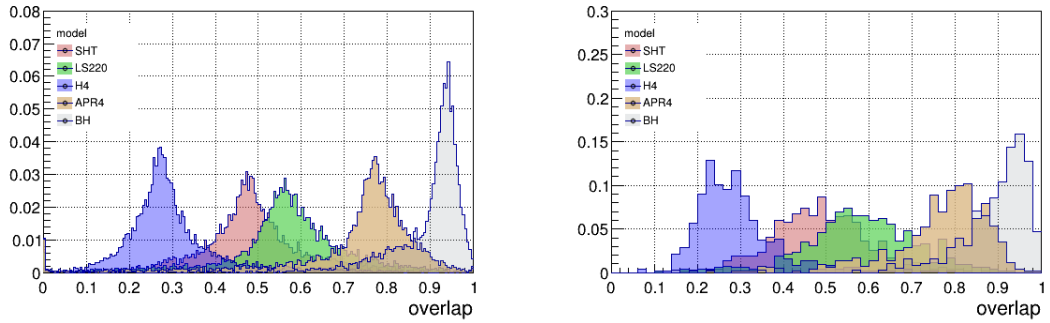


Figure 6.5: PDF of the luminosity profiles overlapping function for the models considered for all the events (left) and for events with $55 \leq SNR \leq 65$ (right). The distributions binning is different, because the resolution used for the total plot cannot be applied to the other one due to a lack of statistics that would cause too large fluctuations.

	RMS		Mean	
	SNR 55-65	Total	SNR 55-65	Total
SHT	0.11	0.14	0.49	0.489
LS220	0.13	0.15	0.58	0.565
H4	0.10	0.13	0.29	0.304
APR4	0.12	0.17	0.76	0.720
BH	0.11	0.14	0.88	0.880

Table 6.2: Comparison of mean and RMS values of the \mathcal{O} distributions for all events and for the 55-65 SNR bin. For all waveform models, the RMS is significantly larger when including all events, due to the contribution of lower SNR. Only in the APR4 case there is a significant shift in the mean values, although smaller than RMS.

98 "observed events" in the 55-65 SNR bin under the same selection criteria described in previous chapter (see Table 5.1).

We compute the likelihood ratio between the different models. For simplicity, this comparison is performed only on model pairs and therefore the likelihood ratio is defined as

$$L_{ratio} = \frac{PDF(M_i)}{PDF(M_{ref})}, \quad (6.2)$$

where the PDF are the ones coming from the reference simulations described in previous sections.

This analysis is repeated considering, time by time, a different model as the reference one.

The first estimator we study is the overlapping function \mathcal{O} , whose PDF for the different models is shown in Fig.6.5. Fig.6.6(*Top and second row*) show the likelihood ratio behavior between models predicting the formation of a NS remnant, while Fig.6.6(*bottom*) shows L_{ratio} taking as reference the model promptly collapsing to a black hole.

Looking at Fig.6.6 we can distinguish some regions of overlapping function values in which the different reference models are more probable with respect to the others. We choose a threshold

$$threshold : \quad |Log(L_{ratio})| = 0.5 \quad (6.3)$$

such that

- if $L_{ratio} > 0.5$ we state that the observation favors sufficiently model M_i
- if $-0.5 \leq L_{ratio} \leq 0.5$ the result is not sufficiently informative
- if $L_{ratio} < -0.5$ we state that the result favors sufficiently model M_{ref}

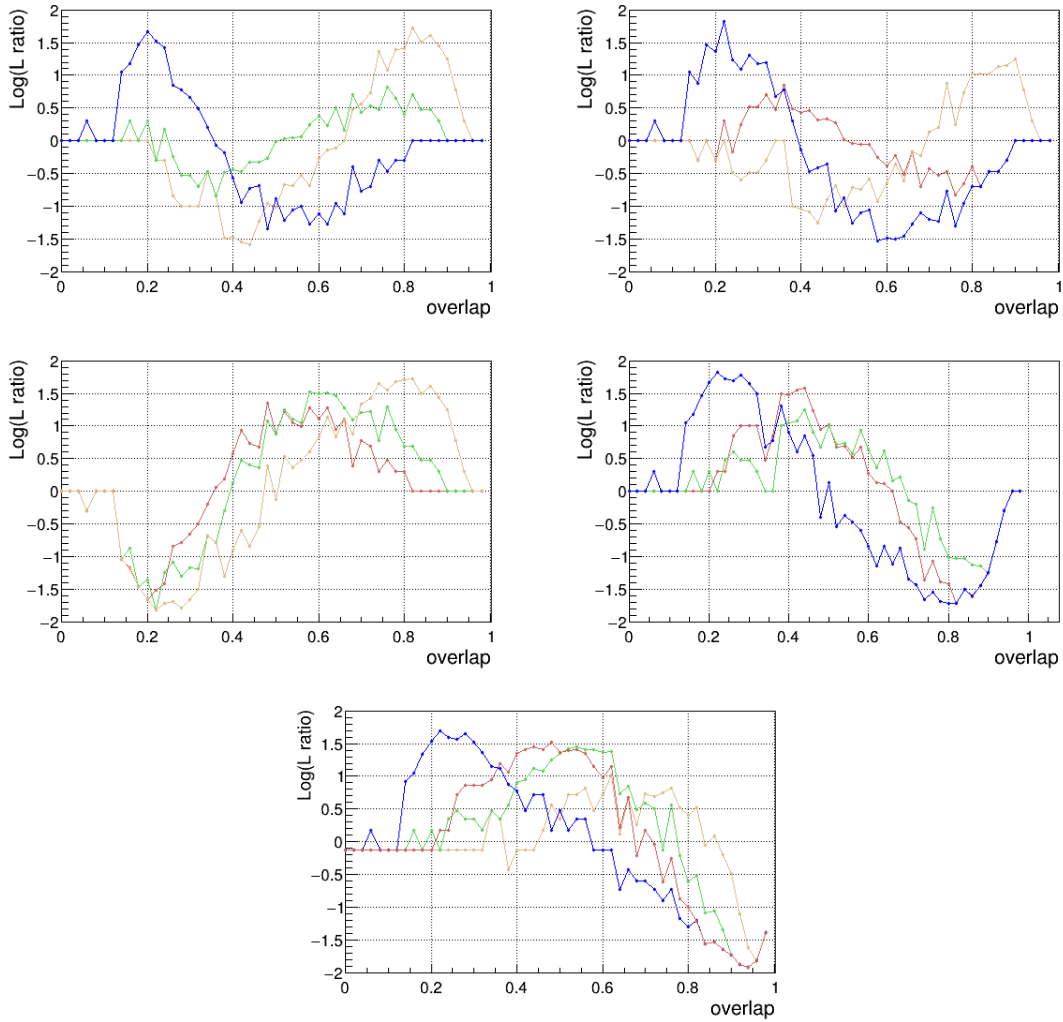


Figure 6.6: $\text{Log}(L_{ratio})$ as a function of the overlapping luminosity parameter, taking as reference model SHT (top left), LS220 (top right), H4 (middle left), APR4 (middle right) and SHT-M2.2-I (predicting prompt collapse to a BH) (bottom). The M_i taken among the models with formation of a neutron star remnant follow the color code: red = SHT, green = LS220, blue = H4, orange = APR4.

This choice is just indicative and appears reasonable when priors are similar as in our case.

Following the criterion described above, for each other model M_i we divided the \mathcal{O} values interval in different regions in which either M_i is excluded or M_i is favored or we do not have enough information to make a decision. Since the new population, that represents the observed event, has been simulated with the SHT waveform, we choose SHT as M_{ref} and thus $M_i = \{\text{LS220}, \text{H4}, \text{APR4}, \text{BH}\}$ (we remind that the model indicated as "BH" is the SHT-M2.0-S, expected to promptly collapse to a black hole). If \mathcal{O} of the "observed event" falls in the region with M_i excluded we say that we classified the event correctly, if it is in the region where M_i is favored the classification is wrong, otherwise uncertain. Fig.6.7 displays how many events have been classified in these three ways for every waveform M_i . Table 6.3 reports the percentage of events with correct, uncertain or wrong classification. In the comparison with LS220 model most of the classification were uncertain, consistent with the fact that a large region of their PDF is

overlapped. For all the other models instead the classification based on this estimator was efficient, with more than 75% of events classified correctly, up to a 91% correct assignments in the case of the prompt-collapse to black hole model. Interestingly, the events classified wrongly are only a few percent in any case.

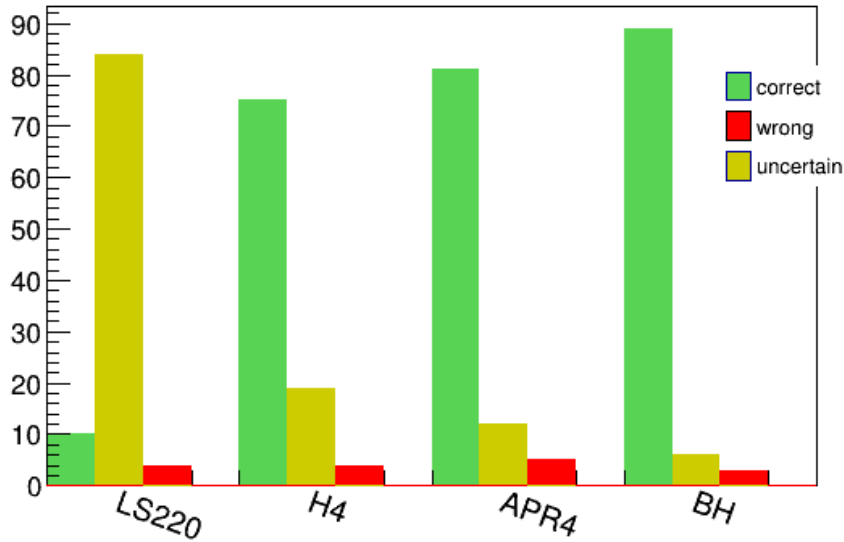


Figure 6.7: This plot shows, for the \mathcal{O} estimator analysis, how many events, among those in the simulated "observation", correctly exclude (green) a given model, how many wrongly select that model (red), and for how many of them information is not enough and therefore the model exclusion remains uncertain (yellow).

	LS220	H4	APR4	BH
correct	10%	77%	83%	91%
uncertain	86%	19%	12%	6%
wrong	4%	4%	5%	1%

Table 6.3: Table reporting the percentage of events which lead to a correct, wrong or uncertain exclusion of the model indicated in the top row. Values are based on the $\log(L_{ratio})$ reported in Fig.6.6.

We tried to perform a similar analysis with the spectral estimators found. For what concerns energy-weighted frequency, the PDF for the different models (Fig.6.8) shows clearly that a distinction between models as the one performed with \mathcal{O} is not feasible. Only the model expected to promptly collapse to a black hole has a separated peak, the models with a NS remnant have too large and overlapped distributions. The analysis based on likelihood ratio described above, therefore, can not be performed between every model. Anyway, it could be used to discriminate between a prompt-collapse to black hole and the formation of a NS remnant.

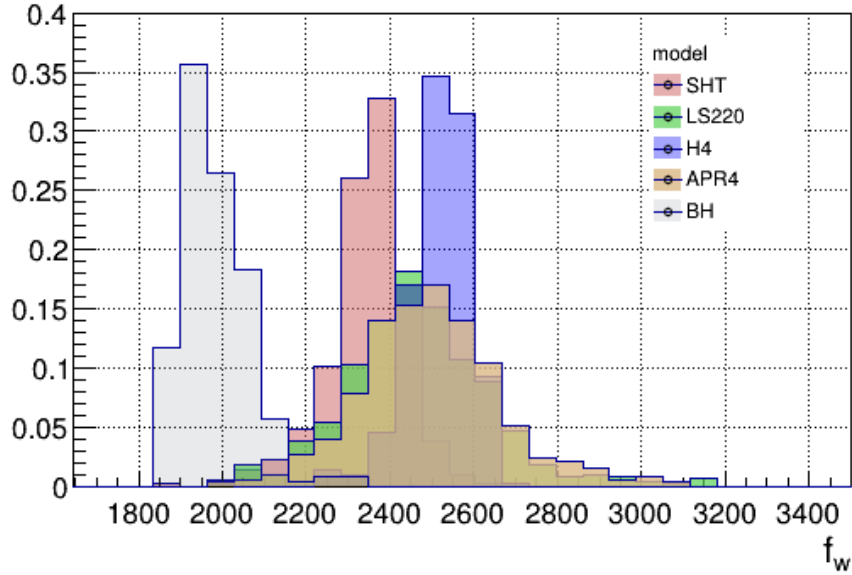


Figure 6.8: PDFs of the energy-weighted frequency parameter for events in the 55-65 SNR bin for all the models considered. Weighted frequency is expressed in Hz and its PDF in $1/\text{Hz}$. PDFs of models predicting a NS are too much overlapped, in particular the ones for APR4 (orange) and LS220 (green).

Choosing the frequency bandwidth estimator, instead the different models PDFs for events with $55 \leq \text{SNR} \leq 65$ are shown in Fig.6.9.

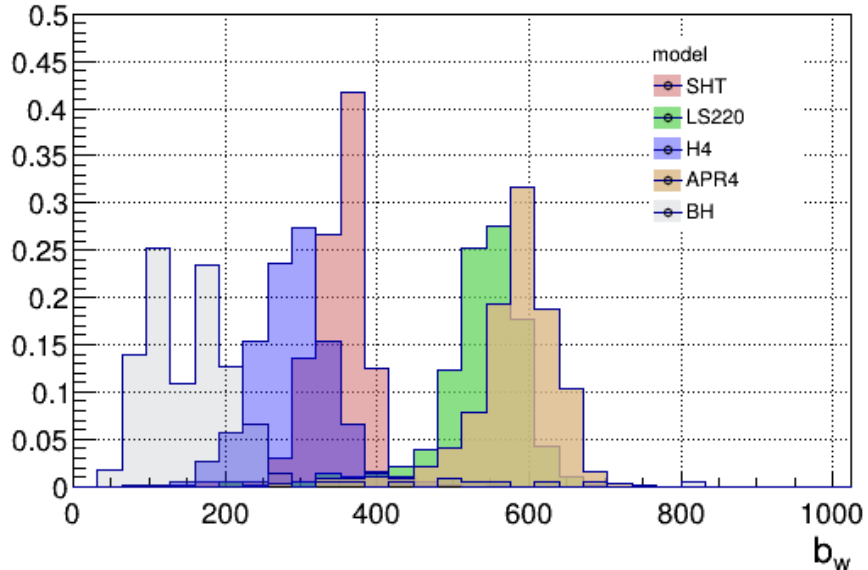


Figure 6.9: PDFs of the energy-weighted frequency bandwidth parameter for events in the 55-65 SNR bin for all the models considered. Weighted bandwidth is expressed in Hz and its PDF in $1/\text{Hz}$.

The PDFs of different models are quite well separated, hence we performed the same analysis described for the overlapping function. The likelihood ratios for the different models are shown

in Fig.6.10. The classification results for the same simulated observed events used for the \mathcal{O} , keeping the uncertainty region for likelihood values between $[-0.5, 0.5]$, are shown in Fig.6.11 and percentage are reported in Table 6.4.

The most uncertain classification happens for H4 model, but the other one are almost always correctly excluded. In particular, for the LS220 and APR4 models no wrong assignments have been done. This is particularly interesting because the most uncertain model for what concerns the overlapping estimators, namely LS200, is instead clearly distinguished with the weighted bandwidth. Similarly, the H4 model with shows a quite large uncertain with the bandwidth is correctly excluded by the overlapping function.

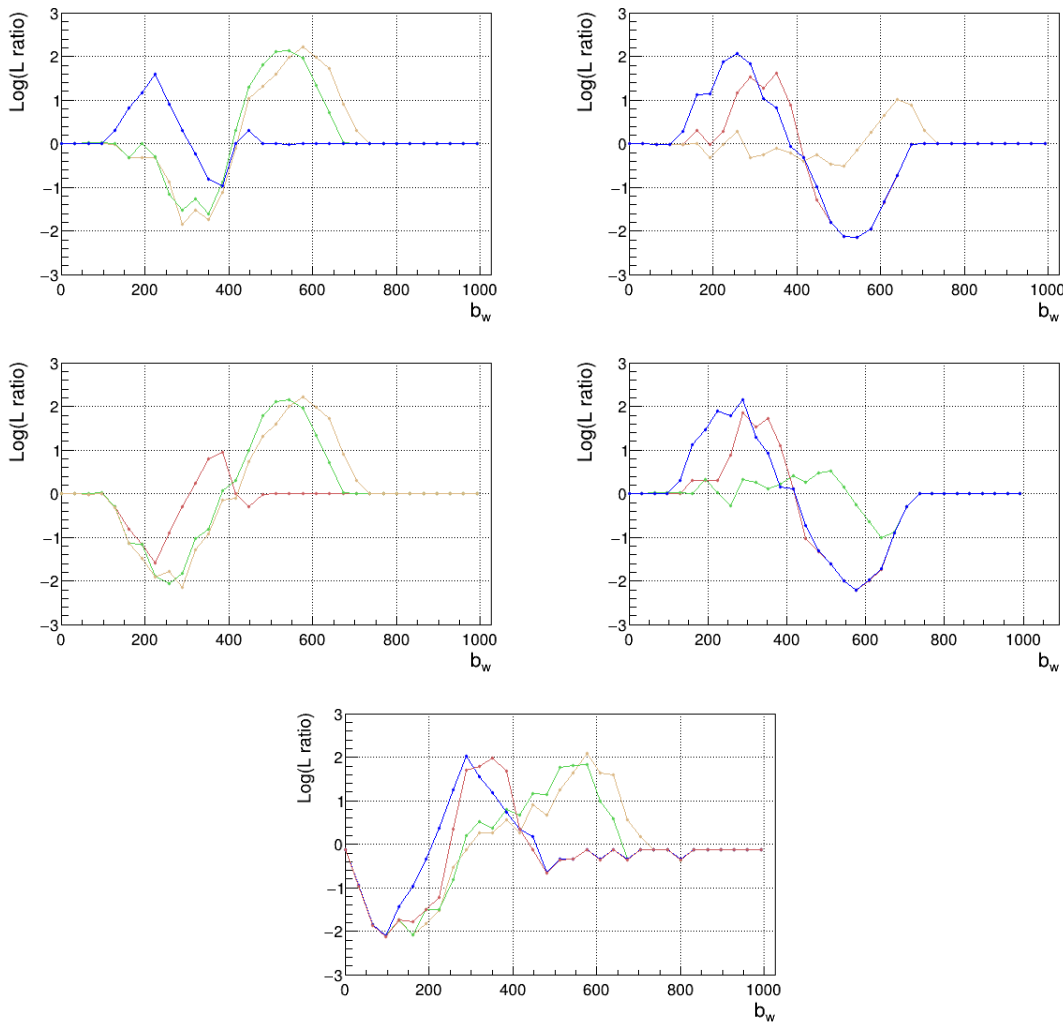


Figure 6.10: $\text{Log}(L_{ratio})$ as a function of the energy-weighted frequency bandwidth parameter, taking as reference model SHT (top left), LS220 (top right), H4 (middle left), APR4 (middle right) and SHT-M2.2-I (predicting prompt collapse to a BH) (bottom). The M_i taken among the models with formation of a neutron star remnant follow the color code: red = SHT, green = LS220, blue = H4, orange = APR4.

In this exploratory analysis we demonstrated that the luminosity profile can be used to infer properties about the PM signal source, a result which is not present elsewhere in literature. Moreover, we demonstrated that the joint use of spectral parameters and luminosity profile can greatly

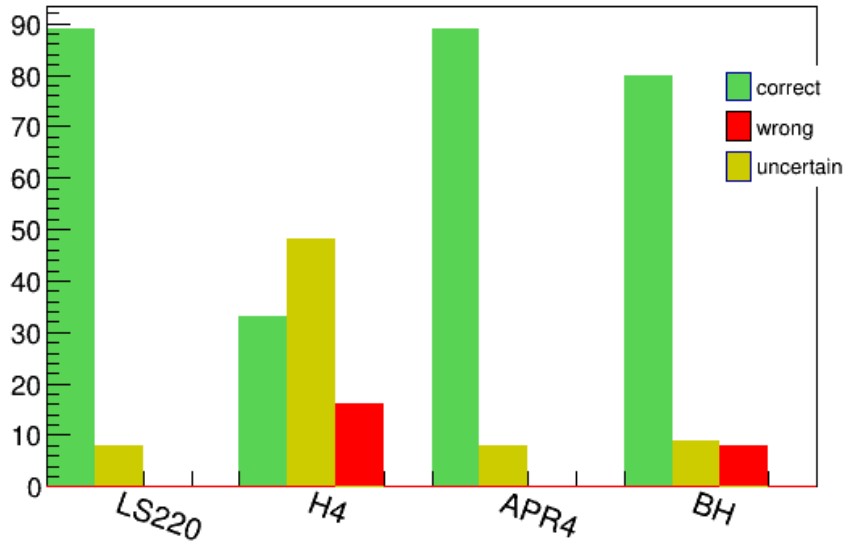


Figure 6.11: This plot shows, for the weighted bandwidth estimator analysis, how many events, among those in the simulated "observation", correctly exclude (green) a given model, how many wrongly select that model (red), and for how many of them information is not enough and therefore the model exclusion remains uncertain (yellow).

	LS220	H4	APR4	BH
correct	92%	34%	92%	82%
uncertain	8%	49%	8%	9%
wrong	0%	16%	0%	8%

Table 6.4: Table reporting the percentage of events which lead to a correct, wrong or uncertain exclusion of the model indicated in the top row. Values are based on the $\log(L_{ratio})$ reported in Fig.6.10.

enhance the capability to identify the EOS model. As a next step, we need to make a synthesis of the inference results based on different observables. This requires to study the full variance matrix, including cross correlation terms among different results.

Conclusions

The detection of the first gravitational wave signal from a BNS in August, 2017 opened a completely new window on the study of the physics of these objects, in particular for what concerns NS equation of state. After the coalescence, a BNS could have different fates depending on the mass and EOS of the progenitors, those influence also the gravitational wave signal emitted during this post-merger phase. Finding and interpreting EOS prints in this signal would help discriminating between the various NS models proposed. Although the post-merger signal is more difficult to detect with respect to the late-inspiral and merger one, because of a lower sensitivity of the detectors in the frequency region involved, the improvements carried out for the next observing runs should allow the detectors to gain sensitivity also around the typical frequencies of post-merger gravitational-wave signals.

In this thesis we presented a data analysis method, based on cWB algorithm, to characterize the gravitational wave signal emitted by neutron stars binaries during the post-merger. In particular, the developed tools aim at characterizing the reconstructed signal in time and frequency without assumptions on the signal's morphology.

We applied the procedure developed in [50] in order to identify, on the reconstructed signal TF map, the region with the post-merger, applying a cut in time and frequency. For our analysis, these maps are computed, from the reconstructed signal, at fixed resolution $df = 512\text{Hz}$ and $dt \simeq 1\text{ms}$, needed to ensure the required precision in time. The frequency cut is taken a priori at $f = 1792\text{Hz}$, since almost all models predict higher frequencies for the post-merger signal. t_{cut} instead is taken immediately after the merger time, computed as the energy-weighted time in frequency band 768-1280 Hz.

For what concerns time characterization, we found two main estimators, the luminosity profile of the reconstructed event, that can be analyzed in different frequency bands, and the time duration of reconstructed post-merger signal. Another feature we studied is the energy distribution in the TF map region in which the PMNS signal is expected, in particular the ratio between the total energy of PMN and the energy in frequency band 1280-1792. Instead, for what concerns spectral characterization, we used the energy-weighted frequency and bandwidth. Since, in this case, we are not interested in a good precision in time, we studied the spectral features starting from a reconstructed TF map with fixed resolution $df = 64\text{Hz}$ and $dt \simeq 7.8\text{ms}$. In general, we found out that these estimators have different behaviors, and therefore distributions, depending on the neutron star model considered. In particular, large differences are present between the model predicting a prompt-collapse to a black hole and ones in which the remnant is expected to survive as a HMNS or SMNS for some time, of the order of ms or seconds respectively, before collapsing

to a black hole. However, the distributions are strongly influenced by the reconstructed SNR value of the events considered, therefore a proper comparison must be made between events with similar SNR. Our analysis confirmed that, in order to gather information from the post-merger, events with high SNR, approximately $SNR \gtrsim 50$, are needed. This is also the reason why we simulated signals with the detector sensitivity designed for O4.

In the last chapter we outlined a method for identifying the presence of a post-merger emission from a NS remnant and enabling some EOS classification, exploiting some of the estimators previously found. We investigated the possibility of discriminating a prompt-collapse scenario from the formation of a HMNS or SMNS starting from the energy distribution the TF region where the PM signal is expected. We concluded that in general at least a 5% false alarm probability must be allowed in order not to risk missing more than 30% events, but, again, the results strongly depend on the events SNR. The study of the luminosity profiles, instead, was performed in two different ways: we computed the difference in median time of the cumulative energy distributions in the two frequency regions $1280Hz < f < 1792Hz$ and $f > 1792Hz$ and the normalized cross correlation coefficient between the two. While, with the actual tools, the median time difference is not very informative, the r coefficient distributions show large differences between the models considered, therefore can be used both to discriminate a prompt-collapse scenario and to classify the different EOS leading to a NS remnant formation. This is a pilot study that must be extended in order to obtain a systematic approach, in particular our conclusions are necessarily limited to the models we considered. An interesting development would be performing the analysis taking into account also different mass values for the same EOS. However, when observations will be available, template algorithms will allow to estimate some parameters of the progenitors, like masses, with good precision, as demonstrated for GW170817 [32]. Therefore, it would be enough to implement our analysis method on signals simulated with Numerical Relativity waveforms of models with masses as near as possible to the measured ones.

To conclude, we presented a new data analysis method to characterize the post-merger GW signal through some estimators that can be used both to discriminate between a prompt-collapse scenario from the formation of a NS remnant and to help identifying the EOS model. We demonstrated that the luminosity profile can be used to infer properties about the PM signal source, a result which is not present elsewhere in literature. Moreover, we demonstrated that the joint use of spectral parameters and luminosity profile can greatly enhance the capability to identify the EOS model. All the results we presented concern data from the Livingston detector, a future development will try to improve these result by using the information of the entire network of detectors.

Bibliography

- [1] M. Maggiore, *Gravitational waves- Theory and Experiments*, Oxford University Press (2008)
- [2] B. F. Schutz, *A first course in general relativity*, Cambridge University Press (1988)
- [3] J. B. Hartle, *Gravity - An Introduction to Einstein's General Relativity*, Pearson, second edition (2014)
- [4] B. S. Sathyaprakash, B. F. Schutz, Physics, Astrophysics and Cosmology with Gravitational Waves, *Living Rev. Relativity*, **12** (2009) 2
- [5] M. Rinaldi, General Relativity and Cosmology, notes of General Relativity and Cosmology course, University of Trento (2017)
- [6] S. Kawamura, Ground-based interferometers and their science reach, *Class. Quantum Grav.* **27** (2010) 084001
- [7] <https://www.ligo.caltech.edu/page/ligos-ifo>
- [8] M. Pitkin *et al.*, Gravitational Wave Detection by Interferometry (ground and space), *Living Rev. Rel.* **14** (2011) 5
- [9] W. T. Ni, M. Zimmermann, Inertial and gravitational effects in the proper reference frame of an accelerated, rotating observer, *Phys. Rev. D* **17** (1978) 1473
- [10] D. Rätzel, I. Fuentes, Testing small scale gravitational wave detectors with dynamical mass distributions, *Journal of Physics Communications* (2018)
- [11] <http://www.auriga.lng.infn.it/auriga/detector/overview.html>
- [12] S. S. Y. Chua, *Quantum Enhancement of a 4km Laser Interferometer Gravitational Waves Detector*, Ch.2 "Gravitational Waves and the Quest for Their Direct Detection" Springer International Publishing (2015)
- [13] R. Del Fabbro *et al.*, Three-dimensional seismic super-attenuator for low frequency gravitational wave detection, *Physics Letters A*.**124** (1987) pp.253-257
- [14] S. Braccini *et al.*, Measurement of the seismic attenuation performance of the VIRGO Super-attenuator, *Astrop. Phys.***23** (2005) pp 557-565

- [15] B. P. Abbott *et al.* [LIGO Scientific and Virgo Collaborations], Observation of Gravitational Waves from a Binary Black Hole Merger, *Phys. Rev. Lett.* **116** (2016) 061102
- [16] B. P. Abbott *et al.* [LIGO Scientific and Virgo Collaborations], GW151226: Observation of Gravitational Waves from a 22-Solar-Mass Binary Black Hole Coalescence, *Phys. Rev. Lett.* **116** (2016) 241103
- [17] B. P. Abbott *et al.* [LIGO Scientific Collaboration], Advanced LIGO, *Class. Quant. Grav.* **32** (2014) no 7,
- [18] <http://www.physics.gla.ac.uk/igr>
- [19] D. A. Ostlie, B. W. Carroll, *An introduction to Modern Stellar Astrophysics*, Benjamin-Cummings Pub. Co., First edition (1996)
- [20] M. S. Longair, *High Energy Astrophysics*, Cambridge University Press, Third edition (2011)
- [21] P. Haensel, A. Y. Potekhin, D. G. Yakovlev, *Neutron Stars 1, Equation of State and Structure*, Springer Berlin (2010)
- [22] J. M. Lattimer, The Nuclear Equation of State and Neutron Star Masses, *Annu. Rev. Nucl. Part. Phys.* **62** (2012)
- [23] D. R. Lorimer, Binary and Millisecond Pulsars, *Living Rev. Rel.* **11** (2008) 8
- [24] X.Roca-Maza *et al.*, Influence of the nuclear symmetry energy on the structure and composition of the outer crust, arXiv:1109.3011 (2011)
- [25] Hotokezaka K. et al, Remnant massive neutron stars of binary neutron star mergers: Evolution process and gravitational waveform, *Phys. Rev. D* **88** (2013) 044026
- [26] J. A. Faber,F. A. Rasio, Binary Neutron Star Mergers, *Living Rev. Rel.* **15** (2012) 8
- [27] A. Bauswein *et al.*, Neutron Stars Properties from the Postmerger Gravitational Wave Signal of Binary Neutron Stars, *HT. Phys. Part. Nuclei* **46** (2015) 835
- [28] L. Baiotti, L. Rezzolla, Binary neutron-star mergers: a review of Einstein's richest laboratory, *Rept. Prog. Phys.* **80** (2017) no.9, 096901
- [29] G. B. Cook *et al.*, Rapidly rotating neutron stars in general relativity: Realistic equations of state *Astrophys.J.* **424** (1994) 832
- [30] L. Rezzolla, K. Takami, Gravitational-wave signal from binary neutron stars: a systematic analysis of the spectral properties, *Phys. Rev. D* **93** (2016), 124051
- [31] B. P. Abbott *et al.* [LIGO Scientific and Virgo Collaborations], GW170817: Observation of Gravitational Waves from a Binary Neutron Star Inspiral, *Phys. Rev. Lett.* **119** (2017), 161101

- [32] B. P. Abbott *et al.* [LIGO Scientific and Virgo Collaborations], Properties of the Binary Neutron Star Merger GW170817, *Phys. Rev. X* **9** (2019), 011001
- [33] B. P. Abbott *et al.* [LIGO Scientific and Virgo Collaborations], GW170817: Measurements of Neutron Star Radii and Equation of State, *Phys. Rev. Lett.* **121** (2018), 161101
- [34] LIGO Scientific and Virgo and Fermi GBM and INTEGRAL and IceCube and IPN and Insight-Hxmt and ANTARES and Swift and Dark Energy Camera GW-EM and DES and DLT40 and GRAWITA and Fermi-LAT and ATCA and ASKAP and OzGrav and DWF (Deeper Wider Faster Program) and AST3 and CAASTRO and VINROUGE and MASTER and J-GEM and GROWTH and JAGWAR and CaltechNRAO and TTU-NRAO and NuSTAR and Pan-STARRS and KU and Nordic Optical Telescope and ePESSTO and GROND and Texas Tech University and TOROS and BOOTES and MWA and CALET and IKI-GW Follow-up and H.E.S.S. and LOFAR and LWA and HAWC and Pierre Auger and ALMA and Pi of Sky and DFN and ATLAS Telescopes and High Time Resolution Universe Survey and RIMAS and RATIR and SKA South Africa/MeerKAT Collaborations and AstroSat Cadmium Zinc Telluride Imager Team and AGILE Team and 1M2H Team and Las Cumbres Observatory Group and MAXI Team and TZAC Consortium and SALT Group and Euro VLBI Team and Chandra Team at McGill University, Multi-messenger Observations of a Binary Neutron Star Merger, *Astrophys. J. Lett.* **848** (2017), L12
- [35] LIGO Scientific Collaboration and Virgo Collaboration, Fermi Gamma-ray Burst Monitor, and INTEGRAL, Gravitational Waves and Gamma-Rays from a Binary Neutron Star Merger: GW170817 and GRB 170817A, *Astrophys. J. Lett.* **848** (2017), L13
- [36] B. P. Abbott *et al.* [LIGO Scientific and Virgo Collaborations], Search for Post-merger Gravitational Waves from the Remnant of the Binary Neutron Star Merger GW170817, *Astrophys. J. Lett.* **851** (2017) no.1, L16
- [37] H. Y. Chen *et al.*, Distance measures in gravitational-wave astrophysics and cosmology, (2017) arXiv:1709.08079
- [38] X. Zhu, Inferring the population properties of binary neutron stars with gravitational-wave measurements of spin, *Phys. Rev. D* **98** (2018) 043002
- [39] M- Burgay *et al.*, An Increased estimate of the merger rate of double neutron stars from observations of a highly relativistic system, *Nature (London)* **426** (2003) 531
- [40] B. D. Metzger *et al.*, Electromagnetic counterparts of compact object mergers powered by the radioactive decay of r-process nuclei, *Mon.Not.Roy.Astron.Soc.* **406** (2010) 2650
- [41] T. Hinderer, Tidal Love numbers of neutron stars, *Astrophys. J.* **677** (2008) 1216
- [42] J. M. Lattimer, The Nuclear Equation of State and Neutron Star Masses, *Ann.Rev.Nucl.Part.Sci.* **62** (2012) 485-515

- [43] G. Shen, C. J. Horowitz and S. Teige, Equation of State of Dense Matter from a density dependent relativistic mean field model, *Phys. Rev. C* **82** (2010) 015806
- [44] J. M. Lattimer, F. D. Swesty, A Generalized equation of state for hot, dense matter, *Nucl. Phys. A* **535** (1991) 331
- [45] A. Akmal, V. R. Pandharipande, and D. G. Ravenhall, Equation of state of nucleon matter and neutron star structure, *Phys. Rev. C* **58** (1998) 1804
- [46] N. K. Glendenning and S. A. Moszkowsk, Reconciliation of neutron-star masses and binding of the Λ in hypernuclei, *Phys. Rev. Lett.* **67** (1991) 2414
- [47] W. Kastaun, F. Galeazzi, Properties of hypermassive neutron stars formed in mergers of spinning binaries, *Phys. Rev. D* **91** (2015) no.6, 064027
- [48] A. Endrizzi *et al.*, General Relativistic Magnetohydrodynamic Simulations of Binary Neutron Star Mergers with the APR4 Equation of State, *Class. Quant. Grav.* **33** (2016) no.16, 164001
- [49] T. Kawamura T. *et al.*, Binary Neutron Star Mergers and Short Gamma-Ray Bursts: Effects of Magnetic Field Orientation, Equation of State, and Mass Ratio, *Phys. Rev. D* **94** (2016) no.6, 064012
- [50] M. C. Tringali, *Analysis methods for gravitational wave from binary neutron star coalescences: investigation on the post-merger phase* (2017)
- [51] cWB Home Page:
<https://ldas-jobs.ligo.caltech.edu/waveburst/doc/cwb/xman/index.html>
- [52] B. P. Abbott *et al.* (KAGRA Collaboration, Scientific Collaboration and Virgo Collaboration), LIGO, Prospects for Observing and Localizing Gravitational-Wave transients with Advanced LIGO, Advanced Virgo and KAGRA, *Living Rev. Relativ.*, in preparation
- [53] V. Necula *et al.*, Transient analysis with fast Wilson-Daubechies time-frequency transform, *J. Phys. Conf. Ser.* **363** (2012) 012032
- [54] S. Klimenko *et al.*, Coherent method for detection of gravitational wave bursts, *Class. Quant. Grav.* **25** (2008) 114029
- [55] S. Klimenko *et al.*, Method for detection and reconstruction of gravitational wave transients with networks of advanced detectors, *Phys. Rev. D* **93** (2016) no.4, 042004
- [56] S. Klimenko *et al.*, Constrained likelihood analysis for a network of gravitational wave detectors, *Phys. Rev. D* **72** (2005) 122002
- [57] S. Klimenko *et al.*, *Coherent WaveBurst*, LIGO note T060282-00-Z (2007)
- [58] F. Zappa *et al.*, Gravitational-Wave Luminosity of Binary Neutron Stars Mergers, *Phys. Rev. Lett.* **120** (2018) 111101

- [59] M. Drago, *Search for Transient Gravitational Wave Signals with Unknown Waveform in the LIGO-Virgo Network of Interferometric Detectors using a Fully Coherent Algorithm* (2010)
- [60] B. Reinisch, G. Teichtmeister, *Series Expansion with Wavelets*, Advanced Signal Processing 2, Technische Universität Graz (2007)
- [61] S. Klimenko, *Coherent Network Analysis-cWB review*, University of Florida (2014)
- [62] B. P. Abbott *et al.* [LIGO Scientific and Virgo Collaborations], All-sky search for long-duration gravitational wave transients in the first Advanced LIGO observing run, *Class. Quant. Grav.* **35** (2018) no.6, 065009
- [63] ROOT Manual: <https://root.cern.ch/guides/users-guide>
- [64] B. P. Abbott *et al.* [LIGO Scientific and Virgo Collaborations], GWTC-1: A Gravitational-Wave Transient Catalog of Compact Binary Mergers Observed by LIGO and Virgo during the First and Second Observing Runs, arXiv:1811.12907 [astro-ph.HE]
- [65] S. A. Usman *et al.*, The PyCBC search for gravitational waves from compact binary coalescence, *Class. Quant. Grav.* **33** (2016) no.21, 215004